Iris Hehn, BSc

Investigation of the impact of interface dipole layers on the performance of organic solar cells by drift-diffusion simulations

MASTER THESIS

For obtaining the academic degree
Diplom-Ingenieurin

Master Programme of
Technical Physics

Graz University of Technology

Supervisor:
Univ.-Prof. Dipl.-Ing. Dr.techn. Ferdinand Schürrer
Co-Supervisor:
Dipl.-Phys. Dr.rer.nat. Karin Zojer
Institute of Theoretical and Computational Physics

Graz, September 2012

Deutsche Fassung:
Beschluss der Curricula-Kommission für Bachelor-, Master- und Diplomstudien vom 10.11.2008
Genehmigung des Senates am 1.12.2008

EIDESSTATTLICHE ERKLÄRUNG

Ich erkläre an Eides statt, dass ich die vorliegende Arbeit selbstständig verfasst, andere als die angegebenen Quellen/Hilfsmittel nicht benutzt, und die den benutzten Quellen wörtlich und inhaltlich entnommene Stellen als solche kenntlich gemacht habe.

Graz, am ……………………………   ………………………………………………..
(Unterschrift)

Englische Fassung:

STATUTORY DECLARATION

I declare that I have authored this thesis independently, that I have not used other than the declared sources / resources, and that I have explicitly marked all material which has been quoted either literally or by content from the used sources.

……………………………   ………………………………………………..
date   (signature)

Abstract

Modern organic solar cells consist of a number of different active and service layers. At the interfaces shifts in energy levels and charge carrier aggregation can occur. Any interface modification, intended or arbitrary could have a severe impact on the performance of photovoltaic devices. The aim of this work is to investigate the influence of interface dipole layers on the current-voltage characteristics of organic solar cells. We simulate the device by means of a two-dimensional drift-diffusion model. The Poisson equation, the drift-diffusion current equations for electrons and holes as well as the continuity equations for electrons, holes and excitons are discretized on a two-dimensional mesh and then solved self-consistently in an iteration process. The input parameters include the HOMO and LUMO levels of the organic semiconductors, the workfunctions of the contacts and the charge carrier mobilities. The results are discussed considering the electrostatic potential, the local charge carrier distributions and the current-voltage characteristic of the device.

Zusammenfassung

Untersuchung der Auswirkung von Dipolschichten an Grenzflächen auf die Effizienz von organischen Solarzellen mit Drift-Diffusionsmodellen

Moderne organische Solarzellen bestehen aus mehreren aktiven Schichten und diversen Hilfsschichten. An all diesen Grenzflächen kann es zu Verschiebungen der Transportniveaus sowie zu Ladungsträgerakkumulation kommen. Jede Art der Grenzschichtmodifikation kann die Effizienz von Solarzellen gravierend beeinflussen. Das Ziel dieser Arbeit ist daher die Untersuchung von Dipolschichten an Grenzflächen und deren Einfluss auf die Strom-Spannungs-Charakteristik von organischen Solarzellen. Zur Anwendung kommt dabei eine zweidimensionale Drift-Diffusions-Simulation. Die Poissongleichung, die Gleichungen für den Drift-Diffusionsstrom der Elektronen und Löcher sowie die Kontinuitätsgleichungen für Elektronen, Löcher und Excitonen werden dabei auf einem zweidimensionalen Gitter diskretisiert und in einem Iterationsprozess selbstkonsistent gelöst. Die wichtigsten materialspezifischen Eingabeparamter sind die HOMO und LUMO Niveaus der organischen Halbleiter, die Austrittsarbeiten der Kontakte sowie die Ladungsträgermobilitäten. Die Simulationsergebnisse werden anhand des elektrischen Potentials, der örtlich aufgelösten Ladungsträgerdichte sowie der Strom-Spannungs-Charakteristik diskutiert.

Contents

1 Introduction

The energy consumption on Earth increases steadily. The reasons range from the growing world population over the increasing spread of electrical devices to the continuous growth of industrial production. Nearly all activities in modern daily life consume energy. Together with the huge problem of global warming, caused partly by conventional power plants, exploiting alternative energy sources has become a world wide necessity. The scientific development in this area over the last decade has been astonishing, yet the current technological standard is not sufficient for providing electricity based solely on alternative energy sources.

One of the most promising renewable energy sources is of course the sun's radiation. Photovoltaic devices have already reached a standard allowing them to become almost mainstream technology for small scale private energy production. They are almost exclusively based on inorganic materials such as gallium-arsenide or of course the most common of all, silicon. Yet silicon based solar cells have a number of disadvantages. The most distinct being the huge production costs of a single solar cell compared to its power output. This enormous energy consumption is caused primarily by the silicon purification process. Yet this production step is vital for solar cell efficiencies.

An alternative to the common inorganic solar cells are photovoltaic devices based on organic semiconductors. Apart from the reduced material costs organic solar cells could be printed onto the substrate, which is far less expensive and also faster than the conventional assembly process of a silicon solar cell. Different layers of the device can be printed in a roll to roll process onto flexible substrates in far larger dimensions than is now possible. The great disadvantage of organic solar cells, however, is their low efficiency. This problem is being tackled by a number of research groups and the efficiency records have been climbing steadily over the past few years. One crucial point seems to be the combination of different active materials and service layers. The phenomena occurring at these interfaces pose new questions and challenges for the fundamental understanding of the working principal of organic solar cells. Different aspects have been studied by other research groups. The impact of the interface morphology on the characteristics of the solar cell has been addressed. Differences between planar and interdigitated structures as well as nanoparticles dispersed in a matrix have been studied theoretically [29, 43]. The nanoparticle phase has also been tackled by experimental groups [30]. The influence of several material parameters on the shape of the I-V curve has been investigated. Especially the ratio of the charge carrier mobilities has a great impact on the characteristics. It can induce s-shaped I-V curves [41, 44]. The origin of the open circuit voltage has been experimentally tackled by [45]. The first simulations and measurements concerned with dipole layers in organic solar cells have generated a number of new questions [34, 33].

The main aspect of this work is to investigate the impact of dipole layers formed on the interface between two organic active layers on the current-voltage characteristic of solar cells. The simulations are based on solving the Poisson, the drift-diffusion-current and the continuity equations self consistently on a two-dimensional grid. A fixed charge density can be placed at the interface. Analogously the energy levels specified for each material can be shifted to introduce additional potential drops.

In Chapter 2 we give a general overview of different types of solar cells as well as their basic working principal. The operation regimes of a solar cell and the basic transport level alignments are discussed. Charge carrier generation and transport in organic semiconductors are addressed. Lastly the basic semiconductor equations together with the Poisson equation are introduced.

Chapter 3 deals with the derivation of the drift-diffusion equations stated in Chapter 2. The calculation starts from the Boltzmann equation. The bipolar model as well as the low density approximation are introduced. The collision and generation-recombination terms are derived from basic considerations. Rescaling the Boltzmann equation, performing a Hilbert expansion and comparing the coefficients ultimately yields the final drift-diffusion and continuity equations.

In Chapter 4 the numerical methods employed for solving the drift-diffusion equations are described and the used boundary conditions are addressed. Explicitely the discretization procedure and the Scharfetter-Gummel algorithm are explained. The temporal evolution is considered by an implicit time step method.

The simulation results are described in Chapter 5. We start by considering the impact of real contacts including thermionic emission and tunneling from the contact into the active layer. The injection barrier is thereby influenced by the actual electric field at the contact region. The differences to the formerly used ohmic contacts are considerable. Next, the impact of light reflection off the metallic bottom contact back through the device is analyzed. As well, measured absorption spectra are introduced, replacing the formerly used fixed absorption coefficients. The charge separation process at the organic-organic interface as well as the influence of charge carrier mobility are discussed. The behaviour of the system at various temperatures is included as a parameter study. Lastly the influence of a dipole layer situated at the heterojunction on the performance of the solar cell is studied.

2 General aspects of solar cells

2.1 Working principle of solar cells

Solar cells are devices that convert radiation energy into electrical energy. They consist of a translucent top contact, a bottom contact with a different workfunction and a semiconducting layer in between. The structure of the active layer varies widely. A great number of different layouts and material combinations are being tested. Mainly, one can separate between solar cells operating solely either on inorganic or organic semiconductors and devices working with a mixture of both called hybrid cells. The layout therein can range from simple planar heterojunctions over comblike structures [29] to even inorganic nanoparticles dispersed in an organic matrix [30].

The main differences between organic and inorganic semiconductors are (i) charge carrier mobility, (ii) densities, (iii) number of intrinsic charge carriers and (iv) electron and hole generation. In inorganic solar cells the charge carrier densities as well as the mobilities are orders of magnitudes higher than in organic materials. Also, there are no intrinsic charge carriers in organic semiconductors. In inorganic semiconductors a free electron-hole pair is created instantaneously when a photon is absorbed. Light absorption in an organic semiconductor on the other hand induces the generation of a bound electron-hole pair, called exciton. The are electrically neutral structures and are spread over an area of one to several molecules. Excitons cannot dissociate by thermal activation as their binding energy is far larger than the thermal energy at room temperature. The only way to create a free electron-hole pair out of an exciton is dissociation at a donor-acceptor interface, if the HOMO and LUMO level offsets are greater than the exciton binding energy. In this case it is energetically possible for the exciton to dissociate.

Common to all solar cells is that the charge carriers, no matter how they were generated in the first place, need to be extracted to the contacts. The resulting electric field accelerates the charges to their respective contacts. Figure 2.1 shows a typical I-V characteristic of a solar cell.

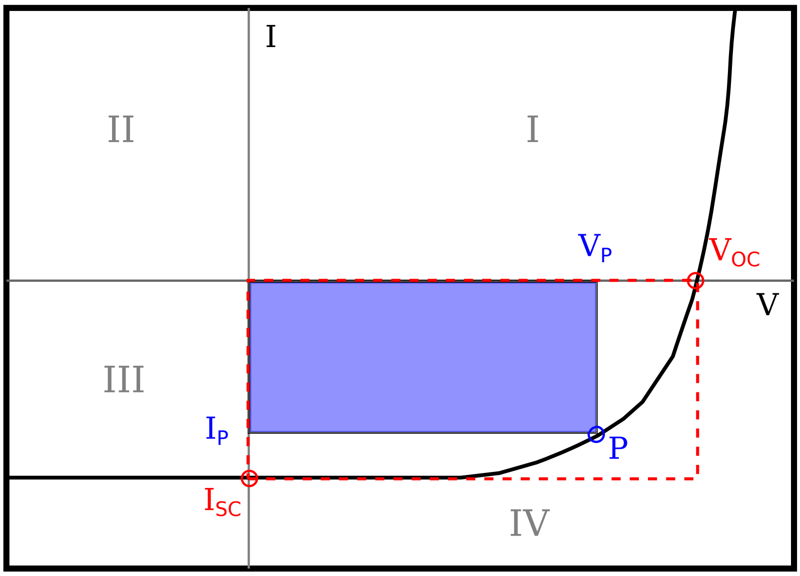

Figure 2.1: The operation regimes of a solar cell. They are (III) reverse bias, (IV) solar cell mode and (I) forward bias. The short circuit current I_{sc}, the open circuit voltage V_{oc} and the maximum power point P, defined by I_P and V_P are shown.

The The plot is divided into four quadrants. The interesting one is the fourth, the power quadrant. It is characterized by a negative current and positive applied voltage. In this configuration power is generated in the solar cell. The characteristic currents and voltages indicated in the plot are easily explained. The quantity I_{sc} is called the short circuit current. It is the current measured, when no voltage is applied. The open circuit voltage V_{oc} on the other hand is defined as the voltage, at which there is no current flow $I = 0$. Other important quantities for describing solar cells are the so-called maximum power point P, defined by the voltage V_P and the current j_P and the fill factor FF. The maximum power point is already defined by its name. It is the point on the I-V curve, at which maximal power can be gained from the device. Electrical power is defined as the product of current and voltage.

The fill factor is defined as the ratio of the power in the maximum power point to the product of the short circuit current and the open circuit voltage

$$FF = \frac{I_P V_P}{I_{sc} V_{oc}} \, .$$

The theoretical limit for the efficiency of a single layer solar cell with AM 1.5 irradiation is $\eta \approx 33\,\%$ [16]. This number is calculated by considering the influence of the bandgap energy. Small bandgap semiconductors absorb nearly all incoming photons, resulting in a large current, but their open circuit voltage, which is limited by the bandgap is rather low. A semiconductor with a very large bandgap on the other hand shows a high open circuit voltage, yet the achievable maximum current is quite weak. With the optimum bandgap energy the afore mentioned efficiency of

33 % can be reached.

Energy level alignment

Again considering Fig. 2.1, the energy level alignments in the different quadrants will be discussed here briefly. We start in the third quadrant. The according potential landscape is shown schematically in Fig. 2.2.

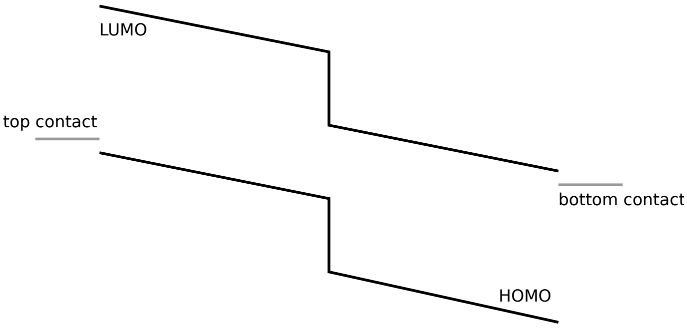

Figure 2.2: Energy level alignment in the device for negative applied voltages. The contact workfunctions are coloured grey, the HOMO and LUMO levels black. The workfunction of the top contact (on the right) is shifted above the workfunction of the bottom contact (right).

In In these plots electrons move downwards along the LUMO level, holes move upwards in the HOMO level.

The top contact, drawn on the left hand side has a higher potential than the bottom contact. The LUMO level lies above the HOMO level. Both are inclined downwards from the top contact to the bottom contact. Electrons are accelerated down the slope towards the bottom contact, holes in the opposite direction towards the top contact. Both can gain energy by crossing the jump at the donor acceptor interface.

At zero applied voltage the short circuit condition is reached. The top and bottom electrode are just connected. This forces the occupation levels of the two contacts to the same energetic level, resulting in the potential landscape shown in Fig. 2.3.

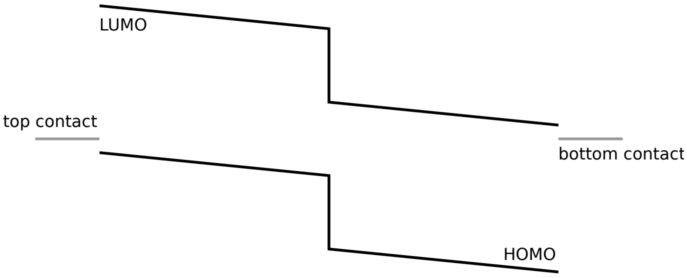

Figure 2.3: Energy level alignment in the device for zero applied voltages, called short circuit condition. The workfunctions of the contacts align at the same energy. The HOMO and LUMO levels are still tilted.

The contact workfunctions are aligned, the slopes of the HOMO and LUMO levels are weaker but still oriented in the same direction as before. Drift is still the main driving force.

If the external voltage is increased further to positive values, the bottom contact lies energetically higher than the bottom contact. The potential difference gradually increases until the open circuit condition is reached. The according energy landscape is depicted in Fig. 2.4.

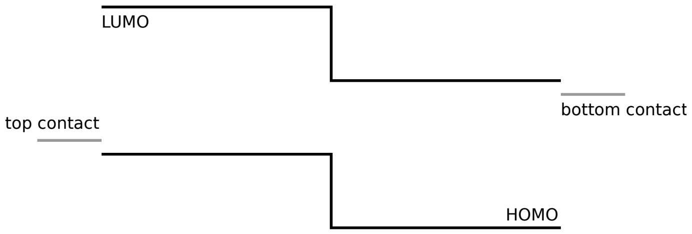

Figure 2.4: Energy level alignment in the device for open circuit conditions. The applied external voltage exactly compensates the built-in voltage. Consequently the HOMO and LUMO levels are completely flat in either half of the device. Charge carriers can only move diffusively, there is no drift force.

In this scenario no current flows. The HOMO and LUMO levels are completely flat, because the external voltage exactly compensates the built-in voltage V_{bi} given by the difference of the two contact workfunctions ϕ

$$V_{bi} = \phi_{anode} - \phi_{cathode} \,.$$

Actually, in this configuration in organic solar cells there is still some current flow, caused by diffusion. As explained in more detail in Section 2.2, charge carriers in organic solar cells are generated solely at the donor-acceptor interface. If there is no electric field extracting them to the contacts they still move away from the high density area at the interface by diffusion. And importantly, they diffuse towards the right contacts as they can not overcome the energetic barrier posed by the interface. In organic solar cells the external voltage has to be a little higher than according to the flat band condition in order to stop all current flow.

If the external voltage is still increased more, the slope of the HOMO and LUMO transport levels changes sign. The levels now rise towards the bottom contact. This can be seen in Fig. 2.5.

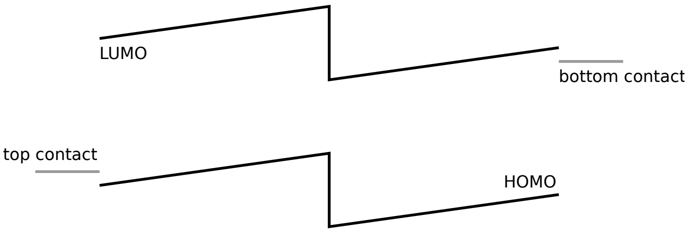

Figure 2.5: Energy level alignment in the device for applied voltages greater than the open circuit voltage. The transport levels are tilted in the other direction. Charge carriers drift towards the wrong contact. If the tilt is large enough they can overcome the potential barrier at the interface.

Charge Charge carriers now drift to the respective opposite contact. Many more carriers are injected from the contacts into the semiconductor as are generated by light absorption. They have a high enough potential energy to cross the interface barrier on their way to the other contact. The current flows in the opposite direction through the device, it has a positive sign. This corresponds to the first quadrant. No power is generated in this regime.

2.2 Organic solar cells

Organic solar cells are in many ways different from inorganic ones. The material parameters, the efficiency, the charge carrier mobilities as well as the charge transport itself differ. But the main difference, which is very relevant for device layouts and simulations, is the charge carrier generation process. In inorganic solar cells photons hit the semiconductor and generate instantaneously an electron-hole pair. In organic devices on the other hand, light creates excitons in the semiconductor. They are bound electron-hole pairs with a binding energy of $E_b \approx 0.3-0.5\,\mathrm{eV}$, which act electrically neutral. They therefore are completely uninfluenced by any electric field in the device and can only move by means of diffusion. If they encounter an acceptor-donor interface, with an energy offset greater than the exciton binding energy, they dissociate immediately into a separate electron and hole [3]. How this process takes place is still not understood in detail. It is, however, logical that the excitons need to gain more energy by dissociation than their binding energy. The thermal energy at room temperature, which is about 25 meV is not nearly sufficient to induce dissociation. The dissociation process is schematically shown in the form of an energy diagram in Fig. 2.6.

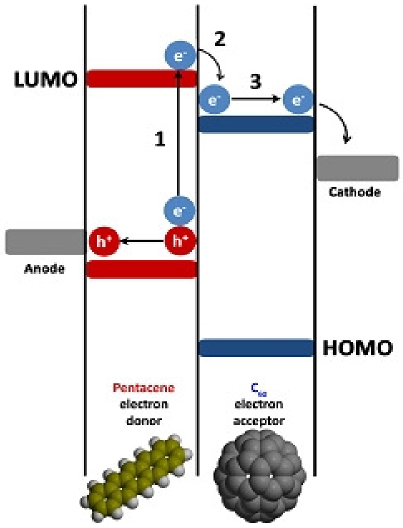

Figure 2.6: Schematic illustration of the exciton dissociation process. The exciton diffuses to a donor-acceptor interface, where the electron is transferred to the acceptor in the LUMO level and the hole to the donor in the HOMO level. They then move towards their respective contacts [2].

If they do not reach an interface during their lifetime, which is roughly $\tau \approx 10^{-9}$ s, they recombine and are lost for energy production.

After dissociation the electrons and holes have to be extracted to the contacts. They can travel by diffusion and drift, where the diffusion is a not negligible part in the charge carrier movement. In Fig. 2.7 the generation profiles for an inorganic and an organic solar cell are depicted.

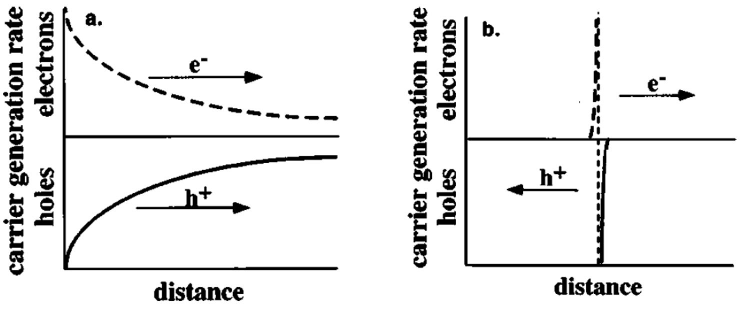

Figure 2.7: Illustration of the charge carrier generation profile in inorganic (left) and organic (right) solar cells. In inorganic solar cells free electrons and holes are created according to Lambert-Beer's law. They both diffuse in direction from the top to the bottom of the device in the same direction. In organic solar cells free charge carriers are only generated at a donor acceptor interface. Electrons and holes diffuse in opposite directions [3].

In inorganic solar cells, on the left in Fig. 2.7, free electron-hole pairs are created throughout the device according to Lambert-Beer's law (4.39), meaning the electron and hole concentration decreases steadily from the top of the device to the bottom. This, in consequence, induces both electrons and holes to diffuse away from the top downwards. This diffusion current does not aid the process of charge extraction towards the contacts, because electrons and holes diffuse in the same instead of opposite directions.

In contrast, the generation profile in organic solar cells, shown in Fig. 2.7 on the right, is centered sharply around the donor-acceptor interface. In organic solar cells absorbed light generates excitons, which only dissociate at the donor-acceptor interface. Hence, there is a strong concentration of electrons and holes on either side of the interface. The interface functions as a potential barrier because of the offset in the HOMO/LUMO levels. For that reason electrons can not diffuse into the acceptor and holes are unable to diffuse into the donor. The diffusion away from the crowded interface extracts electrons and holes to separate contacts. Thus, diffusion plays an active part in charge extraction to the contacts in organic solar cells.

2.3 Inorganic solar cells

Nearly all commercial solar cells are of the inorganic type. Most of them consist of monocrystalline silicon or gallium-arsenide. When they are illuminated, an absorbed photon directly creates a free electron-hole pair. It is not bound in an excitonic state as in organic semiconductors. For the extraction of charges to the contacts only drift forces are responsible. Yet for inorganic solar cells no external voltage needs to be applied. Their working principal is based on a pn-junction. If a p-type doped and an n-type semiconductor are connected, a pn-junction is formed. It is schematically illustrated in Fig. 2.8.

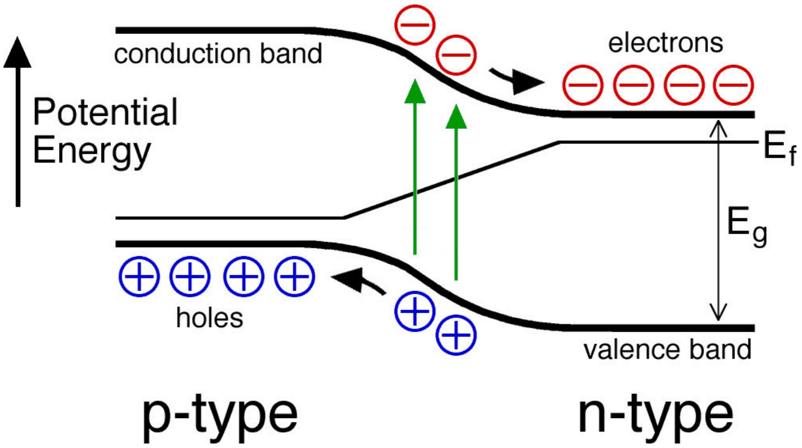

Figure 2.8: At a pn-junction the valence and conduction band get bent, resulting in an internal electric field [1].

A consequence of the band bending at a pn-junction is an internal electric field.

This effect is exploited in solar cells for extraction of charge carriers.

The before mentioned high mobility in inorganic semiconducting crystals allows electrons to move comparatively long distances without noticeable loss. This enables a different design of the top electrode. A metal grid can be applied to the top silicon layer allowing enough light to penetrate to the semiconductor. In organic solar cells a continuous planar contact is necessary. Therefore, a transparent and electrically conducting material has to be used for the top electrode, which is rather expensive. Mostly indium-tin-oxide (ITO) is chosen.

The nowadays highest efficiency achievable is around $\eta \approx 36\,\%$. This value can be reached by multilayer device layouts of very pure semiconducting crystals. A great disadvantage of inorganic solar cells, however, is the immense amount of energy used in the production and recycling process compared to the power generated by the solar cell. The critical step therein is the purification of silicon.

2.4 Hybrid solar cells

The active layer of hybrid solar cells contains organic and inorganic components. In the inorganic semiconductor light generates free electrons and holes whereas in the organic layer excitons are created, a certain percentage of which dissociates at the donor acceptor interface. To increase the fraction of separating excitons the distance between generation regions and the interface should be as short as possible. An ideal structure, therefore, shows an interdigitated donor-acceptor phase [29]. Alternatively, nanoparticles dispersed in a matrix also fulfill this criterion [30]. The challenge for the nanoparticle structure is to ensure percolation to enable charge carriers to travel to their collecting contact solely in one or the other material. If the nanoparticle density is too low, charge carriers get trapped in them and are lost for transport [31].

2.5 Charge carrier transport in organic semiconductors

The semiconducting properties of some organic materials are caused by a π-conjugated electron system. The individual carbon atoms of the chain undergo an sp^2 hybridization. It is schematically shown in Fig. 2.9 for an ethene molecule (C_2H_4).

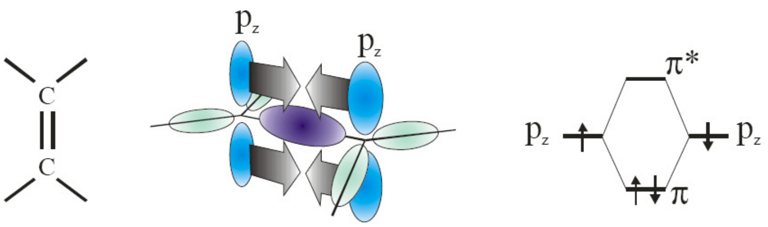

Figure 2.9: Illustration of an sp^2 hybridization in an ethene molecule. One σ- and two π-bonds are formed [9].

The carbon atoms in the chain are bound by a σ- and a π-bond. The σ-bond is located on the rotation axis between the two atoms. It is invariant to rotation of either atom around the binding axis. The two π-bonds are also formed in the same plane as the σ-bond, yet they lie below and above the former. They are not rotationally invariant. The π-bond is created by a more or less strong overlap of the p_z orbitals of the carbons. The single orbitals of each atom form two joint orbitals π and $\pi*$, where the former represents the bonding and the latter the antibonding molecular orbital. By this form of bonding the electrons are effectively delocalized over the whole carbon chain. The longer the chain the more orbitals are formed, see Fig. 2.10.

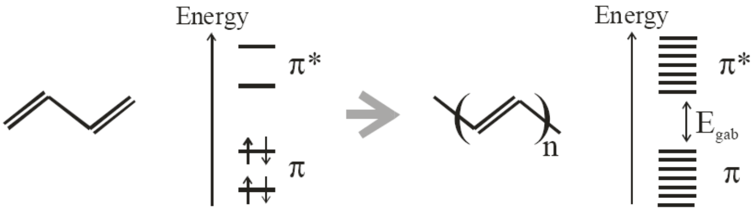

Figure 2.10: Formation of bonding (π) and anti bonding ($\pi*$) orbitals in a polymer chain. The longer the chain the more orbitals are formed [9].

The highest of the bonding orbitals is called HOMO and the lowest of the antibonding ones LUMO. HOMO is the acronym of Highest Occupied Molecular Orbital and LUMO of Lowest Unoccupied Molecular Orbital.

An organic semiconductor has no real band structure like an inorganic crystal. Electrons are excited into the LUMO level instead of the conduction band. Accordingly holes travel in the HOMO level.

In a polymer solution not all chains have exactly the same length. There is a distribution of chain lengths with a certain width. Accordingly the HOMO and LUMO levels of the individual molecules do not lie at the exact same energy. This results in a Gaussian shaped density of states at these levels, depicted in Fig. 2.11, instead of a delta peak.

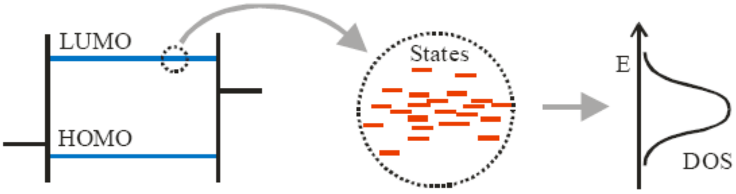

Figure 2.11: Due to a distribution of chain lengths the energy of the individual HOMO and LUMO levels varies. This leads to a Gaussian shaped density of states instead of sharply defined transport levels [9].

The charge carrier transport process as such can be generally divided into the intrachain and the interchain transport. By the former one means the charge carrier transport along one molecule, by the second the transport process from one molecule to the next. The intrachain transport is enabled by the conjugated system of π orbitals. Electrons can easily move along a polymer chain. The transition from one molecule to the next is described by interchain transport. It has the characteristics of a hopping transport, where the orbital overlap of the partaking molecules plays a dominant role. In fact, it determines the mobility of the charge carriers. A main feature of hopping transport is its characteristic temperature dependence. The process is thermally activated, the hopping rate increases with temperature. This explains the positive temperature coefficient of conductivity for organic semiconductors.

Generally, the interchain transport is a limiting factor for the conductivity. Charge transport along one molecule takes place much faster. As the individual polymer chains in a semiconductor are randomly oriented, charge carriers travel with the same mobility in every direction.

For drift-diffusion simulations, however, the individual transport processes are not considered separately. All influences are appraised and included in one parameter, the charge carrier mobility μ. The hopping process for instance can be described by the following field-dependent mobility of the Poole-Frenkel form $\mu = \mu_0 \exp\left(\gamma\sqrt{|E|}\right)$ [12]. Here, μ_0 is the mobility without electric field E and γ is a constant.

There are a number of temperature and field-dependent models for the charge carrier mobility, yet in this work the simulations were done with fixed mobilities for each type of charge carrier in each semiconductor.

It should also be mentioned that there are no intrinsic free charge carriers in organic semiconductors. They either have to be generated by illumination and subsequent absorption or by injection from the device contacts. Both processes take place in solar cells.

Drift-diffusion equation for electrons and holes

In a drift-diffusion model two driving forces for charge carrier movement are considered, drift and diffusion, as the name already states. Drift describes electron and hole movement due to an acting electric field. Thereby, electrons and holes are accelerated in opposite directions.

Diffusive transport is caused by a gradient in the charge carrier density. Electrons travel away from dense electron concentrations on the one hand because of the acting electrostatic forces and on the other hand because of the concentration gradient. The same applies for holes.

As electrons moving in one direction and positively charged holes moving in the opposite direction generate a current in the same direction, namely the one, in which the holes are traveling, the total current can be written as the sum

$$J(x,y,t) = J_n(x,y,t) + J_p(x,y,t)\,,$$

where J_n and J_p are described by [10]

$$J_n(x,y,t) = q\,n(x,y,t)\mu_n(x,y)E_n(x,y,t) + q\,D_n(x,y)\nabla n(x,y,t)\,, \tag{2.1}$$

$$J_p(x,y,t) = q\,p(x,y,t)\mu_p(x,y)E_p(x,y,t) - q\,D_p(x,y)\nabla p(x,y,t)\,. \tag{2.2}$$

Here $n(x,y,t)$ and $p(x,y,t)$ denote the position- and time-dependent electron/hole concentrations and $E_{n/p}$ the acting electric field. The respective electron/hole mobilities and diffusion constants are denoted by $\mu_{n/p}$ and $D_{n/p}$. They are connected by the Einstein relation

$$D_{n/p} = \frac{k_B T}{q}\mu_{n/p}(x,y)\,,$$

with the Boltzmann constant k_B, the temperature T and the positive elementary charge q. These drift-diffusion equations are coupled to the continuity equations for electrons and holes

$$\frac{\partial n(x,y,t)}{\partial t} - \frac{1}{q}\nabla J_n(x,y,t) = G(x,y,t) - R(x,y,t)\,, \tag{2.3}$$

$$\frac{\partial p(x,y,t)}{\partial t} + \frac{1}{q}\nabla J_p(x,y,t) = G(x,y,t) - R(x,y,t)\,, \tag{2.4}$$

with the charge carrier generation and recombination rates G and R [11]. They also are position and time dependent.

The electric field $E_{n/p}$ is calculated from the effective electrostatic potential $\Psi_{n/p}$, described in the next section

$$E_{n/p}(x,y,t) = -\nabla\Psi_{n/p}(x,y,t)\,. \tag{2.5}$$

Equations (2.1), (2.2), (2.3), (2.4) will be derived from the Boltzmann equation in Chapter 3.

Poisson equation

The Poisson equation

$$\nabla[\varepsilon_0\varepsilon_r(x,y)\nabla\psi(x,y,t)] = -\rho(x,y,t) = q\,[n(x,y,t) - p(x,y,t)]\,, \tag{2.6}$$

is used to calculate the position-dependent electrostatic potential $\psi(x,y,t)$ from the charge densities $n(x,y,t)$, $p(x,y,t)$ and the relative dielectric permittivity $\varepsilon_r(x,y)$.

At this point the charge transport along the HOMO and LUMO levels has to be considered. Electrons travel at higher energetic levels than holes. Thus, we have to modify the electrostatic potential in the following way

$$\Psi_{n/p}(x,y,t) = \psi(x,y,t) + \frac{\Theta_{n/p}(x,y)}{q}\,. \tag{2.7}$$

In equation (2.7) so-called the generalized potential $\Psi_{n/p}(x,y,t)$ for electrons and holes was introduced. The HOMO and LUMO levels of the donor and acceptor are denoted by $\Theta_{n/p}$. The generalized potential causes the electrostic force acting on electrons and holes, respectively. It is used to calculate the electric field (2.5) occuring in equations (2.1) and (2.2).

Exciton movement

As excitons are electrically neutral, they can not be influenced by electric fields. Hence, the only acting force is caused by the gradient in the exciton density, causing diffusion. The exciton flux density can be written as

$$\Phi_{ex}(x,y,t) = -k_BT\mu_{ex}\nabla ex(x,y,t)\,, \tag{2.8}$$

where $ex(x,y,t)$ is the exciton density distribution and μ_{ex} the exciton mobility [11]. It is coupled to the exciton diffusion constant D_{ex} by

$$\frac{k_BT}{q}\mu_{ex} = D_{ex}\,, \tag{2.9}$$

with the Boltzmann constant k_B, the temperature T and the elementary charge q. In equation (2.8) there is only a diffusion term but no drift term. The continuity equation for excitons is given by

$$\frac{\partial ex(x,y,t)}{\partial t} + \frac{1}{q}\nabla\Phi_{ex}(x,y,t) = G_{ex}(x,y,t) - R_{ex}(x,y,t) - G(x,y,t)\,, \tag{2.10}$$

with G_{ex} and R_{ex} the exciton generation and recombination rates. The symbol G denotes the electron and hole generation rate. It appears in the exciton continuity equation as a loss term.

2.6 Solar spectrum

In the sun, nuclear fusion from hydrogen to helium creates energy according to the famous formula $E = mc^2$, describing the equivalence of mass and energy. After a very long time photons reach the sun's surface and leave the star. Their energy ranges from the infrared to the ultraviolet. After a journey of roughly eight minutes the photons reach the earth, where they first encounter the atmosphere. On their way through, processes like reflection and absorption occur, diminishing the light intensity reaching the surface of the earth. At the equator light hits the earth at almost 90° and therefore travels the shortest distance through the atmosphere. The intensity reaching the surface is high. Regions lying nearer to either pole receive lower intensities due to longer light paths through the atmosphere and higher impact angles. This is shown schematically in Fig. 2.12.

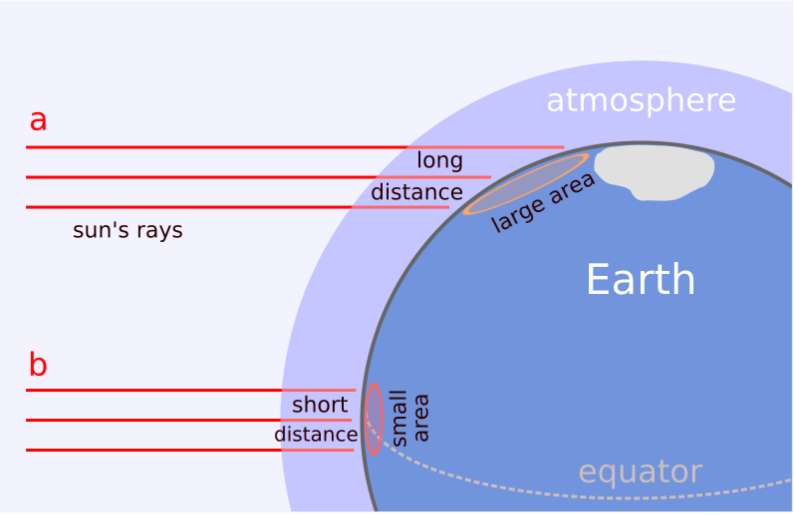

Figure 2.12: Illustration of the path and incidence angle of incoming light. The intensity reaching the surface of the earth is highest at the equator and decreases towards the poles [5].

For the simulation the so-called AM 1.5, or air mass 1.5, spectrum was used. It is plotted in Fig. 2.13.

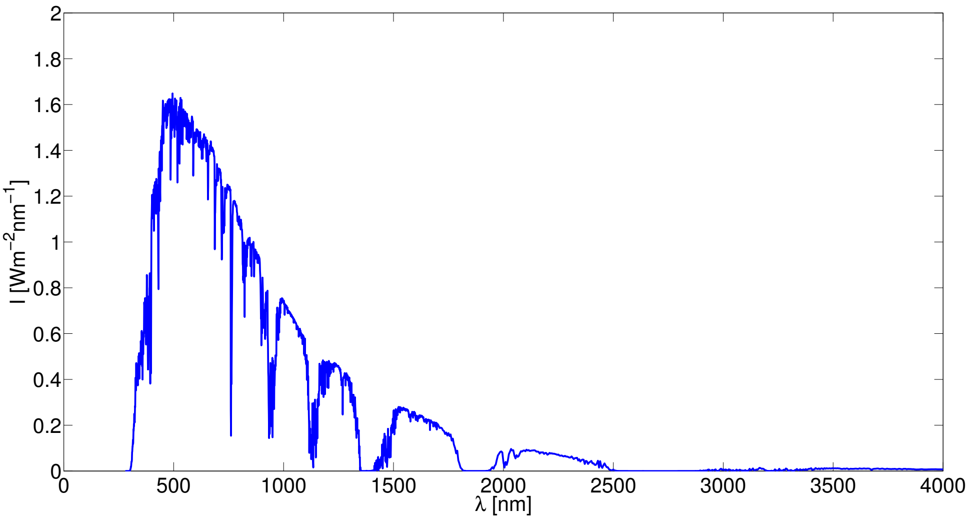

Figure 2.13: Wavelength dependence of the AM 1.5 spectrum used for the simulations. It includes the influences of a diffusive sky and diffuse light reflection off the ground at 48.9° latitude [4].

It shows the spectral radiation from the sun reaching the surface of the earth at 48.9° of latitude. It includes the impact of a diffusive sky and light reflection off the ground.

2.7 Charge carrier generation

Light penetrating an absorbing medium loses intensity on the way. The intensity left after a distance x from the starting point is given by Lambert Beer's law of absorption [47]

$$I(x) = \int_0^{\lambda_{max}} I_0(\lambda) \exp\left[-\alpha(\lambda) x\right] d\lambda\,, \tag{2.11}$$

with a wavelength dependent absorption coefficient $\alpha(\lambda)$ and $I_0(\lambda)$ the solar spectrum AM 1.5 described in the previous section. The unit of the intensities in equation (2.11) is $\mathrm{Wm}^{-2}\mathrm{nm}^{-1}$. The integration interval ends at λ_{max}, the maximum wavelength, which corresponds to the bandgap energy E_{gap}.

When a photon hits a molecule it excites it from the state S_0 to S^*. The molecule then thermalizes back into the state S_1. The surplus energy $S_1 - S_0$ is released in form of a strongly bound electron-hole pair, called an exciton. This process is illustrated schematically in Fig. 2.14.

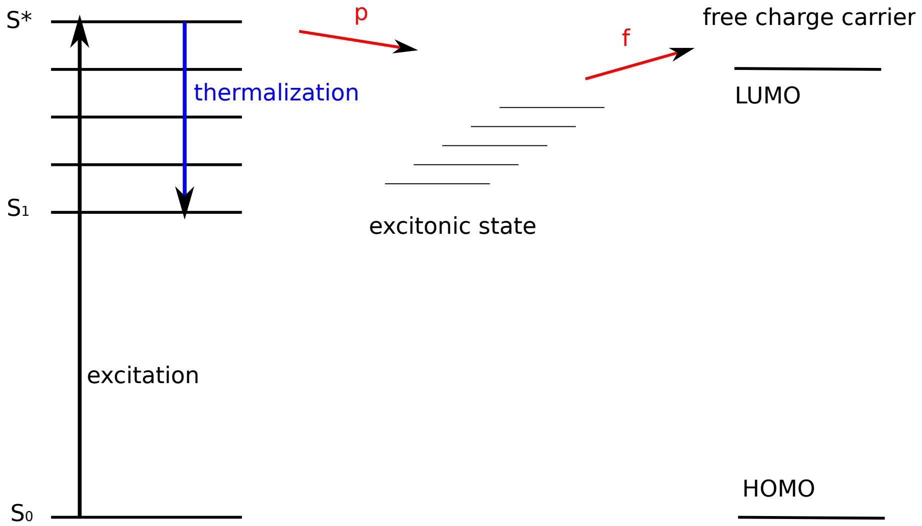

Figure 2.14: Schematic illustration of the processes from an incoming photon to a free charge carrier. A photon excites a molecule from the ground state S_0 to an excited state S^*. After thermalizing to the lower state S_1 an exciton is formed with a certain probability p. It then dissociates into free charge carriers with the probability f.

The exciton binding energy lies at roughly $0.3 - 0.5\,\mathrm{eV}$. Mainly two different kinds of excitons exist, the Frenkel exciton and the Wannier-Mott exciton. The first kind is very strongly bound with the afore mentioned binding energy. Therefore, the mean distance between electron and hole is rather short. They may even be located at the same molecule. Frenkel excitons occur mostly in materials with small dielectric constants, where the Coulomb interaction is strong.

The Wannier-Mott exciton on the other hand is bound comparatively loosely. A typical binding energy is of the order of $0.01\,\mathrm{eV}$. As a result the Wannier-Mott exciton may be dispersed over a few molecules. This type of exciton is mainly found in semiconductors with high dielectric constants and small band gaps.

For our simulations only Frenkel excitons are of relevance. After generation, the excitons can diffuse for a certain time, their lifetime $\tau_{ex} = 10^{-9}\,\mathrm{s}$ (see Section 4.4). The excitons can not dissociate in the bulk of the semiconductor as their thermal energy, $E_{th} \approx 25\,\mathrm{meV}$ is far to small to overcome the binding energy. They can only dissociate into a free electron-hole pair at a donor-acceptor interface, if the HOMO/LUMO offset between donor and acceptor is greater than the exciton binding energy.

3 Derivation of the drift-diffusion equations

3.1 The Boltzmann transport equation

Charge carriers in a semiconductor move in the position and momentum space due to their velocity and existing electric fields. We now consider the paths the particles take in the six-dimensional phase space which are called trajectories. In the next step we try to find an expression for the probability of finding a particle at position $x \in \mathbb{R}^3_x$, with momentum $p \in \mathbb{R}^3$ at time $t > 0$. This probability is given by the distribution function. We denote it by the symbol $F \in \mathbb{R}^3$. As it is a function of position, momentum and time it should be correctly written as $F(x, p, t)$. For the first considerations we will not include scattering between particles among themselves or with the lattice. It this case, as the particles move only along their trajectories as time progresses, we can state that the probability of finding a particle at a specific point $A = (x, p)$ along the trajectory at time t is the same as the probability of finding it at an earlier position $A' = (x - vdt, p - \mathcal{F}dt)$ along the same trajectory at the according time $t - dt$. Putting this consideration in the shape of an equation results in

$$F(x, p, t) = F(r - vdt, p - \mathcal{F}dt, t - dt)\,. \tag{3.1}$$

This holds if the particle moves with velocity $v \in \mathbb{R}^3_{v'}$ in position space and a force $\mathcal{F} \in \mathbb{R}^3$ acts making it change its momentum accordingly.

We now expand (3.1) into a Taylor series with respect to powers of dt. We perform the expansion in dt up to first order around $dt = 0$ and get

$$\begin{aligned} F(x,p,t) = F(x,p,t) + \left(-v\cdot\nabla_x F - \mathcal{F}\cdot\nabla_p F - \frac{\partial F}{\partial t}\right)\,, \\ v\cdot\nabla_x F + \mathcal{F}\cdot\nabla_p F + \frac{\partial F}{\partial t} = 0\,, \\ \frac{\mathrm{d}F}{\mathrm{d}t} = 0\,, \end{aligned} \tag{3.2}$$

where $\frac{dF}{dt}$ denotes the total differential of F with respect to the time t. Equation (3.2) states that the occupation probability along a trajectory does not change with time. If the state is occupied at time $t = 0$ then it will be occupied at all times t. This is only a realistic description of the system as long as scattering processes are excluded. Through such an event particles can be scattered from one trajectory to another. The momentum of the involved particle is instantaneously changed from p'

to p, whereas the position only changes afterwards according to the new momentum. A second influence on the distribution function are source and sink terms. Sources, sinks and scattering events together can populate an until then empty state, or depopulate a state. Including these terms in equation (3.2) results in

$$\frac{\partial F}{\partial t} + v \cdot \nabla_x f + \mathcal{F} \cdot \nabla_p F = \left.\frac{\partial F}{\partial t}\right|_{coll} + s(x,p,t)\,, \tag{3.3}$$

where s includes source and sink terms. The steps up to this point are performed in more detail in [18]. Now we perform a transformation of variables from p to v

$$\frac{\partial F}{\partial p} = \frac{\partial F}{\partial v}\frac{\partial v}{\partial p}\,,$$

where we have to consider that the momentum $p = mv$, where m denotes the particle mass. We also replace the force $\mathcal{F}$ by the electrical field $E \in \mathbb{R}^3$ acting on a particle with the charge e. With this equation (3.3) reads

$$\frac{\partial F}{\partial t} + v \cdot \nabla_x F + \frac{e}{m} E \cdot \nabla_v F = \left.\frac{\partial F}{\partial t}\right|_{coll} + s(x,p,t)\,. \tag{3.4}$$

The rate of scattering a particle with position vector x, and velocity vector v' into a state with position vector x, and velocity vector v at time t is written as $P(x, v' \to v, t)$. It is assumed to be proportional to the occupation probability $F(x, v', t)$ of the starting state (x, v') at time t. Equally, one has to assume that $P(x, v' \to v, t)$ is proportional to $1 - F(x, v, t)$, the probability, that the end state (x, v) is unoccupied at time t. Thus we have

$$P(x, v' \to v, t) = s(x, v', v)F(x, v', t)(1 - F(x, v, t))\,, \tag{3.5}$$

with the scattering rate s. To define s precisely, $s(x, v', v)dv'$ is the probability that a particle is scattered from the state (x, v') into the state (x, v) per unit of time, with v' belonging to the volume element dv' around v'. The form of this scattering rate is determined by the underlying physics of the considered scattering situation.

The distribution function $F(x, v, t)$ can increase by particles being scattered form any state (x, v') into the state (x, v) and it decreases by particles being scattered out of the state (x, v) into any other state (x, v'). Therefore, the rate of change of $F(x, v, t)$ is given by the integral over the difference of those two rates taken over the whole velocity space, resulting in

$$Q(F) := \left(\frac{dF}{dt}\right)_{\mathrm{coll}}(x, v, t) = \int\limits_{\mathbb{R}^3_{v'}} [P(x, v' \to v, t) - P(x(v \to v', t)]dv'\,. \tag{3.6}$$

Inserting (3.5) into (3.6) gives the equation

$$Q(F)(x,v,t) = \int\limits_{\mathbb{R}^3_{v'}} [s(x,v',v)F'(1-F) - s(x,v,v')F(1-F')]dv' \,, \tag{3.7}$$

by using the abbreviations

$$F = F(x,v,t), \qquad F' = F(x,v',t) \,.$$

Omitting external sources, equation (3.4) in short notation reads by taking into account (3.7):

$$\partial_t F + v \cdot \nabla_x F + \frac{e}{m} E \cdot \nabla_v F = \int\limits_{\mathbb{R}^3_{v'}} [s(x,v',v)F'(1-F) - s(x,v,v')F(1-F')]dv',$$

$$x \in \mathbb{R}^3_x \,, \quad v \in \mathbb{R}^3_v, \quad t > 0 \,. \tag{3.8}$$

Velocity and wave vector are directly related to each other by $k = \frac{mv}{\hbar}$. We therefore write the above equations in terms of wave vector $k \in \mathbb{R}^3$. The collision integral then reads

$$Q(F)(x,k,t) = \int\limits_{B} [s(x,k',k)F'(1-F) - s(x,k,k')F(1-F')]dk' \,, \tag{3.9}$$

where we have to integrate over the first Brillouin zone B and to define $F = F(x,k,t)$ as well as $F' = F(x,k',t)$. The Boltzmann equation is now given by

$$\partial_t F + v(k) \cdot \nabla_x F + \frac{e}{\hbar} E \cdot \nabla_k F = Q(F),$$

$$x \in \mathbb{R}^3_x, \quad k \in B, \quad t > 0 \,. \tag{3.10}$$

Integrating the collision integral with respect to the wave vector k over the first Brillouin zone results in

$$\int_B Q(F)dk = \int\limits_B \int\limits_B [s(x,k',k)F'(1-F) - s(x,k,k')F(1-F')]dk'dk = 0 \,. \tag{3.11}$$

This shows that considering the whole state space no particles are destroyed or generated through collision processes. It ensures the very important conservation of particles.

Another significant property of the collision operator is the so-called principle of detailed balance. It states that in thermal equilibrium as many particles are scattered into a state (x,k) as are scattered out of it. This means that the scattering probabilities into a state and out of it are equal:

$$s(x,k',k)F'_e(1-F_e) = s(x,k,k')F_e(1-F'_e) \,. \tag{3.12}$$

Here, F_e denotes the number density in thermal equilibrium. It is given by the Fermi-Dirac statisitcs:

$$F_e(k) = F_D\left(\frac{\varepsilon(k) - \varepsilon_F}{k_B T}\right), \tag{3.13}$$

$$F_D(u) = \frac{1}{1 + \exp(u)}, \tag{3.14}$$

where $\varepsilon(k)$ is the considered energy band of the semiconductor, ε_F denotes the Fermi energy, k_B the Boltzmann constant and T the lattice temperature. Inserting (3.13), (3.14) into (3.12) and doing a few basic calcutions gives

$$s(x,k',k)(F_e' - F_e F_e') = s(x,k,k')(F_e - F_e F_e'),$$

and further

$$\begin{aligned} s(x,k,k') &= s(x,k',k)\frac{F_e' - F_e F_e'}{F_e - F_e F_e'} \\ &= s(x,k',k)\frac{\frac{1}{F_e} - 1}{\frac{1}{F_e'} - 1} \\ &= s(x,k',k)\frac{1 + \exp\left(\frac{\varepsilon(k) - \varepsilon_F}{k_B T}\right) - 1}{1 + \exp\left(\frac{\varepsilon(k') - \varepsilon_F}{k_B T}\right) - 1} \\ &= \exp\left(\frac{\varepsilon(k) - \varepsilon(k')}{k_B T}\right) s(x,k',k). \end{aligned} \tag{3.15}$$

Knowing the scattering rate $s(x,k,k')$, a collision frequency λ can be defined by

$$\lambda(x,k) := \int\limits_B s(x,k,k')dk',$$

which is reciprocal to the relaxation time

$$\tau(x,k) := \frac{1}{\lambda(x,k)}.$$

The relaxation time gives the average time between two consecutive collisions at the state (x,k). It also represents the time scale on which the number density evolves or relaxes towards an equilibrium state. Hence, the name relaxation time.

3.1.1 Low density approximation

In many considered cases the number density F of particles is small

$$0 \leqslant F(x,k,t) \ll 1\,. \tag{3.16}$$

In the low density approximation, $1-F(x,k,t)\approx 1$, the collision integral (3.9) reads

$$Q_L(F)(x,k,t) = \int\limits_B \left[s(x,k',k)F' - s(x,k,k')F\right]dk'\,. \tag{3.17}$$

The conservation of particles, ensured by the condition

$$\int\limits_B Q_L(F)dk = 0\,,$$

still holds. The principle of detailed balance in the low density approximation is now given by

$$s(x,k',k)F_e' = s(x,k,k')F_e\,. \tag{3.18}$$

In the low density approximation the Fermi-Dirac statistic can be approximated by the Maxwell distribution

$$M(k) = N^* \exp\left(-\frac{\varepsilon(k)}{k_BT}\right), \qquad N^* = \left[\int\limits_B \exp\left(-\frac{\varepsilon(k)}{k_BT}\right)dk\right]^{-1}. \tag{3.19}$$

We now are allowed to assume that the number density $F(x,k,t)$ in thermal equilibrium is described by the Maxwell distribution, $F_e = M(k)$ and the principle of detailed balance reads

$$s(x,k',k)M(k') = s(x,k,k')M(k)\,. \tag{3.20}$$

Inserting (3.19) into (3.20)

$$s(x,k',k)N^*\exp\left(-\frac{\varepsilon(k')}{k_BT}\right) = s(x,k,k')N^*\exp\left(-\frac{\varepsilon(k)}{k_BT}\right)$$

leads directly to the detailed balance relation

$$s(x,k,k') = \exp\left(\frac{\varepsilon(k)-\varepsilon(k')}{k_BT}\right)s(x,k',k)\,,$$

which is stated in (3.15). The scattering rate s can be rewritten in terms of the so-called collision cross section Φ:

$$s(x,k',k) = \Phi(x,k,k')\exp\left(\frac{\varepsilon(k')}{k_BT}\right). \tag{3.21}$$

As can be easily verified the collision cross section Φ is symmetric with respect to k and k'

$$\Phi(x,k,k') = s(x,k',k)\exp\left(-\frac{\varepsilon(k')}{k_BT}\right) \tag{3.22}$$

$$= s(x,k,k')\exp\left(\frac{\varepsilon(k')-\varepsilon(k)}{k_BT}\right)\exp\left(-\frac{\varepsilon(k')}{k_BT}\right) \tag{3.23}$$

$$= \Phi(x,k',k)\,. \tag{3.24}$$

Inserting (3.24) into (3.17), the collision integral is given by

$$Q_L(F)(x,k,t) = \int\limits_B \left[\Phi(x,k,k')\exp\left(\frac{\varepsilon(k')}{k_BT}\right)F' - \Phi(x,k,k')\exp\left(\frac{\varepsilon(k)}{k_BT}\right)F\right]dk'$$

$$= \int\limits_B \Phi(x,k,k')\left[\exp\left(\frac{\varepsilon(k')}{k_BT}\right)F' - \exp\left(\frac{\varepsilon(k)}{k_BT}\right)F\right]dk'\,. \tag{3.25}$$

3.1.2 The bipolar model

A semiconductor is characterised by the fact that the Fermi energy lies in the gap between the top of the valence band and the bottom of the conduction band, the so called bandgap. Furthermore, the difference between a metal and a semiconductor is the width of the bandgap. Semiconductors have by far smaller bandgaps than metals. This allows electrons to be thermally activated from the valence band into the conduction band. This process shows an exponential dependence on the temperature T. At room temperature, the conduction band is not completely empty anymore, but still rather scarcely populated by electrons. In the transition from the valence band to the conduction band, every electron leaves a so-called hole in the valence band. It is associated with a positive elementary charge. This ensures charge neutrality over the whole crystal.

Electrons can also be transferred to the conduction band by external energy sources, for example by shining light onto the semiconductor. Any process that transfers an electron from the valence band to the conduction band, leaving a hole in the valence band, is called generation of an electron-hole pair. The inverse process is called recombination of an electron-hole pair.

The concept of naming a not existing electron in the valence band a hole and assigning it with the elementary charge $q > 0$ is an easy and elegant way to describe the collective motion of the remaining electrons in the valence band. For more information on the basic physical properties of semiconductors the reader is referred to [21], [22].

In the following calculations, quantities corresponding to electrons will be denoted with the index n and holes with the index p. The number densities n and p are calculated from their distribution functions F_n and F_p, respectively:

$$n = \int_B F_n dk\,, \qquad p = \int_B F_p dk\,,$$

as are the current densities

$$J_n = -q \int_B v_n(k) F_n \, dk\,, \qquad J_p = q \int_B v_p(k) F_p \, dk\,,$$

with v_n, v_p the respective electron and hole velocities and $q > 0$ denoting the elementary charge. They are related to the band diagrams $\varepsilon_n(k)$ and $\varepsilon_p(k)$ by the relations

$$v_n = \frac{1}{\hbar} \nabla_k \varepsilon_n(k)\,, \tag{3.26}$$

$$v_p = -\frac{1}{\hbar} \nabla_k \varepsilon_p(k)\,. \tag{3.27}$$

The temporal evolution of the distribution functions is described by the Boltzmann equations

$$\partial_t F_n + v_n(k) \cdot \nabla_x F_n - \frac{q}{\hbar} E \cdot \nabla_k F_n = Q_n(F_n) + I_n(F_n, F_p)\,, \tag{3.28}$$

$$\partial_t F_p + v_p(k) \cdot \nabla_x F_p + \frac{q}{\hbar} E \cdot \nabla_k F_p = Q_p(F_p) + I_p(F_n, F_p)\,. \tag{3.29}$$

Hence, Q_n and Q_p are the electron and hole collision operators, modeling the short range particle interactions with each other and the environment. They are of the form (3.11) with the transition rates s_n and s_p, respectively. They satisfy the detailed balance relations according to the equations (3.20) and (3.19):

$$s_n(x, k, k') = \exp\left(\frac{\varepsilon_n(k) - \varepsilon_n(k')}{k_B T}\right) s_n(x, k', k)\,,$$

$$s_p(x, k, k') = \exp\left(\frac{\varepsilon_p(k) - \varepsilon_p(k')}{k_B T}\right) s_p(x, k', k)\,.$$

The operators I_n and I_p describe generation and recombination processes of electron-hole pairs. They are given by

$$I_n(F_n, F_p) = \int_B [g(x, k, k')(1 - F_n)(1 - F_p') - r(x, k, k') F_n F_p'] dk'\,, \tag{3.30}$$

$$I_p(F_n, F_p) = \int_B [g(x, k', k)(1 - F_n')(1 - F_p) - r(x, k', k) F_n' F_p] dk'\,, \tag{3.31}$$

where $g(x, k, k')$ gives the rate of generating an electron at the state (x, k) and a hole at the state (x, k'). Further, $r(x, k, k')$ gives the rate of recombination of an electron at the state (x, k) and a hole at the state (x, k'). The terms in the equation (3.30) are accounted for as follows. The quantity $I_n(F_n, F_p)$ gives the rate of electrons gained or lost in the state (x, k) due to generation and recombination processes. The first term under the integral, $g(x, k, k')(1 - F_n)(1 - F_p')$, is the gain term due to electrons being generated in the state (x, k) in combinatin with a hole being generated in any state (x, k'). A necessary requirement for this process is the fact that the state (x, k) must not be populated by an electron and the state (x, k') not by a hole. Hence, the factors $(1 - F_n)(1 - F_p')$ occur.

The second term under the integral, $-r(x, k, k')F_n F_p'$, is a loss term, easily recognised as such by the minus sign. It describes the reduction of the number of electrons in the state (x, k) by recombination of electron-hole pairs. Naturally, the electron state (x, k) and the hole state (x, k') have to be occupied for a recombination process to occur.

The term $I_n(F_n, F_p)$ only accounts for electrons with wave vector k. The wave vector k' of the according hole is not specified. Generation and recombination can occur involving a hole with any wave vector k'. To account for all possible pairings the integral $\int_B \cdots dk'$ over the Brillouin zone has to be taken. The argumentation is analogous for the hole equation (3.31).

Corresponding to the properties of the collision operators Q_n and Q_p, we have to ensure that generation into and recombination from the state (x, k), represented by the operators I_n, (3.30) and I_p, (3.31), balance in thermal equilibrium. A sufficient condition is given by the relation

$$\begin{aligned} g(x, k, k')(1 - F_{ne})(1 - F_{pe}') &= r(x, k, k')F_{ne}F_{pe}' \\ g(x, k, k')(1 - F_{ne} - F_{pe}' + F_{ne}F_{pe}') &= r(x, k, k')F_{ne}F_{pe}' \,, \end{aligned}$$

where $F_{ne/pe}$ stands for the electron/hole distribution in thermal equilibrium given by the Fermi-Dirac statistics (3.13), (3.14). Bringing $r(x, k, k')$ to the left side of the equation and all the other terms to the right side yields

$$r(x, k, k') = g(x, k, k') \left\{ \frac{1}{F_{ne}F_{pe}'} - \frac{1}{F_{pe}'} - \frac{1}{F_{ne}} + 1 \right\} .$$

Now, we insert the expressions (3.13), (3.14) for the equilibrium distribution functions $F_{ne/pe}$ into this relation:

$$\begin{aligned} r(x, k, k') = g(x, k, k') \Bigg\{ & \left[1 + \exp\left(\frac{\varepsilon_n(k) - \varepsilon_F}{k_B T}\right)\right] \left[1 + \exp\left(\frac{-\varepsilon_p(k') + \varepsilon_F}{k_B T}\right)\right] \\ & - \left[1 + \exp\left(\frac{-\varepsilon_p(k') + \varepsilon_F}{k_B T}\right)\right] - \left[1 + \exp\left(\frac{\varepsilon_n(k) - \varepsilon_F}{k_B T}\right)\right] + 1 \Bigg\} \end{aligned}$$

Sorting the terms results in

$$\begin{aligned} r(x,k,k') = g(x,k,k')\Bigg\{ & 1 + \exp\left(\frac{\varepsilon_n(k)-\varepsilon_F}{k_B T}\right) + \exp\left(\frac{-\varepsilon_p(k')+\varepsilon_F}{k_B T}\right) \\ & + \exp\left(\frac{\varepsilon_n(k)-\varepsilon_p(k')}{k_B T}\right) - 1 - \exp\left(\frac{-\varepsilon_p(k')+\varepsilon_F}{k_B T}\right) \\ & -1 - \exp\left(\frac{\varepsilon_n(k)-\varepsilon_F}{k_B T}\right) + 1 \Bigg\}, \end{aligned}$$

from which we finally obtain the detailed balance relation

$$r(x,k,k') = g(x,k,k')\exp\left(\frac{\varepsilon_n(k)-\varepsilon_p(k')}{k_B T}\right) \tag{3.32}$$

connecting the generation rate $g(x,k,k')$ and the recombination rate $r(x,k,k')$.

The space charge density ρ is constituted by electrons, holes and also ionized impurities, called dopants. The impurity or doping profile will be called C, and we assume it to be only dependent on the position vector x: $C = C(x)$. By this assumption we exclude mobile impurities. The doping profile C is given by the number of positively charged donors minus the number of negatively charged acceptors. Adding up all contributions to the space charge density leaves

$$\rho = -q(n-p-C)\,. \tag{3.33}$$

By integrating the Boltzmann equations (3.28) and (3.29) over the Brillouin zone B, a calculation that will be done explicitely in the next section, one obtains

$$q\partial_t n - \operatorname{div} J_n = -qR\,, \tag{3.34}$$

$$q\partial_t p + \operatorname{div} J_p = -qR\,, \tag{3.35}$$

where R accounts for the generation and recombination of charges. It is expressed in terms of the distribution functions F_n and F_p:

$$R = -\int_B I_p(F_n,F_p)dk = -\int_B I_n(F_n,F_p)dk\,.$$

It has to be noted that the conservation laws (3.34), (3.35) are coupled in a nonlinear way via R, meaning recombinatin and generation processes. This means that the total number of each type of charge is no longer conserved, although electrons and holes can only be generated or destroyed in pairs.

The total current density

$$J = J_n + J_p\,, \tag{3.36}$$

satisfies a continuity equation. This can be verified by a short calculation. Substracting (3.34) from (3.35) and using (3.33) and (3.36) gives:

$$\begin{aligned}
q\partial_t p - q\partial_t n + \operatorname{div} J_p + \operatorname{div} J_n &= 0 \\
q\partial_t (p-n) + \operatorname{div}(J_p + J_n) &= 0 \\
-q\partial_t (n-p) + \operatorname{div} J &= 0 \\
\partial_t(-q(n-p)) + \operatorname{div} J &= 0 \\
\partial_t(-q(n-p-C)) - \partial_t C + \operatorname{div} J &= 0 \\
\partial_t \rho - \underbrace{\partial_t C}_{=0} + \operatorname{div} J &= 0 \\
\partial_t \rho + \operatorname{div} J &= 0 \qquad (3.37)
\end{aligned}$$

The conservation of charge for the whole space is obtained by integrating (3.37) over the considered volume V:

$$\int\limits_V \partial_t \rho(x,t) dx + \int\limits_V \operatorname{div} J(x,t)\, dx = 0\,,$$

where we can make use of the Gauß theorem, to transform the integral over the volume V into an integral over the surface of V denoted by ∂V:

$$\partial_t \int\limits_V \rho(x,t) dx + \int\limits_{\partial V} J(x,t)\, dS\,.$$

Here, dS is an infinitesimal surface element of ∂V. Under the assumption that there is no current flow at the surface ∂V, the second integral vanishes, leaving

$$\partial_t \int\limits_V \rho(x,t) dx = 0\,.$$

The partial derivative of the integral over the charge density equals zero, implying that the integral over the charge density has the same value at all times:

$$\int\limits_V \rho(x,t) dx = \int\limits_V \rho(x,t=0) dx\,, \qquad \forall t > 0\,.$$

This means that the total charge in the volume V is conserved.

Again we make use of the low density approximation

$$0 \leqslant F_n \ll 1\,, \qquad 0 \leqslant F_p \ll 1\,, \qquad (3.38)$$

which allows us to set all terms in the collision and generation-recombination integrals that are quadratic in F_n, F_p equal to zero.

Following the example of the collision relaxation time, we can define relaxation times for the charge generation (τ_G) and recombinatin (τ_R) processes:

$$\tau_G(x,k) = \left(\int_B g(x,k,k')dk' \right)^{-1} , \tag{3.39}$$

$$\tau_R(x,k) = \left(\int_B r(x,k,k')dk' \right)^{-1} . \tag{3.40}$$

Comparing the order of magnitude of the different relaxation times one finds that the generation and recombination relaxation times are far larger than the collision relaxation times. This complies with the natural assumption that collisions happen more frequently than generations or recombinations of electron-hole pairs. The collision relaxation time is of the order of $\sim 10^{-12}\,\mathrm{s}$, whereas the generation-recombination relaxation times are of the order of $\sim 10^{-9}\,\mathrm{s}$.

3.2 From kinetic to fluid dynamic models by ways of the mean free path method - the Hilbert expansion

Solving a kinetic transport model numerically is a very difficult undertaking. We make the transition to fluid dynamical models for semiconductors. They have the great advantage of being much more computationally efficient, that means, solving them numerically on a computer takes a lot less time, than solving the basic kinetic models. On the other hand, they are still sufficiently accurate for our purposes from a physical point of view. Not so much information is lost in the transition from a kinetic to a fluid dynamical description of the system at the micrometer scale. There are a number of models around. Their general common feature, however, is the reduced number of independent variables. From a kinetic transport model with seven independent variables (three space, three velocity, one time coordinate) we go over to the fluid dynamic model with just four independent variables (three space, one time coordinate). The dependent variables are usually described by averages of the phase space number density with respect to the velocity, which are called moments.

Two different ways to make the transition to fluid dynamic models exist. The first one, which will also be considered in this thesis exploits the smallness of the mean free path, which is an order parameter of the given system and describes the average distance travelled by an electron between two consecutive scattering events. The second one is a so-called moment method. To close the resulting system of equations it is necessary to make an assumption concerning the velocity dependence of the phase space density. This ansatz also contains several time and position dependent parameters. The ansatz is then inserted into the Boltzmann equation. The resulting equation is multiplied with a number of independent functions of the velocity and then integrated over the velocity space. The result of this procedure is a number of differential equations for the time- and position-dependent parameters of the ansatz. As is easily imagined, the moment method requires a certain amount of experience for choosing an appropriate ansatz. Furthermore, not all occurring integrals can be solved. In such a case the term in question has to be replaced by a suitable phenomenological model.

Considering all steps of the calculation, the first method via the mean free path is easier and will be taken in this thesis. We start with the bipolar model stated in Section 3.1.2,

$$\partial_t F_n + v_n(k) \cdot \nabla_x F_n - \frac{q}{\hbar} E \cdot \nabla_k F_n = Q_n(F_n) + I_n(F_n, F_p)\,, \tag{3.41}$$

$$\partial_t F_p + v_p(k) \cdot \nabla_x F_p + \frac{q}{\hbar} E \cdot \nabla_k F_p = Q_p(F_p) + I_n(F_n, F_p)\,, \tag{3.42}$$

along with the low density approximations (3.16), (3.17) for the collision terms. We use the expression (3.25) for the collision terms, which leads to the following relations for the electron and hole collision terms

$$Q_n(F_n) = \int\limits_B \Phi_n(x,k,k') \left[\exp\left(\frac{\varepsilon_n(k')}{k_B T}\right) F_n' - \exp\left(\frac{\varepsilon_n(k)}{k_B T}\right) F_n\right] dk'\,, \tag{3.43}$$

$$Q_p(F_p) = \int\limits_B \Phi_p(x,k,k') \left[\exp\left(-\frac{\varepsilon_p(k')}{k_B T}\right) F_p' - \exp\left(-\frac{\varepsilon_p(k)}{k_B T}\right) F_p\right] dk'\,. \tag{3.44}$$

For the generation-recombination rates we use the equations (3.30) and (3.31), where we also make use of the low density approximation $(1 - F_{n/p}) \approx 1$ and the relation of detailed balance (3.32):

$$\begin{aligned} I_n(F_n, F_p) &= \int\limits_B [g(x,k,k')(1-F_n)(1-F_p') - r(x,k,k')F_n F_p'] dk' \\ &= \int\limits_B [g(x,k,k') - r(x,k,k') F_n F_p'] dk' \\ &= \int\limits_B \left[g(x,k,k') - g(x,k,k') \exp\left(\frac{\varepsilon_n(k) - \varepsilon_p(k')}{k_B T}\right) F_n F_p'\right] dk' \\ &= -\int\limits_B g(x,k,k') \left[\exp\left(\frac{\varepsilon_n(k) - \varepsilon_p(k')}{k_B T}\right) F_n F_p' - 1\right] dk' \end{aligned} \tag{3.45}$$

The calculation for holes is analogous and will be skipped here. The resulting expression is given by

$$I_p(F_n, F_p) = -\int\limits_B g(x,k',k) \left[\exp\left(\frac{\varepsilon_n(k') - \varepsilon_p(k)}{k_B T}\right) F_n' F_p - 1\right] dk'\,. \tag{3.46}$$

We assume that the conduction electrons gather around the conduction band minimum and the holes around the valence band maximum. This is the case at room temperature. Based on this assumption we make the approximation of a parabolic relation between the energy and wave vector of the electrons and holes:

$$\varepsilon_n(k) = E_c + \frac{\hbar^2}{2m_n}|k|^2\,, \tag{3.47}$$

$$\varepsilon_p(k) = E_v - \frac{\hbar^2}{2m_p}|k|^2\,, \tag{3.48}$$

with E_c, the conduction band minimum, E_v, the valence band maximum and m_n and m_p the effective electron and hole masses. Based on these relations, we calculate the electron and hole velocities according to Eq. (3.26) and (3.27)

$$v_n(k) = \frac{1}{\hbar}\nabla_k \varepsilon_n(k) = \frac{1}{\hbar}\nabla_k\left(E_c + \frac{\hbar^2}{2m_n}|k|^2\right) = \frac{1}{\hbar}\frac{2\hbar^2}{2m_n}k = \frac{\hbar}{m_n}k\,, \tag{3.49}$$

$$v_p(k) = -\frac{1}{\hbar}\nabla_k \varepsilon_p(k) = -\frac{1}{\hbar}\nabla_k\left(E_v - \frac{\hbar^2}{2m_p}|k|^2\right) = \frac{1}{\hbar}\frac{2\hbar^2}{2m_p}k = \frac{\hbar}{m_p}k\,. \tag{3.50}$$

We now introduce the reference velocity

$$\overline{v} = \sqrt{\frac{k_B T}{m_n}}\,. \tag{3.51}$$

The choice of this reference velocity is quite plausible if one considers the terms for the kinetic and thermal energy of an electron:

$$\begin{aligned} E_{kin} &= \frac{m_n v^2}{2}\,,\\ E_{therm} &= \frac{k_B T}{2}\,. \end{aligned}$$

Setting them equal gives the result

$$\begin{aligned} E_{kin} &= E_{therm}\,,\\ \frac{m_n v^2}{2} &= \frac{k_B T}{2}\,,\\ v &= \sqrt{\frac{k_B T}{m_n}}\,. \end{aligned}$$

Consequently, the reference velocity can be seen as the thermal velocity of an electron. We define the scaled wave vector

$$k_s = \frac{\hbar}{m_n \overline{v}}k\,, \tag{3.52}$$

where $\overline{v}$ is the reference velocity (3.51). We want to measure the velocity of electrons in units of this reference velocity:

$$v_{ns} = \frac{v_n}{\overline{v}} = \frac{\hbar k}{m_n}\frac{1}{\overline{v}} = k_s\,, \tag{3.53}$$

where we made use of the relation $p_n = m_n v_n = \hbar k$ to express v_n. This result immediately justifies the definition of k_s, (3.52). The scaled hole velocity is defined analogously:

$$v_{ps} = \frac{v_p}{\overline{v}} = \frac{\hbar k}{m_p}\frac{1}{\overline{v}} = \frac{m_n}{m_p}k_s\,. \tag{3.54}$$

The collision and generation-recombination relaxation times defined in (3.39), (3.40) are associated with the corresponding mean free paths, l_C and l_R, between two consecutive scattering or recombination-generation events

$$\tau_C = \frac{l_C}{\overline{v}}, \qquad \tau_R = \frac{l_R}{\overline{v}}\,,$$

Collisions happen much more frequently than generations or recombinations, [20], therefore $\tau_R \approx 10^{-9}\,\mathrm{s} \ll \tau_C \approx 10^{-12}\,\mathrm{s}$. Thus,

$$l_C \ll l_R \tag{3.55}$$

holds. The ratio of the two mean free paths, denoted by the parameter α^2 is very small

$$\alpha^2 = \frac{l_C}{l_R} \ll 1\,.$$

The smallness of the parameter α will be exploited later. The next steps taken are a rescaling of the Boltzmann equations (3.41) and (3.42) by making a variable transformation to the scaled quantities defined above. This way we introduce the parameter α to the equation. We then will perform an expansion in terms of powers of α.

To complete the scaling we also need to convert the position x, time t, the according derivatives and the electric field strength into dimensionless variables. This is done by defining the reference length l_0 by

$$\alpha = \frac{l_C}{l_0}\,,$$

which means that α can be interpreted as the scaled mean free path between two scattering events. In addition, we need the reference time τ_R and the thermal voltage

$U_T = \frac{k_B T}{q}$ for the scaling procedure:

$$\begin{aligned}
x_s &= \frac{x}{l_0}\,, \\
t_s &= \frac{t}{\tau_R} = \frac{t\overline{v}}{l_R} = \frac{t\overline{v}\alpha^2}{lc} = t\alpha\frac{\overline{v}}{l_0}\,, \\
E_s &= E\frac{l_0}{U_T}\,.
\end{aligned}$$

We perform the rescaling explicitely for the electron Boltzmann equation (3.41), where me make the following substitutions:

$$\begin{aligned}
\nabla_k &= \frac{\hbar}{m_n\overline{v}}\nabla_{k_s}\,, \\
\nabla_x &= \frac{1}{l_0}\nabla_{x_s}\,, \\
\partial_t &= \alpha\frac{\overline{v}}{l_0}\partial_{t_s}\,, \\
v_n &= \overline{v}v_{ns}\,, \\
E &= E_s\frac{U_T}{l_0}\,.
\end{aligned}$$

To tackle the right side of the Boltzmann equation, we use the fact that the scaled collision and recombination-generation terms Q_{ns} and I_{ns} are linked to the unscaled terms by the respective relaxation times τ_C and τ_R:

$$\begin{aligned}
Q_{ns} &= \frac{Q_n}{\frac{1}{\tau_C}}\,, \\
I_{ns} &= \frac{I_n}{\frac{1}{\tau_R}}\,.
\end{aligned}$$

Inserting the definitions stated above into equation (3.41) yields

$$\begin{aligned}
\alpha\frac{\overline{v}}{l_0}\partial_{t_s}F_{ns} + \overline{v}v_{ns}\frac{1}{l_0}\cdot\nabla_{x_s}F_{ns} - \frac{q}{\hbar}E_s\frac{U_T}{l_0}\frac{\hbar}{m_n\overline{v}}\cdot\nabla_{k_s}F_{ns} &= \frac{1}{\tau_C}Q_{ns} + \frac{1}{\tau_R}I_{ns} \\
&= \frac{\overline{v}}{l_C}Q_{ns} + \frac{\overline{v}}{l_R}I_{ns}
\end{aligned}$$

$$\alpha\frac{\overline{v}}{l_0}\frac{l_C}{\overline{v}}\partial_{t_s}F_{ns} + \overline{v}v_{ns}\frac{1}{l_0}\frac{l_C}{\overline{v}}\cdot\nabla_{x_s}F_{ns} - \frac{q}{\hbar}E_s\frac{U_T}{l_0}\frac{\hbar}{m_n\overline{v}}\frac{l_C}{\overline{v}}\cdot\nabla_{k_s}F_{ns} = Q_{ns} + \frac{l_C}{l_R}I_{ns}$$

In the next steps we use the relations $l_C = \alpha l_0$, $\overline{v}^2 = \frac{k_B T}{m_n}$ and $U_T = \frac{k_B T}{q}$:

$$\alpha^2 \partial_{t_s} F_{ns} + \alpha v_{ns} \cdot \nabla_{x_s} F_{ns} - \alpha \frac{q E_s U_T m_n}{k_B T m_n} \cdot \nabla_{k_s} F_{ns} = Q_{ns} + \alpha^2 I_{ns}$$
$$\alpha^2 \partial_{t_s} F_{ns} + \alpha v_{ns} \cdot \nabla_{x_s} F_{ns} - \alpha E_s \cdot \nabla_{k_s} F_{ns} = Q_{ns} + \alpha^2 I_{ns} \, .$$

From here on we will omit the index s for the scaled quantities. The rescaled versions of the Boltzmann equation for electrons and holes are

$$\alpha^2 \partial_t F_n + \alpha \{ v_n(k) \cdot \nabla_x F_n - E \cdot \nabla_k F_n \} = Q_n(F_n) + \alpha^2 I_n(F_n, F_p) \, , \tag{3.56}$$
$$\alpha^2 \partial_t F_p + \alpha \{ v_p(k) \cdot \nabla_x F_p + E \cdot \nabla_k F_p \} = Q_p(F_p) + \alpha^2 I_n(F_n, F_p) \, . \tag{3.57}$$

The scaled collision ($Q_{n/p}(F_{n/p})$) and generation-recombination ($I_{n/p}(F_n, F_p)$) terms have the same form as the unscaled ones, except that the integration is taken over $\mathbb{R}^3$ instead of the Brillouin zone B. This is allowed, because the charge distribution function $F_{n/p}$ is approximately zero everywhere outside the Brillouin zone B. Apart from the change in integration limits the exponential factors

$$\exp\left(\frac{\varepsilon_n(k)}{k_B T} \right) \, , \qquad \exp\left(\frac{\varepsilon_p(k)}{k_B T} \right) \, , \tag{3.58}$$

change into

$$\exp\left(E_{cs} + \frac{1}{2} |k_s|^2 \right) \, , \qquad \exp\left(E_{vs} - \frac{m_n}{2 m_p} |k_s|^2 \right) \, , \tag{3.59}$$

due to the equations (3.47) and (3.48), where the energy $E_{cs} = \frac{E_c}{k_B T}$ is the scaled conduction band minimum and $E_{vs} = \frac{E_v}{k_B T}$ the scaled valence band maximum. We find these changes for the exponential factors by the following basic calculation steps for electrons

$$\begin{aligned} \frac{\varepsilon_n(k)}{k_B T} &= \frac{E_c + \frac{\hbar^2}{2 m_n} |k|^2}{k_B T} = \frac{E_c + \frac{\hbar^2}{2 m_n} \frac{m_n^2 \overline{v}^2}{\hbar^2} |k_s|^2}{k_B T} \\ &= \frac{E_c + \frac{m_n \overline{v}^2}{2} |k_s|^2}{k_B T} = \frac{E_c + \frac{m_n k_B T}{2 m_n} |k_s|^2}{k_B T} = E_{cs} + \frac{1}{2} |k_s|^2 \, , \end{aligned}$$

and analogously for holes

$$\begin{aligned} \frac{\varepsilon_p(k)}{k_B T} &= \frac{E_v - \frac{\hbar^2}{2 m_p} |k|^2}{k_B T} = \frac{E_v - \frac{\hbar^2}{2 m_p} \frac{m_n^2 \overline{v}^2}{\hbar^2} |k_s|^2}{k_B T} \\ &= \frac{E_v - \frac{m_n^2}{2 m_p} \overline{v}^2 |k_s|^2}{k_B T} = \frac{E_v - \frac{m_n^2}{2 m_p} \frac{k_B T}{m_n} |k_s|^2}{k_B T} = E_{vs} - \frac{m_n}{2 m_p} |k_s|^2 \, . \end{aligned}$$

At this point we apply a Hilbert expansion. This is an expansion of the distribution functions of the scaled Boltzmann equations (3.56), (3.57) in terms of powers of the scaled mean free path $\alpha = \frac{l_C}{l_0}$:

$$F_n = F_{n0} + \alpha F_{n1} + \alpha^2 F_{n2} + \cdots \tag{3.60}$$

$$F_p = F_{p0} + \alpha F_{p1} + \alpha^2 F_{p2} + \cdots \tag{3.61}$$

We insert the Hilbert expansions (3.60), (3.61) into the scaled Boltzmann equations (3.56), (3.57) and sort the terms in powers of α. The result for the electron equation reads

$$\begin{aligned} &\sum_{j=2}^{\infty} \alpha^j \frac{\partial}{\partial t} F_{n,j-2} + \sum_{j=1}^{\infty} \alpha^j \left(v_n \cdot \nabla_x F_{n,j-1} - E \cdot \nabla_k F_{n,j-1} \right) \\ &\quad = \sum_{j=0}^{\infty} Q_n(F_{n,j}) + \sum_{j=2}^{\infty} \alpha^j I_n(F_{n,j-2}, F_{p,j-2}) \,. \end{aligned}$$

The equation for holes looks analogously. The coefficients of the terms α^0, α^1, $\alpha^2, \ldots$ have to vanish, since the powers of α are linearly independent. The only term of the order of $\alpha^0 = 1$ is $Q_{n/p}(F_{n0/p0})$, so it immediately follows that

$$Q_n(F_{n0}) = Q_p(F_{p0}) = 0 \,. \tag{3.62}$$

Equation (3.62) has the solutions

$$F_{n0} = n(x,t) M_n(k), \qquad F_{p0} = p(x,t) M_p(k), \tag{3.63}$$

with M_n and M_p denoting the scaled Maxwell distributions

$$M_n(k) = \frac{1}{N_c} \exp\left(-\frac{1}{2} |k|^2 \right) , \tag{3.64}$$

$$M_p(k) = \frac{1}{N_v} \exp\left(-\frac{m_n}{2 m_p} |k|^2 \right) , \tag{3.65}$$

with the constants

$$N_c = (2\pi)^{\frac{3}{2}}, \qquad N_v = \left(\frac{2\pi m_p}{m_n} \right)^{\frac{3}{2}} . \tag{3.66}$$

N_c and N_v are chosen in a way that ensures that the integrals of the Maxwell distributions taken over the entire k-space are equal to one, meaning the Maxwell distributions (3.64), (3.65) are normalized. With this normalization we can identify the until now unspecified quantities $n(x,t)$, $p(x,t)$ as the scaled position space number densities of electrons and holes. We now verify that (3.63) are solutions to

(3.62):

$$\begin{aligned}
Q_n(F_{n0}) &= \int\limits_{\mathbb{R}^3} \Phi_n \left[\exp\left(E_c + \frac{1}{2}|k'|^2\right) F'_{n0} - \exp\left(E_c + \frac{1}{2}|k|^2\right) F_{n0}\right] dk' \\
&= \int\limits_{\mathbb{R}^3} \Phi_n \Bigg[\exp\left(E_c + \frac{1}{2}|k'|^2\right) n(x,t)\frac{1}{N_c}\exp\left(-\frac{1}{2}|k'|^2\right) \\
&\qquad - \exp\left(E_c + \frac{1}{2}|k|^2\right) n(x,t)\frac{1}{N_c}\exp\left(-\frac{1}{2}|k|^2\right) \Bigg] dk' \\
&= \int\limits_{\mathbb{R}^3} \Phi_n \underbrace{\left[\exp\left(E_c\right) n(x,t)\frac{1}{N_c} - \exp\left(E_c\right) n(x,t)\frac{1}{N_c}\right]}_{=0} dk' = 0
\end{aligned}$$

$$\begin{aligned}
Q_p(F_{p0}) &= \int\limits_{\mathbb{R}^3} \Phi_p \left[\exp\left(-E_v + \frac{m_n}{2m_p}|k'|^2\right) F'_{p0} - \exp\left(-E_v + \frac{m_n}{2m_p}|k|^2\right) F_{p0}\right] dk' \\
&= \int\limits_{\mathbb{R}^3} \Phi_p \Bigg[\exp\left(-E_v + \frac{m_n}{2m_p}|k'|^2\right) p(x,t)\frac{1}{N_v}\exp\left(-\frac{m_n}{2m_p}|k'|^2\right) \qquad (3.67) \\
&\qquad - \exp\left(-E_v + \frac{m_n}{2m_p}|k|^2\right) p(x,t)\frac{1}{N_v}\exp\left(-\frac{m_n}{2m_p}|k|^2\right) \Bigg] dk' \\
&= \int\limits_{\mathbb{R}^3} \Phi_n \underbrace{\left[\exp\left(-E_v\right) p(x,t)\frac{1}{N_v} - \exp\left(-E_v\right) p(x,t)\frac{1}{N_v}\right]}_{=0} dk' = 0
\end{aligned}$$

Collecting terms of the oder $\alpha^1 = \alpha$ and setting the whole coefficient equal to zero leads to

$$v_n(k)\cdot\nabla_x F_{n0} - E\cdot\nabla_k F_{n0} = Q_n(F_{n1})\,,$$

where we insert (3.63) for F_{n0}

$$v_n(k)\cdot\nabla_x(n(x,t)M_n(k)) - E\cdot\nabla_k(n(x,t)M_n(k)) = Q_n(F_{n1})\,.$$

Because $M_n(k)$ is no function of x and $n(x,t)$ is no function of k we are allowed to write

$$v_n(k)M_n(k)\cdot\nabla_x n(x,t) - E\,n(x,t)\cdot\nabla_k M_n(k) = Q_n(F_{n1})\,.$$

Here we need the expression for $\nabla_k M_n(k)$,

$$\begin{aligned}
\nabla_k M_n(k) &= \frac{1}{N_c}\nabla_k \exp\left(-\frac{1}{2}|k|^2\right) = -\frac{1}{N_c}\exp\left(-\frac{1}{2}|k|^2\right) k \\
&= -M_n k = -M_n v_n,
\end{aligned}$$

where we used $v_{ns} = k_s$ of (3.53), here omitting the index s. With this we get

$$v_n(k)M_n(k) \cdot [\nabla_x n(x,t) + E\, n(x,t)] = Q_n(F_{n1})\,,$$

as equation for the coefficients of α for electrons.
The calculation for holes is analogous, nevertheless it will be given here explicitely:

$$\begin{aligned}
&v_p(k) \cdot \nabla_x F_{p0} + E \cdot \nabla_k F_{p0} = Q_p(F_{p1})\\
&v_p(k) \cdot \nabla_x (p(x,t)M_p(k)) + E \cdot \nabla_k (p(x,t)M_p(k)) = Q_p(F_{p1})\\
&v_p(k)M_p(k) \cdot \nabla_x p(x,t) + E\, p(x,t) \cdot \nabla_k M_p(k) = Q_p(F_{p1})
\end{aligned}$$

Calculating $\nabla_k M_p(k)$ gives

$$\begin{aligned}
\nabla_k M_p(k) &= \frac{1}{N_v} \nabla_k \exp\left(-\frac{m_n}{2m_p}|k|^2\right) && (3.68)\\
&= \frac{1}{N_v} \nabla_k \exp\left(-\frac{m_n}{2m_p}(k_x^2 + k_y^2 + k_z^2)\right) && (3.69)\\
&= \frac{1}{N_v} \exp\left(-\frac{m_n}{2m_p}|k|^2\right)\left(-\frac{m_n}{m_p}k\right) && (3.70)\\
&= -M_p(k)v_p\,,
\end{aligned}$$

where we used $v_{ps} = \frac{m_n}{m_p}k_s$ of (3.54), here omitting the index s, leaving finally

$$v_p(k)M_p(k)\,[\nabla_x p(x,t) - E\, p(x,t)] = Q_p(F_{p1})\,. \tag{3.71}$$

For the further steps of the derivation we take advantage of the following lemma, quoting [17] and [20]:
“ *A) A necessary and sufficient condition for the solvability of an equation of the form*

$$Q_{n/p}(f) = g \tag{3.72}$$

is

$$\int\limits_{\mathbb{R}^3} g\, dk = 0\,. \tag{3.73}$$

If (3.73) holds, (3.72) has a one-dimensional linear manifold of solutions of the form $f = f_{n/p} + q_{n/p}M_{n/p}$ *where* $f_{n/p}$ *denotes a particular solution and* $q_{n/p}$ *is a parameter.*
B) The equations

$$Q_n(h_n) = M_n v_n\,, \qquad Q_p(h_p) = M_p v_p \tag{3.74}$$

have solutions $h_n(x,k),\ h_p(x,k) \in \mathbb{R}^3$ *which satisfy*

$$\int_{\mathbb{R}^3} v_n \otimes h_n \, dk = -\mu_n(x) I_3 < 0, \tag{3.75}$$

$$\int_{\mathbb{R}^3} v_p \otimes h_p \, dk = -\mu_p(x) I_3 < 0, \tag{3.76}$$

where I_3 *is the three-dimensional unity matrix and* $a \otimes b = ab^T$*, for* $a, b \in \mathbb{R}^3$*, denotes the tensor product. Furthermore, the j-th component of* $h_{n/p}$ *is an odd function of the j-th component of* k *and has the form*

$$h_{n/p,j}(k) = \overline{h}(k_j, |P_j k|)\,,$$

where $|P_j k|$ *denotes the Euclidian norm of the projection of* k *onto the plane perpendicular to the* k_j*-direction.*"
Here we introduce the scaled current densities

$$J_n(x,t) = \mu_n(\nabla_x n + nE)\,, \tag{3.77}$$

$$J_p(x,t) = -\mu_p(\nabla_x p - pE)\,, \tag{3.78}$$

with the mobilities μ_n for electrons and μ_p for holes. The first term denotes current caused by diffusion due to a gradient in the electron distribution. If electrons are accumulated at one place they will diffuse away from that area into regions which are less densely populated. The second term describes drifting electrons. Drift is caused by an applied external or internal electric field. Both terms are proportional to the mobility. The larger the mobility, the more current is gained from the same acting forces. The argumentation is analogous for holes, yet the signs in the formulas are reversed for the hole case. The overal minus sign takes care of the fact that holes moving in one direction give the same current as electrons moving in the opposite direction because of their opposite charge. The minus in front of the drift term is caused by the fact that holes in an electric field are drawn in the opposite direction as electrons exposed to the same electric field.
Using the expressions for the scaled current densities (3.77), (3.78) and the above stated Lemma the solutions to (3.68), (3.71) are

$$F_{n1} = J_n \cdot \frac{h_n}{\mu_n} - q_n M_n\,, \tag{3.79}$$

$$F_{p1} = -J_p \cdot \frac{h_p}{\mu_p} + q_p M_p\,, \tag{3.80}$$

where q_n and q_p are as yet unspecified.
Going further and collecting coefficients of order $\alpha^n,\ n \geqslant 2\,$, in the scaled versions

of the Boltzmann equation (3.56), (3.57) results in:

$$\partial_t F_{n,j-2} + v_n \cdot \nabla_x F_{n,j-1} - E \cdot \nabla_k F_{n,j-1} = Q_n(F_{n,j}) + I_n(F_{n,j-2}, F_{p,j-2})\,, \tag{3.81}$$
$$\partial_t F_{p,j-2} + v_p \cdot \nabla_x F_{p,j-1} + E \cdot \nabla_k F_{p,j-1} = Q_p(F_{p,j}) + I_n(F_{n,j-2}, F_{p,j-2})\,. \tag{3.82}$$

Looking at (3.56), (3.57), the form of (3.81), (3.82) is immediately obvious. The partial derivative appears as a coefficient to α^2, hence the subscript $j-2$, the same applies to the term I_n. The coefficients to α appear here with the index $j-1$. The argument of Q_n has index j, because in the Boltzmann equation this term is a coefficient to $\alpha^0 = 1$.

We now consider the special case $j = 2$. Equations (3.81), (3.82) turn into

$$\partial_t F_{n0} + v_n \cdot \nabla_x F_{n1} - E \cdot \nabla_k F_{n1} = Q_n(F_{n2}) + I_n(F_{n0}, F_{p0})\,, \tag{3.83}$$
$$\partial_t F_{p0} + v_p \cdot \nabla_x F_{p1} + E \cdot \nabla_k F_{p1} = Q_p(F_{p2}) + I_n(F_{n0}, F_{p0})\,. \tag{3.84}$$

We can now make use of the solvability condition (3.72), (3.73). Applying it to (3.83) we get

$$\int\limits_{\mathbb{R}^3} \left[\underbrace{\partial_t F_{n0}}_{(1)} + \underbrace{v_n \cdot \nabla_x F_{n1}}_{(2)} - \underbrace{E \cdot \nabla_k F_{n1}}_{(3)} - \underbrace{I_n(F_{n0}, F_{p0})}_{(4)} \right] dk \overset{!}{=} 0\,. \tag{3.85}$$

We now insert (3.63) for F_{n0}, F_{p0} and (3.79) for F_{n1}, treating the different terms of the integral separately for easier reading. First we calculate (1) by inserting (3.63) for F_{n0}

$$\begin{aligned} \int\limits_{\mathbb{R}^3} \partial_t F_{n0} dk &= \int\limits_{\mathbb{R}^3} \partial_t \left(n(x,t) M_n(k) \right) dk \\ &= \int\limits_{\mathbb{R}^3} M_n(k) \partial_t n(x,t) dk \\ &= \partial_t\, n(x,t) \underbrace{\int\limits_{\mathbb{R}^3} M_n(k)\, dk}_{=1} = \partial_t\, n(x,t)\,. \end{aligned} \tag{3.86}$$

In the second line we used that the Maxwell distribution M_n is not a function of time. We are also allowed to exchange the partial derivative and the integral. Lastly we exploit the fact that the Maxwell distribution we use is normalized in $\mathbb{R}^3$.

Moving on to part (2) of the integral, we replace F_{n1} by (3.79)

$$\begin{aligned}\int\limits_{\mathbb{R}^3} v_n \cdot \nabla_x F_{n1} dk &= \int\limits_{\mathbb{R}^3} v_n(k) \cdot \nabla_x \left(J_n(x,t) \cdot \frac{h_n(x,k)}{\mu_n(x)} - q_n M_n(k) \right) dk \\ &= \int\limits_{\mathbb{R}^3} \left[\nabla_x \cdot \left(v_n(k) \frac{J_n(x,t) \cdot h_n(x,k)}{\mu_n(x)} \right) - v_n(k) \cdot M_n(k) \nabla_x q_n \right] dk\end{aligned}$$

Here we used that the Maxwell distribution and the electron velocity do not depend on the position x. Thus, we are allowed to pull $v_n(k)$ into the argument of the differential operator. The term $\nabla_x \, q_n$ is equal to zero, because q_n is just a parameter as stated in the lemma. The first term can be rewritten as follows

$$\begin{aligned}\nabla_x \cdot \left[v_n(k) \frac{J_n(x,t) \cdot h_n(x,k)}{\mu_n(x)} \right] &= \nabla_x \cdot \left[v_n(k) \frac{h_n(x,k) \cdot J_n(x,t)}{\mu_n(x)} \right] \\ &= \nabla_x \cdot \left[(v_n(k) \otimes h_n(x,k)) \, \frac{J_n(x,t)}{\mu_n(x)} \right] .\end{aligned}$$

The validity of the last transformation will be shown here:

$$\begin{aligned}v_n(k) \left[h_n(x,k) \cdot J_n(x,t) \right] &= \begin{pmatrix} v_1 \\ v_2 \\ v_3 \end{pmatrix} \left[\begin{pmatrix} h_1 \\ h_2 \\ h_3 \end{pmatrix} \cdot \begin{pmatrix} J_1 \\ J_2 \\ J_3 \end{pmatrix} \right] \\ &= \begin{pmatrix} v_1 h_1 J_1 + v_1 h_2 J_2 + v_1 h_3 J_3 \\ v_2 h_1 J_1 + v_2 h_2 J_2 + v_2 h_3 J_3 \\ v_3 h_1 J_1 + v_3 h_2 J_2 + v_3 h_3 J_3 \end{pmatrix}\end{aligned}$$

Evaluating the expression including the tensor product yields

$$\begin{aligned}\left[v_n(k) \otimes h_n(x,k) \right] J_n(x,t) &= \left[v_n h_n^T \right] J_n \\ &= \left[\begin{pmatrix} v_1 \\ v_2 \\ v_3 \end{pmatrix} \cdot (h_1, h_2, h_3) \right] \begin{pmatrix} J_1 \\ J_2 \\ J_3 \end{pmatrix} \\ &= \begin{pmatrix} v_1 h_1 & v_1 h_2 & v_1 h_3 \\ v_2 h_1 & v_2 h_2 & v_2 h_3 \\ v_3 h_1 & v_3 h_2 & v_3 h_3 \end{pmatrix} \begin{pmatrix} J_1 \\ J_2 \\ J_3 \end{pmatrix} \\ &= \begin{pmatrix} v_1 h_1 J_1 + v_1 h_2 J_2 + v_1 h_3 J_3 \\ v_2 h_1 J_1 + v_2 h_2 J_2 + v_2 h_3 J_3 \\ v_3 h_1 J_1 + v_3 h_2 J_2 + v_3 h_3 J_3 \end{pmatrix} .\end{aligned}$$

We see that both expressions yield the same result. This allows us to rewrite part

(2) of the integral as follows

$$\begin{aligned}\int_{\mathbb{R}^3} v_n \cdot \nabla_x F_{n1} dk &= \nabla_x \underbrace{\int_{\mathbb{R}^3} \left(v_n(k) \otimes h_n(x,k)\right) dk}_{=-\mu_n(x) I_3} \frac{J_n(x,t)}{\mu_n(x)} \\ &= -\nabla_x \, I_3 J_n(x,t) \\ &= -\nabla_x \, J_n(x,t)\,, \end{aligned} \tag{3.87}$$

where we used (3.75) of the lemma.

Term (3) of the integral (3.85) equals zero. It can be rewritten as

$$\int_{\mathbb{R}^3} E \cdot \nabla_k F_{n1} dk = E \cdot \oint_{\partial\mathbb{R}^3} F_{n1} dS_k = 0\,, \tag{3.88}$$

where we used Gauß' theorem. The distribution function vanishes for $|k| \to \infty$.

Finally we consider part (4) of the integral. For the generation-recombination term $I_n(F_{n0}, F_{p0})$ we insert the scaled version of equation (3.45), which yields

$$\begin{aligned}\int_{\mathbb{R}^3} I_n(F_{n0}, F_{p0}) dk &= -\int_{\mathbb{R}^3}\int_{\mathbb{R}^3} g(x,k,k') \left[\exp\left(E_c + \frac{1}{2}|k|^2 - E_v + \frac{m_n}{2m_p}|k'|^2 \right) F_{n0} F'_{p0} - 1 \right] dk' dk \\ &= -\int_{\mathbb{R}^3}\int_{\mathbb{R}^3} g(x,k,k') \left[\exp\left(E_c + \frac{1}{2}|k|^2 - E_v + \frac{m_n}{2m_p}|k'|^2 \right) \right. \\ &\times \left. n(x,t)p(x,t) \frac{1}{N_c}\frac{1}{N_v} \exp\left(-\frac{1}{2}|k|^2\right) \exp\left(-\frac{m_n}{2m_p}|k'|^2\right) - 1 \right] dk' dk \\ &= -\int_{\mathbb{R}^3}\int_{\mathbb{R}^3} g(x,k,k') \left[\exp\underbrace{(E_c - E_v)}_{E_g} n(x,t)p(x,t) \frac{1}{N_c}\frac{1}{N_v} - 1 \right] dk' dk \\ &= -n(x,t)p(x,t) \frac{1}{N_c N_v} \exp(E_g) \int_{\mathbb{R}^3}\int_{\mathbb{R}^3} g(x,k,k') dk' dk + \int_{\mathbb{R}^3}\int_{\mathbb{R}^3} g(x,k,k') dk' dk \\ &= -R\,. \end{aligned} \tag{3.89}$$

Here we used the abbreviation $E_g = E_c - E_v$ for the scaled bandgap of the semiconductor. The bandgap is the energy difference between the bottom of the conduction band and the top of the valence band, here impliciteley scaled by the factor $(k_b T)^{-1}$.

Combining (3.86), (3.87), (3.88) and (3.89) we get:

$$\partial_t \, n(x,t) - \nabla_x \, J_n(x,t) = -R\,. \tag{3.90}$$

Doing an analogous calculation for holes results in

$$\partial_t\, p(x,t) + \nabla_x\, J_p(x,t) = -R\,, \tag{3.91}$$

where the recombination-generation rate R is given by

$$R = A(x)(np - n_i^2)\,. \tag{3.92}$$

$A(x)$ and n_i are defined as follows:

$$n_i = \sqrt{N_c N_v}\exp\left(-\frac{E_g}{2}\right)\,, \qquad A(x) = n_i^{-2}\int\limits_{\mathbb{R}^3}\int\limits_{\mathbb{R}^3} g(x,k,k')dk'dk\,.$$

Equations (3.90) and (3.91) together with (3.77), (3.78) are the scaled versions of the drift-diffusion-current equations for semiconductors. The unscaled versions are

$$\begin{aligned} J_n &= q\mu_n\left(U_T\nabla_x\, n + nE\right)\,, & q\partial_t\, n - \nabla_x\, J_n &= -qR\,, \\ J_p &= -q\mu_p\left(U_T\nabla_x\, p + pE\right)\,, & q\partial_t\, p + \nabla_x\, J_p &= -qR\,, \end{aligned} \tag{3.93}$$

with the thermal voltage $U_T = \frac{k_B T}{q}$ introduced earlier in the calculation as the reference voltage. Actually there is a relation between the thermal voltage and carrier mobility. They are connected by the diffusivity D

$$D_n = \mu_n U_T\,, \qquad D_p = \mu_p U_T\,.$$

The equations

$$\frac{D_n}{\mu_n} = \frac{D_p}{\mu_p} = U_T\,, \tag{3.94}$$

are called the Einstein relations. Here the scaled variables are denoted by the same symbols as the unscaled ones. The scaling chosen in this derivation implies $(k_B T m_n)^{\frac{3}{2}}\hbar^{-3}$ as reference value for the number densites of electrons and holes. Considering this, the unscaled recombination-generation rate R is of the form (3.92) with the unscaled intrinsic number density n_i described by

$$n_i = \left(\frac{2\pi k_T\sqrt{m_n m_p}}{\hbar^2}\right)^{\frac{3}{2}}\exp\left(-\frac{E_g}{2k_B T}\right)\,.$$

To be able to simulate processes in semiconductors self-consistently with the electric field the drift diffusion equations (3.93) have to be complemented by the Poisson equation. The resulting equations are called the basic semiconductor device equations. For more detailed information on the derivation of the drift-diffusion-current equations the reader is referred to [17].

4 Numerical methods

4.1 Discretization

To solve the drift-diffusion equations (3.93) on a computer we need to discretize them and solve them at every grid point. The grid spacing is shown schematically in Fig. 4.1.

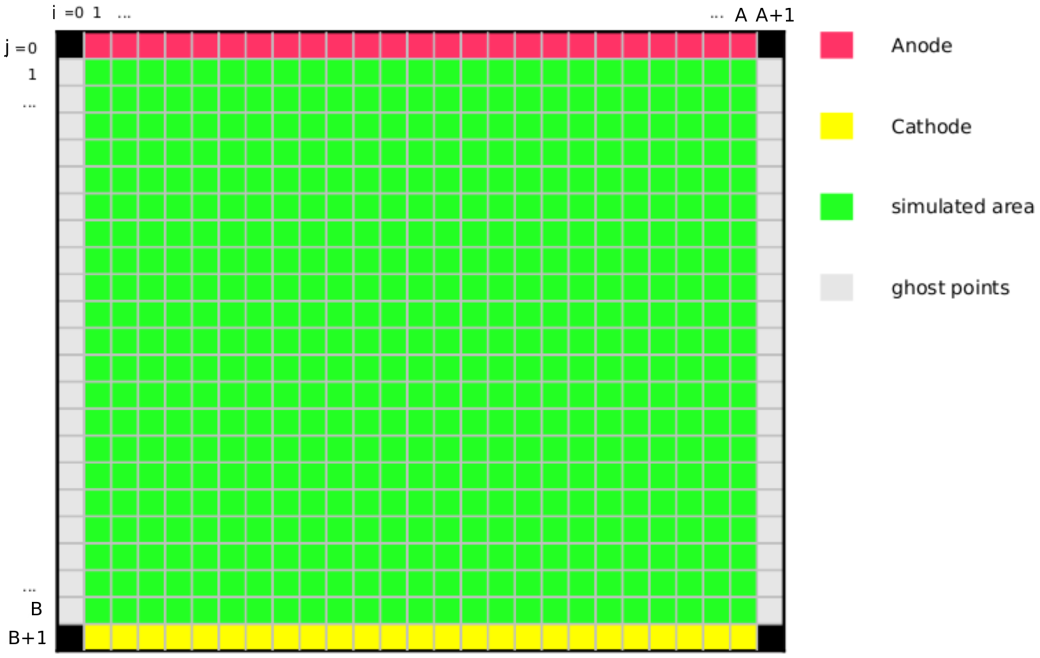

Figure 4.1: Schematic representation of the discretized device. The active layer is coloured green, the top contact is red and the bottom contact yellow. The grey cells on the left and right represent ghost points used to include the proper boundary conditions. In this drawing the y-axis shows downwards and has indices i, the x-axis goes from left to right, with indices j [31].

We choose a rectangular grid with variable grid spacing in both directions. At interfaces the grid spacing is finer than in more homogeneous areas. The index in the y-direction is $j \in [0, B+1]$, where $j = 0$ represents the top contact and $j = B+1$

the bottom contact. In the x-direction the index is $i \in [0, A+1]$, where $i = 0, A+1$ represent the left and right column of ghost points. The lines drawn in Fig. 4.1 represent the cell boundaries. All the necessary quantities like electron and hole density, electrostatic potential are calculated in the center of each cell.

The Poisson as well as the drift-diffusion-current and continuity equations for electrons, holes and excitons need to be discretized and solved on this grid. They form a set of coupled equations. They are solved self-consistently and iteratively until the change between two consecutive iteration steps is smaller than a given tolerance level. To simulate the temporal evolution of the system we use an implicit time step method.

4.2 Poisson solver

We start by discretizing the Poisson equation (2.6)

$$\nabla \cdot [\varepsilon_0 \varepsilon_r(x,y) \nabla \psi(x,y)] = -\rho(x,y) = q\left[n(x,y) - p(x,y)\right],$$

which includes a position dependent relative electric permittivity $\varepsilon_r(x,y)$. In two dimensions it has the form

$$\nabla \cdot f(x,y) = \nabla \cdot \begin{pmatrix} f_x(x,y) \\ f_y(x,y) \end{pmatrix} = \frac{\partial f_x}{\partial x} + \frac{\partial f_y}{\partial y} = -\rho(x,y) = q\left[n(x,y) - p(x,y)\right], \quad (4.1)$$

with

$$f(x,y) = \varepsilon_0 \varepsilon_r(x,y) \nabla \psi(x,y) = \varepsilon_0 \varepsilon_r(x,y) \begin{pmatrix} \frac{\partial \psi}{\partial x} \\ \frac{\partial \psi}{\partial y} \end{pmatrix}. \quad (4.2)$$

For the next step we need a Taylor expansion of f_x on the interval $[x_i - \frac{1}{2}\Delta x_i, x_i + \frac{1}{2}\Delta x_i]$ and of f_y on the interval $[y_j - \frac{1}{2}\Delta y_j, y_j + \frac{1}{2}\Delta y_j]$. From here on we use the abbreviations

$$\begin{aligned} a_i &= \Delta x_i = x_{i+1} - x_i\,, \\ b_j &= \Delta y_j = y_{j+1} - y_j\,. \end{aligned}$$

With these expressions we can write the Taylor expansions as

$$f_x(x_{i+\frac{1}{2}}, y_j) = f_x(x_i, y_j) + \frac{a_i}{2} \left.\frac{\partial f_x(x,y)}{\partial x}\right|_{(x_i,y_j)} + O(x^2)\,, \quad (4.3)$$

$$f_x(x_{i-\frac{1}{2}}, y_j) = f_x(x_i, y_j) - \frac{a_{i-1}}{2} \left.\frac{\partial f_x(x,y)}{\partial x}\right|_{(x_i,y_j)} + O(x^2)\,, \quad (4.4)$$

$$f_y(x_i, y_{j+\frac{1}{2}}) = f_y(x_i, y_j) + \frac{b_j}{2} \left.\frac{\partial f_y(x,y)}{\partial y}\right|_{(x_i,y_j)} + O(x^2)\,, \quad (4.5)$$

$$f_y(x_i, y_{j-\frac{1}{2}}) = f_x(x_i, y_j) - \frac{b_{j-1}}{2} \left.\frac{\partial f_y(x,y)}{\partial y}\right|_{(x_i,y_j)} + O(x^2)\,. \quad (4.6)$$

We now subtract (4.4) from (4.3), only considering terms up to first order, to obtain

$$\begin{aligned}\frac{a_i + a_{i-1}}{2}\,\frac{\partial f_x(x,y)}{\partial x}\bigg|_{(x_i,y_j)} &= f_x(x_{i+\frac{1}{2}},y_j) - f_x(x_{i-\frac{1}{2}},y_j)\,,\\ \frac{\partial f_x(x,y)}{\partial x}\bigg|_{(x_i,y_j)} &= \frac{f_x(x_{i+\frac{1}{2}},y_j) - f_x(x_{i-\frac{1}{2}},y_j)}{\frac{1}{2}(a_i + a_{i-1})}\,.\end{aligned}$$

Substrating (4.6) from (4.5) yields the analogous result for the y-coordinate:

$$\frac{\partial f_y(x,y)}{\partial y}\bigg|_{(x_i,y_j)} = \frac{f_y(x_i,y_{j+\frac{1}{2}}) - f_y(x_i,y_{j-\frac{1}{2}})}{\frac{1}{2}(b_j + b_{j-1})}\,.$$

We can now write down the discretized expression for $\nabla f(x,y)$

$$\nabla f(x,y)|_{(x_i,y_j)} = \frac{f_x(x_{i+\frac{1}{2}},y_j) - f_x(x_{i-\frac{1}{2}},y_j)}{\frac{1}{2}(a_i + a_{i-1})} + \frac{f_y(x_i,y_{j+\frac{1}{2}}) - f_y(x_i,y_{j-\frac{1}{2}})}{\frac{1}{2}(b_j + b_{j-1})}\,.$$

Reinserting (4.2) for $f(x,y)$ yields

$$\begin{aligned}\varepsilon_0\,\nabla\left(\varepsilon_r(x,y)\nabla\psi(x,y)\right)|_{(x_i,y_j)} =\, &\varepsilon_0\frac{\left[\varepsilon_r(x,y)\frac{\partial\psi}{\partial x}\right]_{(x_{i+\frac{1}{2}},y_j)} - \left[\varepsilon_r(x,y)\frac{\partial\psi}{\partial x}\right]_{(x_{i-\frac{1}{2}},y_j)}}{\frac{1}{2}(a_i + a_{i-1})}\\ &+\varepsilon_0\frac{\left[\varepsilon_r(x,y)\frac{\partial\psi}{\partial y}\right]_{(x_i,y_{j+\frac{1}{2}})} - \left[\varepsilon_r(x,y)\frac{\partial\psi}{\partial y}\right]_{(x_i,y_{j-\frac{1}{2}})}}{\frac{1}{2}(b_j + b_{j-1})}\,.\end{aligned} \tag{4.7}$$

To shorten the formulas a bit we use the notation $[f(x,y)]_{(x_i,y_j)} = f_{i,j}$. Also, we still have to discretize the spatial derivatives occurring in equation (4.7). The approximated expressions read

$$\begin{aligned}\frac{\partial\psi}{\partial x}\bigg|_{(x_{i+\frac{1}{2}},y_j)} &\approx \frac{\psi_{i+1,j} - \psi_{i,j}}{a_i}\,, &\quad \frac{\partial\psi}{\partial x}\bigg|_{(x_{i-\frac{1}{2}},y_j)} &\approx \frac{\psi_{i,j} - \psi_{i-1,j}}{a_{i-1}}\\ \frac{\partial\psi}{\partial y}\bigg|_{(x_i,y_{j+\frac{1}{2}})} &\approx \frac{\psi_{i,j+1} - \psi_{i,j}}{b_j}\,, &\quad \frac{\partial\psi}{\partial y}\bigg|_{(x_i,y_{j-\frac{1}{2}})} &\approx \frac{\psi_{i,j} - \psi_{i,j-1}}{b_{j-1}}\,.\end{aligned} \tag{4.8}$$

We use the discretized derivatives (4.8) and obtain for equation (4.7)

$$\varepsilon_0 \nabla \cdot (\varepsilon_r(x,y)\nabla\psi(x,y))|_{(x_i,y_j)} = \varepsilon_0 \frac{\varepsilon_{r,i+\frac{1}{2},j}\left(\frac{\psi_{i+1,j}-\psi_{i,j}}{a_i}\right) - \varepsilon_{r,i-\frac{1}{2},j}\left(\frac{\psi_{i,j}-\psi_{i-1,j}}{a_{i-1}}\right)}{\frac{1}{2}(a_i + a_{i-1})}$$

$$+\varepsilon_0 \frac{\varepsilon_{r,i,j+\frac{1}{2}}\left(\frac{\psi_{i,j+1}-\psi_{i,j}}{b_j}\right) - \varepsilon_{r,i,j-\frac{1}{2}}\left(\frac{\psi_{i,j}-\psi_{i,j-1}}{b_{j-1}}\right)}{\frac{1}{2}(b_j + b_{j-1})} . \tag{4.9}$$

We still do not have an explicit expression for the relative electrical permittivity. It is evident to approximate ε_r between two grid points by the mean value at the two neighbouring points

$$\varepsilon_{r,i\pm\frac{1}{2},j} = \frac{\varepsilon_{r,i\pm1,j} + \varepsilon_{r,i,j}}{2} , \qquad \varepsilon_{r,i,j\pm\frac{1}{2}} = \frac{\varepsilon_{r,i,j\pm1} + \varepsilon_{r,i,j}}{2} . \tag{4.10}$$

Equation (4.9) is now inserted into the Poisson equation (4.1), which results in

$$\begin{aligned} q\frac{n_{i,j} - p_{i,j}}{\varepsilon_0} = & \frac{\varepsilon_{r,i+\frac{1}{2},j}\left(\frac{\psi_{i+1,j}-\psi_{i,j}}{a_i}\right) - \varepsilon_{r,i-\frac{1}{2},j}\left(\frac{\psi_{i,j}-\psi_{i-1,j}}{a_{i-1}}\right)}{\frac{1}{2}(a_i + a_{i-1})} \\ & + \frac{\varepsilon_{r,i,j+\frac{1}{2}}\left(\frac{\psi_{i,j+1}-\psi_{i,j}}{b_j}\right) - \varepsilon_{r,i,j-\frac{1}{2}}\left(\frac{\psi_{i,j}-\psi_{i,j-1}}{b_{j-1}}\right)}{\frac{1}{2}(b_j + b_{j-1})} . \end{aligned} \tag{4.11}$$

As we see from the terms in equation (4.11), the potential at position (i,j) is determined by the potentials at the four nearest neighbour sites as well as the charge carrier densities at coordinates (i,j). We can reshape equation (4.11) to gain an explicit expression for $\psi_{i,j}$, which reads

$$\psi_{i,j} = \frac{1}{A}\left[B + C(\psi_{i+1,j}, \psi_{i,j+1}) + D(\psi_{i-1,j}, \psi_{i,j-1})\right] , \tag{4.12}$$

where we introduced the terms

$$A = \frac{\varepsilon_{r,i,j+\frac{1}{2}}}{b_j} + \frac{\varepsilon_{r,i,j-\frac{1}{2}}}{b_{j-1}} + \frac{\varepsilon_{r,i+\frac{1}{2},j}}{a_i} + \frac{\varepsilon_{r,i-\frac{1}{2},j}}{a_{i-1}} , \tag{4.13}$$

$$B = q\,\frac{n_{i,j} - p_{i,j}}{\varepsilon_0}\,\frac{b_j + b_{j-1}}{2}\,\frac{a_i + a_{i-1}}{2} , \tag{4.14}$$

$$C = \frac{a_i + a_{i-1}}{2}\left(\varepsilon_{r,i,j+1}\frac{\psi_{i,j+1}}{b_j}\right) + \frac{b_j + b_{j-1}}{2}\left(\varepsilon_{r,i+1,j}\frac{\psi_{i+1,j}}{a_i}\right) , \tag{4.15}$$

$$D = \frac{b_j + b_{j-1}}{2}\left(\varepsilon_{r,i-1,j}\frac{\psi_{i-1,j}}{a_{i-1}}\right) + \frac{a_i + a_{i-1}}{2}\left(\varepsilon_{r,i,j-1}\frac{\psi_{i,j-1}}{b_{j-1}}\right) . \tag{4.16}$$

The approximations for the relative permittivity are given in equation (4.10). The equations (4.12) to (4.16) are valid for $i \in [1, A]$ and $j \in [1, B]$. With this calculation we arrive at a system of equations that needs to be solved. The system consists of a very large number of individual equations making a iterative solution favourable to a direct one. An iteration process is numerically very stable. Another advantage of the iteration approach is the consideration of boundary conditions. In direct schemes they create new equations that have to be treated in the solving process. In an iteration process they are automatically included with the starting values of the iteration, which of course have to be set at the beginning. The easiest choice is to start at zero and let the system evolve towards the solution.

The evaluation of the potential starts at the top left grid point of the active layer (depicted in Fig. 4.1), defined by the indices $(i = 1, j = 1)$. It is carried out row-wise, starting at the top row, $i = 1$, proceeding from left to right, from $j = 1$ to $j = B$. The last point to be evaluated is $(i = A, j = B)$.

Considering this iteration scheme we can write down equations (4.12) to (4.16) for the iteration step $k + 1$,

$$\psi_{i,j}^{k+1} = \frac{1}{A}\left[B + C(\psi_{i+1,j}^{k}, \psi_{i,j+1}^{k}) + D(\psi_{i-1,j}^{k+1}, \psi_{i,j-1}^{k+1})\right] ,$$

with

$$\begin{aligned}
A &= \frac{\varepsilon_{r,i,j+\frac{1}{2}}}{b_j} + \frac{\varepsilon_{r,i,j-\frac{1}{2}}}{b_{j-1}} + \frac{\varepsilon_{r,i+\frac{1}{2},j}}{a_i} + \frac{\varepsilon_{r,i-\frac{1}{2},j}}{a_{i-1}} , \\
B &= q\,\frac{n_{i,j} - p_{i,j}}{\varepsilon_0}\,\frac{b_j + b_{j-1}}{2}\,\frac{a_i + a_{i-1}}{2} , \\
C &= \frac{a_i + a_{i-1}}{2}\left(\varepsilon_{r,i,j+1}\frac{\psi_{i,j+1}^{k}}{b_j}\right) + \frac{b_j + b_{j-1}}{2}\left(\varepsilon_{r,i+1,j}\frac{\psi_{i+1,j}^{k}}{a_i}\right) , \\
D &= \frac{b_j + b_{j-1}}{2}\left(\varepsilon_{r,i-1,j}\frac{\psi_{i-1,j}^{k+1}}{a_{i-1}}\right) + \frac{a_i + a_{i-1}}{2}\left(\varepsilon_{r,i,j-1}\frac{\psi_{i,j-1}^{k+1}}{b_{j-1}}\right) .
\end{aligned}$$

4.3 Scharfetter-Gummel algorithm

In this section we will describe the Scharfetter-Gummel algorithm for solving the drift-diffusion model (3.93). This alogrithm is an approximation scheme based on a first-order finite difference method. The reason for using this numerical method are stability concerns. For a simple finite difference method the simulation is not stable. It will either oscillate heavily or not converge at all.

We start the calculation at the expressions for the electron and hole current densities (2.1) and (2.2)

$$J_n(x, y, t) = q\, n(x, y, t)\mu_n(x, y)E(x, y, t) + D_n(x, y)q\nabla n(x, y, t) , \tag{4.17}$$

$$J_p(x, y, t) = q\, p(x, y, t)\mu_p(x, y)E(x, y, t) - D_p(x, y)q\nabla p(x, y, t) , \tag{4.18}$$

where we already inserted the expression for the thermal velocity (3.94), $U_T = \frac{D_{n/p}}{\mu_{n/p}}$. For simplicity the following steps will be demonstrated only for the x component of the electron equation (4.17). The procedure for more spatial directions is analogous, as is the case for the hole current. Thus, we start with the one-dimensional equation for the electron current density given by

$$ {}^{x}J_n(x,y,t) = q\,n(x,y,t)\mu_n(x,y)\,{}^{x}E(x,y,t) + D_n(x,y)q\frac{\partial n(x,y,t)}{\partial x}\,. \tag{4.19} $$

When employing the Scharfetter-Gummel algorithm, the given equation, in this case (4.19), is solved analytically in an interval on the x-axis $x \in [x_i, x_{i+1}]$ and an arbitrary value on the y-axis, $y = y_j$. To be able to solve the equation, we make the assumption that the x-component of the electron current density ${}^{x}J_n(x,y,t)$ is constant in the interval $[x_i, x_{i+1}]$. We denote the constant value by ${}^{x}J^t_{n,i+\frac{1}{2},j}$, where the index t represents the time. The main feature of the Scharfetter-Gummel approximation comes into play later, yet it will be explained here very briefly. The electron density $n(x,y,t)$ has a fixed value at both ends of the interval $[x_i, x_{i+1}]$, given by two boundary conditions. A one-dimensional differential equation has one degree of freedom. If two boundary conditions are given, as is the case here, another quantity has to be treated as a variable to conserve the number of degrees of freedom. For that reason the constant current density ${}^{x}J^t_{n,i+\frac{1}{2},j}$ is treated as an independent variable and will be calculated from the electron concentrations at either end of the interval, given by the boundary conditions. Further on, the so derived equations for the x- and y-components of both the electron and hole current densities will be combined with the discretized versions of the continuity equations (3.93).

But let us follow this calculation step by step. As already mentioned, we start with equation (4.19), assuming a constant electron current density per interval. For the electron mobility μ_n and the electron diffusivity D_n in this interval, we use their corresponding mean values

$$ \begin{aligned} \mu_{n,i+\frac{1}{2},j} &= \frac{\mu_{n,i,j} + \mu_{n,i+1,j}}{2}\,, \\ D_{n,i+\frac{1}{2},j} &= \frac{D_{n,i,j} + D_{n,i+1,j}}{2}\,. \end{aligned} $$

Additionally, we assume a linear generalized electric potential Ψ between the two points x_i and x_{i+1}. Thus, we calculate the electric field by the differential quotient,

$$ {}^{x}E^t_{i+\frac{1}{2},j} = -\frac{\Psi^t_{i+1,j} - \Psi^t_{i,j}}{x_{i+1} - x_i}\,. \tag{4.20} $$

The electric field ${}^{x}E^t_{i+\frac{1}{2},j}$ is constant in the interval $x \in [x_i, x_{i+1}]$.

Based on these preliminary discretizations and definitions we solve the differential equation (4.19). First, we treat the homogenous equation by making an exponential ansatz. Then a particular solution of the inhomogenous equation has to be found.

The general solution to the inhomogenous differential equation is then given by the sum of the homogenous and the particular solution. The homogenous form of equation (4.19) reads

$$a\, n(x,y,t) + b\frac{\partial n(x,y,t)}{\partial x} = 0\,,$$

with the constant factors

$$a = q\,\mu_{n,i+\frac{1}{2},j}\, {}^{x}E^{t}_{i+\frac{1}{2},j}\,, \qquad b = q\,D_{n,i+\frac{1}{2},j}\,.$$

We insert the ansatz

$$n(x,y,t) = Ce^{\lambda x}\,,$$

into the homogeneous equation and find

$$ae^{\lambda x} + \lambda b e^{\lambda x} = 0\,.$$

By solving this equation for λ we see that the homogenous solution is given by

$$n_{hom}(x,y,t) = Ce^{-\frac{a}{b}x}\,.$$

A particular solution of Eq. (4.19) can be found as

$$n_{part}(x,y,t) = \frac{{}^{x}J^{t}_{n,i+\frac{1}{2},j}}{a}\,. \tag{4.21}$$

Combining the homogenous and the particular solutions yields the general solution to the Eq. (4.19):

$$n(x,y,t) = n_{hom} + n_{part} = Ce^{-\frac{a}{b}x} + \frac{{}^{x}J^{t}_{n,i+\frac{1}{2},j}}{a}\,,$$

in the interval $x \in [x_i, x_{i+1}]$ and $y = y_j$. Now we use the boundary conditions fixing the values of the electron density $n(x,y,t)$ at both ends of the interval:

$$n^{t}_{i,j} = Ce^{-\frac{a}{b}x_i} + \frac{{}^{x}J^{t}_{n,i+\frac{1}{2},j}}{a}\,, \tag{4.22}$$

$$n^{t}_{i+1,j} = Ce^{-\frac{a}{b}x_{i+1}} + \frac{{}^{x}J^{t}_{n,i+\frac{1}{2},j}}{a}\,. \tag{4.23}$$

The constant C is calculated from (4.22)

$$C = \frac{n^{t}_{i,j} - \frac{{}^{x}J^{t}_{n,i+\frac{1}{2},j}}{a}}{e^{-\frac{a}{b}x_i}}$$

and inserted into (4.23). Some basic calculation steps are performed to obtain the following expression for the electron current density

$$ {}^{x}J^{t}_{n,i+\frac{1}{2},j} = a\,\frac{n^t_{i+1,j} - n^t_{i,j}\exp\left[-\frac{a}{b}(x_{i+1}-x_i)\right]}{1-\exp\left[-\frac{a}{b}(x_{i+1}-x_i)\right]} \,. $$

This equation for ${}^{x}J^{t}_{n,i+\frac{1}{2},j}$ can be simplified by extending it

$$ {}^{x}J^{t}_{n,i+\frac{1}{2},j} = \frac{b}{x_{i+1}-x_i}\left\{ n^t_{i+1,j}\frac{(x_{i+1}-x_i)\frac{a}{b}}{1-\exp\left[-\frac{a}{b}(x_{i+1}-x_i)\right]} - n^t_{i,j}\frac{-(x_{i+1}-x_i)\frac{a}{b}}{1-\exp\left[+\frac{a}{b}(x_{i+1}-x_i)\right]} \right\} , \tag{4.24} $$

and using the definition of the Bernoulli function

$$ B(x) = \frac{-x}{1-e^x} \,. $$

Inserting this definition into (4.24) yields

$$ {}^{x}J^{t}_{n,i+\frac{1}{2},j} = \frac{b}{x_{i+1}-x_i}\left\{ n^t_{i+1,j} B\left(-\frac{a}{b}(x_{i+1}-x_i)\right) - n^t_{i,j} B\left(+\frac{a}{b}(x_{i+1}-x_i)\right)\right\} \,. $$

At this point we reinsert the expressions $a = q\,\mu_{n,i+\frac{1}{2},j}\,{}^{x}E^{t}_{i+\frac{1}{2},j}$ and $b = q\,D_{n,i+\frac{1}{2},j}$ and obtain

$$ \begin{aligned} {}^{x}J^{t}_{n,i+\frac{1}{2},j} = \frac{qD_{n,i+\frac{1}{2},j}}{x_{i+1}-x_i} \Bigg\{ & n^t_{i+1,j} B\left(-\frac{q\,\mu_{n,i+\frac{1}{2},j}\,{}^{x}E^{t}_{i+\frac{1}{2},j}}{qD_{n,i+\frac{1}{2},j}}(x_{i+1}-x_i)\right) \\ & - n^t_{i,j} B\left(+\frac{q\,\mu_{n,i+\frac{1}{2},j}\,{}^{x}E^{t}_{i+\frac{1}{2},j}}{q\,D_{n,i+\frac{1}{2},j}}(x_{i+1}-x_i)\right)\Bigg\} \,. \end{aligned} \tag{4.25} $$

The argument of the Bernoulli function can be simplified by using the relation between the diffusion constant and the mobility (3.94), and expression (4.20) for the electric field:

$$ \begin{aligned} \frac{q\,\mu_{n,i+\frac{1}{2},j}\,{}^{x}E^{t}_{i+\frac{1}{2},j}}{q\,D_{n,i+\frac{1}{2},j}}(x_{i+1}-x_i) &= -\frac{1}{U_T}\frac{\Psi^t_{i+1,j}-\Psi^t_{i,j}}{x_{i+1}-x_i}(x_{i+1}-x_i) \\ &= -\frac{q(\Psi^t_{i+1,j}-\Psi^t_{i,j})}{k_B T} \,, \end{aligned} $$

where we made use of $U_T = \frac{k_B T}{q}$, for the thermal voltage, with the Boltzmann constant k_B. Combining this calculation with equation (4.25) results in

$$ {}^{x}J^{t}_{n,i+\frac{1}{2},j} = \frac{qD_{n,i+\frac{1}{2},j}}{x_{i+1}-x_i}\left\{ n^t_{i+1,j} B\left(\frac{q(\Psi^t_{i+1,j}-\Psi^t_{i,j})}{k_B T}\right) - n^t_{i,j} B\left(-\frac{q(\Psi^t_{i+1,j}-\Psi^t_{i,j})}{k_B T}\right)\right\} , $$

the x-component of the discretized drift-diffusion current for electrons at time t.

The procedure for the y-component and the whole calculation for the hole current are analogous. Here, only the results are given

$$ {}^{x}J^{t}_{n,i+\frac{1}{2},j} = \frac{qD_{n,i+\frac{1}{2},j}}{x_{i+1}-x_i} \left\{ n^t_{i+1,j} B\left(\frac{q(\Psi^t_{n,i+1,j}-\Psi^t_{n,i,j})}{k_B T}\right) - n^t_{i,j} B\left(-\frac{q(\Psi^t_{n,i+1,j}-\Psi^t_{n,i,j})}{k_B T}\right)\right\} , \tag{4.26} $$

$$ {}^{y}J^{t}_{n,i,j+\frac{1}{2}} = \frac{qD_{n,i,j+\frac{1}{2}}}{y_{j+1}-y_j} \left\{ n^t_{i,j+1} B\left(\frac{q(\Psi^t_{n,i,j+1}-\Psi^t_{n,i,j})}{k_B T}\right) - n^t_{i,j} B\left(-\frac{q(\Psi^t_{n,i,j+1}-\Psi^t_{n,i,j})}{k_B T}\right)\right\} , \tag{4.27} $$

$$ {}^{x}J^{t}_{p,i+\frac{1}{2},j} = -\frac{qD_{p,i+\frac{1}{2},j}}{x_{i+1}-x_i} \left\{ p^t_{i+1,j} B\left(-\frac{q(\Psi^t_{p,i+1,j}-\Psi^t_{p,i,j})}{k_B T}\right) - p^t_{i,j} B\left(\frac{q(\Psi^t_{p,i+1,j}-\Psi^t_{p,i,j})}{k_B T}\right)\right\} , \tag{4.28} $$

$$ {}^{y}J^{t}_{p,i,j+\frac{1}{2}} = -\frac{qD_{p,i,j+\frac{1}{2}}}{y_{j+1}-y_j} \left\{ p^t_{i,j+1} B\left(-\frac{q(\Psi^t_{p,i,j+1}-\Psi^t_{p,i,j})}{k_B T}\right) - p^t_{i,j} B\left(\frac{q(\Psi^t_{p,i,j+1}-\Psi^t_{p,i,j})}{k_B T}\right)\right\} . \tag{4.29} $$

For the simulations we also need the continuity equations (3.93). They are discretized by using a first-order finite difference approximation for the spatial derivatives occuring in the continuity equations. The discretized versions of (3.93) read

$$ \frac{\partial}{\partial t} n^t_{i,j} - \frac{1}{q}\frac{{}^{x}J^{t}_{n,i+\frac{1}{2},j} - {}^{x}J^{t}_{n,i-\frac{1}{2},j}}{\frac{1}{2}(x_{i+1}-x_{i-1})} - \frac{1}{q}\frac{{}^{y}J^{t}_{n,i,j+\frac{1}{2}} - {}^{y}J^{t}_{n,i,j-\frac{1}{2}}}{\frac{1}{2}(y_{j+1}-y_{j-1})} = G^t_{i,j} - R^t_{i,j} , $$

$$ \frac{\partial}{\partial t} p^t_{i,j} + \frac{1}{q}\frac{{}^{x}J^{t}_{p,i+\frac{1}{2},j} - {}^{x}J^{t}_{p,i-\frac{1}{2},j}}{\frac{1}{2}(x_{i+1}-x_{i-1})} + \frac{1}{q}\frac{{}^{y}J^{t}_{p,i,j+\frac{1}{2}} - {}^{y}J^{t}_{p,i,j-\frac{1}{2}}}{\frac{1}{2}(y_{j+1}-y_{j-1})} = G^t_{i,j} - R^t_{i,j} , $$

where G represents the charge carrier generation rate and R the recombination rate. To deal with the time derivative we apply an implicit Euler backward method [15], which yields

$$ \frac{n^{t+\Delta t}_{i,j} - n^t_{i,j}}{\Delta t} - \frac{1}{q}\frac{{}^{x}J^{t+\Delta t}_{n,i+\frac{1}{2},j} - {}^{x}J^{t+\Delta t}_{n,i-\frac{1}{2},j}}{\frac{1}{2}(x_{i+1}-x_{i-1})} - \frac{1}{q}\frac{{}^{y}J^{t+\Delta t}_{n,i,j+\frac{1}{2}} - {}^{y}J^{t+\Delta t}_{n,i,j-\frac{1}{2}}}{\frac{1}{2}(y_{j+1}-y_{j-1})} = G^{t+\Delta t}_{i,j} - R^{t+\Delta t}_{i,j} , \tag{4.30} $$

$$ \frac{p^{t+\Delta t}_{i,j} - p^t_{i,j}}{\Delta t} + \frac{1}{q}\frac{{}^{x}J^{t+\Delta t}_{p,i+\frac{1}{2},j} - {}^{x}J^{t+\Delta t}_{p,i-\frac{1}{2},j}}{\frac{1}{2}(x_{i+1}-x_{i-1})} + \frac{1}{q}\frac{{}^{y}J^{t+\Delta t}_{p,i,j+\frac{1}{2}} - {}^{y}J^{t+\Delta t}_{p,i,j-\frac{1}{2}}}{\frac{1}{2}(y_{j+1}-y_{j-1})} = G^{t+\Delta t}_{i,j} - R^{t+\Delta t}_{i,j} . \tag{4.31} $$

Now we have to insert the expressions for the current density, equations (4.26) to (4.29), into the discretized continuity equations (4.30), (4.31). This yields a system of very long equations containing $n^{t+\Delta t}$ and $p^{t+\Delta t}$ respectively at the five spatial positions $(i,j),(i+1,j),(i-1,j),(i,j+1),(i,j-1)$ and the potentials at time $t+\Delta t$ at the same spatial positions. The equations also contain $n^t_{i,j}$ and $p^t_{i,j}$ respectively, the electron and hole densities at the coordinates (i,j) at the previous time step t. This means, we can find expressions for the new densities $n^{t+\Delta t}_{i,j}$ and $p^{t+\Delta t}_{i,j}$ at the coordinates (i,j) at time $t+\Delta t$. They depend on the densities of the nearest neighbours at the same time step $t+\Delta t$ and the densities at the considered location (i,j) at the previous time step t:

$$\begin{aligned}
n^{t+\Delta t}_{i,j} = \Bigg[& \left(-R^{t+\Delta t}_{i,j} + G^{t+\Delta t}_{i,j} + \frac{n^t_{i,j}}{\Delta t}\right) \frac{a_{i-1}+a_i}{2}\frac{b_{j-1}+b_j}{2} \\
& + n^{t+\Delta t}_{i+1,j} D_{n,i+\frac{1}{2},j} B\left(\frac{\Psi^{t+\Delta t}_{n,i+1,j} - \Psi^{t+\Delta t}_{n,i,j}}{U_T}\right)\frac{b_{j-1}+b_j}{2a_i} \\
& + n^{t+\Delta t}_{i,j+1} D_{n,i,j+\frac{1}{2}} B\left(\frac{\Psi^{t+\Delta t}_{n,i,j+1} - \Psi^{t+\Delta t}_{n,i,j}}{U_T}\right)\frac{a_{i-1}+a_i}{2b_j} \\
& + n^{t+\Delta t}_{i,j-1} D_{n,i,j-\frac{1}{2}} B\left(\frac{\Psi^{t+\Delta t}_{n,i,j-1} - \Psi^{t+\Delta t}_{n,i,j}}{U_T}\right)\frac{a_{i-1}+a_i}{2b_{j-1}} \\
& + n^{t+\Delta t}_{i-1,j} D_{n,i-\frac{1}{2},j} B\left(\frac{\Psi^{t+\Delta t}_{n,i-1,j} - \Psi^{t+\Delta t}_{n,i,j}}{U_T}\right)\frac{b_{j-1}+b_j}{2a_{i-1}}\Bigg] \\
\times \Bigg[& D_{n,i,j-\frac{1}{2}} B\left(\frac{\Psi^{t+\Delta t}_{n,i,j} - \Psi^{t+\Delta t}_{n,i,j-1}}{U_T}\right)\frac{a_{i-1}+a_i}{2b_{j-1}} \\
& + D_{n,i-\frac{1}{2},j} B\left(\frac{\Psi^{t+\Delta t}_{n,i,j} - \Psi^{t+\Delta t}_{n,i-1,j}}{U_T}\right)\frac{b_{j-1}+b_j}{2a_{i-1}} \\
& + D_{n,i+\frac{1}{2},j} B\left(\frac{\Psi^{t+\Delta t}_{n,i,j} - \Psi^{t+\Delta t}_{n,i+1,j}}{U_T}\right)\frac{b_{j-1}+b_j}{2a_i} \\
& + D_{n,i,j+\frac{1}{2}} B\left(\frac{\Psi^{t+\Delta t}_{n,i,j} - \Psi^{t+\Delta t}_{n,i,j+1}}{U_T}\right)\frac{a_{i-1}+a_i}{2b_j} \\
& + \frac{1}{\Delta t}\frac{a_{i-1}+a_i}{2}\frac{b_{j-1}+b_j}{2}\Bigg]^{-1},
\end{aligned} \tag{4.32}$$

where $i = 1, ..., A$ and $j = 1, ..., B$. The following abbreviations were used:

- $a_i = x_{i+1} - x_i$
- $b_j = y_{j+1} - y_j$
- $U_T = \frac{k_B T}{q}$

For holes the expression reads:

$$
\begin{aligned}
p_{i,j}^{t+\Delta t} = \Bigg[& \left(-R_{i,j}^{t+\Delta t} + G_{i,j}^{t+\Delta t} + \frac{p_{i,j}^{t}}{\Delta t} \right) \frac{a_{i-1}+a_i}{2} \frac{b_{j-1}+b_j}{2} \\
& + p_{i+1,j}^{t+\Delta t} D_{p,i+\frac{1}{2},j} B\left(\frac{\Psi_{p,i,j}^{t+\Delta t} - \Psi_{p,i+1,j}^{t+\Delta t}}{U_T} \right) \frac{b_{j-1}+b_j}{2a_i} \\
& + p_{i,j+1}^{t+\Delta t} D_{p,i,j+\frac{1}{2}} B\left(\frac{\Psi_{p,i,j}^{t+\Delta t} - \Psi_{p,i,j+1}^{t+\Delta t}}{U_T} \right) \frac{a_{i-1}+a_i}{2b_j} \\
& + p_{i,j-1}^{t+\Delta t} D_{p,i,j-\frac{1}{2}} B\left(\frac{\Psi_{p,i,j}^{t+\Delta t} - \Psi_{p,i,j-1}^{t+\Delta t}}{U_T} \right) \frac{a_{i-1}+a_i}{2b_{j-1}} \\
& + p_{i-1,j}^{t+\Delta t} D_{p,i-\frac{1}{2},j} B\left(\frac{\Psi_{p,i,j}^{t+\Delta t} - \Psi_{p,i-1,j}^{t+\Delta t}}{U_T} \right) \frac{b_{j-1}+b_j}{2a_{i-1}} \Bigg] \\
\times \Bigg[& D_{p,i,j-\frac{1}{2}} B\left(\frac{\Psi_{p,i,j-1}^{t+\Delta t} - \Psi_{p,i,j}^{t+\Delta t}}{U_T} \right) \frac{a_{i-1}+a_i}{2b_{j-1}} \\
& + D_{p,i-\frac{1}{2},j} B\left(\frac{\Psi_{p,i-1,j}^{t+\Delta t} - \Psi_{p,i,j}^{t+\Delta t}}{U_T} \right) \frac{b_{j-1}+b_j}{2a_{i-1}} \\
& + D_{p,i+\frac{1}{2},j} B\left(\frac{\Psi_{p,i+1,j}^{t+\Delta t} - \Psi_{p,i,j}^{t+\Delta t}}{U_T} \right) \frac{b_{j-1}+b_j}{2a_i} \\
& + D_{p,i,j+\frac{1}{2}} B\left(\frac{\Psi_{p,i,j+1}^{t+\Delta t} - \Psi_{p,i,j}^{t+\Delta t}}{U_T} \right) \frac{a_{i-1}+a_i}{2b_j} \\
& + \frac{1}{\Delta t} \frac{a_{i-1}+a_i}{2} \frac{b_{j-1}+b_j}{2} \Bigg]^{-1},
\end{aligned}
\tag{4.33}
$$

with $i = 1, ..., A$ and $j = 1, ..., B$. The following abbreviations were used:

- $a_i = x_{i+1} - x_i$
- $b_j = y_{j+1} - y_j$
- $U_T = \frac{k_B T}{q}$

The system of equations (4.32) and (4.33) has to be solved. This is done iteratively for the same reasons as already explained in Section 4.2. The iteration needs starting values for $n_{i,j}^{t=0}$ and $p_{i,j}^{t=0}$, which in the simplest case will be chosen as zero. The evaluation is performed in the same way as for the potential, meaning the calculation starts at the top left grid point and progresses row wise from left to right to the bottom right grid point. It then starts again in the top left corner.

We still need explicit information on the charge carrier generation and recombination rates $G_{i,j}^{t+\Delta t}$ and $R_{i,j}^{t+\Delta t}$. For the generation rate we have to consider the exciton distribution. As already stated in Chapter 2, excitons are generated by light absorption in the organic semiconductor. They then can diffuse until they either recombine and are lost for the simulation or dissociate into an electron-hole pair. This behaviour is described by the continuity equation for excitons (2.10)

$$\frac{\partial ex(x,y,t)}{\partial t} = G_{ex}(x,y) - R_{ex}(x,y,t) - G(x,y,t) - \frac{1}{q}\nabla\,\Phi(x,y,t)\,, \tag{4.34}$$

where the exciton flux density is given by (2.8)

$$\Phi_{ex}(x,y,t) = -k_B T \mu_{ex} \nabla\, ex(x,y,t)\,. \tag{4.35}$$

Here, $ex(x,y,t)$ denotes the exciton density at position (x,y) at time t. The terms G_{ex} and R_{ex} give the exciton generation and recombination rates. The generation rate is independent of time as the illumination of the device does not change over time. The recombination rate, however, is time dependent. $G(x,y,t)$ gives the generation rate of electron-hole pairs, it equals the dissociation rate of excitons. Therefore, it is a loss term in the exciton continuity equation. The last term represents excitons gained or lost at position (x,y) due to exciton diffusion.

The discretized versions of the x- and y-component of (4.35) read

$$^{x}\Phi^{t+\Delta t}_{ex,i+\frac{1}{2},j} = -k_B T \mu_{ex,i+\frac{1}{2},j} \frac{ex^{t+\Delta t}_{i+1,j} - ex^{t+\Delta t}_{i,j}}{a_i}\,. \tag{4.36}$$

$$^{y}\Phi^{t+\Delta t}_{ex,i,j+\frac{1}{2}} = -k_B T \mu_{ex,i,j+\frac{1}{2}} \frac{ex^{t+\Delta t}_{i,j+1} - ex^{t+\Delta t}_{i,j}}{b_j}\,, \tag{4.37}$$

Next we discretize the exciton continuity equation (4.34), also considering the temporal derivative by an implicit Euler backwards method. It is the same procedure as for the electron and hole continuity equations. We get

$$\frac{ex^{t+\Delta t}_{i,j} - ex^{t}_{i,j}}{\Delta t} =$$

$$G^{t+\Delta t}_{ex,i,j} - R^{t+\Delta t}_{ex,i,j} - G^{t+\Delta t}_{i,j} - \frac{1}{q}\left(\frac{^{x}\Phi^{t+\Delta t}_{ex,i+\frac{1}{2},j} - {}^{x}\Phi^{t+\Delta t}_{ex,i-\frac{1}{2},j}}{\frac{1}{2}(a_i + a_{i-1})} + \frac{^{y}\Phi^{t+\Delta t}_{ex,i,j+\frac{1}{2}} - {}^{y}\Phi^{t+\Delta t}_{ex,i,j-\frac{1}{2}}}{\frac{1}{2}(b_j + b_{j-1})}\right)$$

as a result. Inserting the expressions (4.36) and (4.37) into the discretized continuity equation (4.3) yields

$$\frac{ex_{i,j}^{t+\Delta t}-ex_{i,j}^{t}}{\Delta t}=G_{ex,i,j}^{t+\Delta t}-R_{ex,i,j}^{t+\Delta t}-G_{i,j}^{t+\Delta t}$$

$$+\frac{2k_BT}{q(a_i+a_{i-1})}\left[\mu_{ex,i+\frac{1}{2},j}\frac{ex_{i+1,j}^{t+\Delta t}-ex_{i,j}^{t+\Delta t}}{a_i}-\mu_{ex,i-\frac{1}{2},j}\frac{ex_{i,j}^{t+\Delta t}-ex_{i-1,j}^{t+\Delta t}}{a_{i-1}}\right]$$

$$+\frac{2k_BT}{q(b_j+b_{j-1})}\left[\mu_{ex,i,j+\frac{1}{2}}\frac{ex_{i,j+1}^{t+\Delta t}-ex_{i,j}^{t+\Delta t}}{b_j}-\mu_{ex,i,j-\frac{1}{2}}\frac{ex_{i,j}^{t+\Delta t}-ex_{i,j-1}^{t+\Delta t}}{b_{j-1}}\right].$$

Again we are interested in a representation of the form

$$ex_{i,j}^{t+\Delta t}=f(ex_{i,j}^{t},ex_{i+1,j}^{t+\Delta t},ex_{i-1,j}^{t+\Delta t},ex_{i,j+1}^{t+\Delta t},ex_{i,j-1}^{t+\Delta t}).$$

After a few basic calculation steps we obtain

$$\begin{aligned}ex_{i,j}^{t+\Delta t}=&\Bigg[\left(G_{ex,i,j}^{t+\Delta t}-R_{ex,i,j}^{t+\Delta t}-G_{i,j}^{t+\Delta t}+\frac{ex_{i,j}^{t}}{\Delta t}\right)\frac{a_{i-1}+a_i}{2}\frac{b_{j-1}+b_j}{2}\\&+\frac{a_i+a_{i-1}}{2b_{j-1}}D_{ex,i,j-\frac{1}{2}}ex_{i,j-1}^{t+\Delta t}+\frac{b_j+b_{j-1}}{2a_{i-1}}D_{ex,i-\frac{1}{2},j}ex_{i-1,j}^{t+\Delta t}\\&+\frac{a_i+a_{i-1}}{2b_j}D_{ex,i,j+\frac{1}{2}}ex_{i,j+1}^{t+\Delta t}+\frac{b_j+b_{j-1}}{2a_i}D_{ex,i+\frac{1}{2},j}ex_{i+1,j}^{t+\Delta t}\Bigg]\\&\times\Bigg[\frac{a_i+a_{i-1}}{2b_{j-1}}D_{ex,i,j-\frac{1}{2}}+\frac{b_j+b_{j-1}}{2a_{i-1}}D_{ex,i-\frac{1}{2},j}\\&+\frac{a_i+a_{i-1}}{2b_j}D_{ex,i,j+\frac{1}{2}}+\frac{b_j+b_{j-1}}{2a_i}D_{ex,i+\frac{1}{2},j}\\&+\frac{1}{\Delta t}\frac{a_{i-1}+a_i}{2}\frac{b_{j-1}+b_j}{2}\Bigg]^{-1},\end{aligned}\tag{4.38}$$

where we made use of the relation (2.9):

- $\frac{k_BT}{q}\mu_{ex,i\pm\frac{1}{2},j}=D_{ex,i\pm\frac{1}{2},j}$,
- $\frac{k_BT}{q}\mu_{ex,i,j\pm\frac{1}{2}}=D_{ex,i,j\pm\frac{1}{2}}$.

Altogether we now have three sytems of equations that need to be solved simultaneously. Thus, we evaluate the equations (4.32), (4.33) and (4.38) in the active region defined by $i\in[1,A]$ and $j\in[1,B]$ iteratively.

4.4 Charge generation and recombination rates

To evaluate the equations (4.32), (4.33) and (4.38) we need to specify the different generation and recombination rates G, R and G_{ex}, R_{ex}.

Exciton generation rate $G_{ex}^{t+\Delta t}$

In our simulation we assume that all the incoming photons generate excitons. There are no competitive processes that reduce it. In the simulation light enters the device through the top electrode passes straight through both semiconductors without diffraction, is reflected at the back electrode at an angle of 0° and travels back to the top electrode on a straight path, where it leaves the device. On its way through the organic semiconductors light is absorbed according to Lambert-Beer's law [47]

$$I(y=d) = I(y=0)e^{-\alpha d}\,, \tag{4.39}$$

with $I(y=0)$ denoting the light intensity at the starting point, $I(y=d)$ the intensity at a distance d from the starting point. The symbol α denotes the absorption coefficient.

In our simulations the AM 1.5 spectrum is used for the incoming light, see Section 2.6. The spectrum is given in units of $Wm^{-2}nm^{-1}$. Light is absorbed if its wavelength is smaller than a maximum wavelength $\lambda_{max} = \frac{hc}{E_{gap}}$, with h the Planck constant and c the speed of light. This maximum wavelength corresponds to the bandgap energy E_{gap}, meaning the minimal energy difference between the LUMO and HOMO levels of the organic semiconductors. Only photons with an energy higher than the bandgap energy can be absorbed.

The intensity at every grid box boundary is calculated as follows for light traversing the device from the top to the bottom contact

$$I^1(x_i, y_j, \lambda) = I^1_{i,j}(\lambda) = I^1_{i,j-1}(\lambda)\;\exp\left[-\alpha_{i,j}(\lambda)\,\frac{\Delta y_j + \Delta y_{j-1}}{2}\right]\,,$$

where $I^1_{i,j}(\lambda)$ is the light intensity of wavelength λ reaching the boundary between the grid boxes (x_i, y_{j-1}) and (x_i, y_j). The intensity at each grid box boundary (x_i, y_j) is calculated from the intensity at the previous grid box boundary (x_i, y_{j-1}), for $1 \leqslant j < B$ and $1 \leqslant i \leqslant A$. The intensity is measured in units of $Wm^{-2}nm^{-1}$. The grid spacing Δy is defined as $\Delta y_j = y_j - y_{j-1}$. In our simulations the absorption coefficient $\alpha_{i,j}(\lambda)$ varies with position and wavelength, as the two semiconductors have different absorption spectra, see Fig. 5.8. We consider the case $j = 0$ separately, using the AM 1.5 spectrum $I_{AM1.5}(\lambda)$ as starting intensity:

$$I^1_{i,0}(\lambda) = I_{AM1.5}(\lambda)\;\exp\left[-\alpha_{i,0}(\lambda)\,\frac{\Delta y_0}{2}\right]\,.$$

For the simulation we need the photon density $P^1_{i,j}$ at the grid box boundaries (i,j), not the intensity. It can be calculated from the intensity with the relation

$I = Ph\nu = Ph\frac{c}{\lambda}$, with the frequency ν, the Planck constant h and the speed of light c. We must also take the sum over all absorbable wavelengths:

$$P^1_{i,j} = \sum_{k=1}^{k_{max}} I^1_{i,j}(\lambda_k)\,\Delta\lambda\frac{\lambda_k}{hc}\,.$$

$P^1_{i,j}$ is the photon density reaching the boundary between the grid box (x_i, y_{j-1}) and (x_i, y_j) per unit of time. It is given in units of $m^{-2}s^{-1}$. Here $\Delta\lambda = \lambda_{k+1} - \lambda_k$ is the constant grid spacing of the wavelength.

In the next step the intensity of the reflected light is calculated

$$I^2(x_i, y_j, \lambda) = I^2_{i,j}(\lambda) = I^2_{i,j+1}(\lambda)\ \exp\left[-\alpha_{i,j+1}(\lambda)\,\frac{\Delta y_j + \Delta y_{j+1}}{2}\right]\,,$$

for $1 \leqslant i \leqslant A$, and $B - 1 \geqslant j > 0$. Again, the case $j = B$ is considered separately

$$I^2_{i,B}(\lambda) = I^1_{i,B}(\lambda)\ \exp\left[-\alpha_{i,B+1}(\lambda)\,\Delta y_B\right]\,.$$

There is no factor $\frac{1}{2}$ in the exponent, because light travels the distance $\frac{\Delta y_B}{2}$ twice. The according photon density of the reflected light at the grid box boundary (i, j) is evaluated in the same way as for the incoming light

$$P^2_{i,j} = \sum_{k=1}^{k_{max}} I^2_{i,j}(\lambda_k)\,\Delta\lambda\frac{\lambda_k}{hc}\,.$$

We are interested in how many photons are absorbed in one grid box per time unit. It is calculated from the differences in the photon density at the grid box boundaries in y-direction. This value still has to be divided by the grid box length in y-direction to give the photon density in units of $m^{-3}s^{-1}$. Thus, the absorbed photon density for each grid box (i, j) is calculated by

$$G^{t+\Delta t}_{ex,i,j} = \frac{2}{\Delta y_j + \Delta y_{j-1}}\left(P^1_{i,j-1} - P^1_{i,j} + P^2_{i,j} - P^2_{i,j-1}\right)\,,$$

for $1 \leqslant i \leqslant A$ and $1 \leqslant j \leqslant B$. This equation includes the contributions of the incoming and the reflected light.

Exciton recombination rate $R^{t+\Delta t}_{ex,i,j}$

If an exciton does not encounter an organic-organic interface during a certain period of time after generation it recombines and is lost for the simulation. This process is described by the exciton recombination rate

$$R^{t+\Delta t}_{ex,i,j} = \frac{ex^{t+\Delta t}_{i,j}}{\tau_{ex}}\,,$$

with the exciton lifetime τ_{ex}. In the simulation the value is set to $\tau_{ex} = 10^{-9}\,\mathrm{s}$. This value is chosen so that the mean diffusion length before recombination is approximately $\sigma \approx 15\,\mathrm{nm}$, [38]. We calculate the exciton diffusion constant D_{ex} from the equation [38]

$$\sigma = \sqrt{D_{ex}\,\tau_{ex}}\,.$$

to be $D_{ex} = 2.25 \cdot 10^{-7}\,\mathrm{m^2 s^{-1}}$.

Exciton dissociation rate $G_{i,j}^{t+\Delta t}$

Next we need an expression for $G_{i,j}^{t+\Delta t}$, the charge carrier generation rate, which equals the exciton dissociation rate. It depends on the solar cell. In this work we only consider solar cells built out of organic semiconductors. In this type of device excitons can only dissociate at an organic-organic interface [3]. Excitons are generated by incoming light and diffuse according to their mobility. If they encounter an organic-organic interface during their lifetime they dissociate immediately. In this code this behaviour is modelled by using two different lifetimes τ. The value $\tau_1 = 10^3\,\mathrm{s}$ is the mean time before an exciton dissociates in the organic semiconductor and $\tau_2 = 10^{-12}\,\mathrm{s}$ is the mean time before an exciton dissociates at the organic-organic interface. These values are chosen to ensure that no excitons dissociate in the semiconductor and all excitons meeting the interface dissociate instantaneously, which is the physical situation that we want to reproduce. Thus, these arbitrary choices of dissociation-lifetimes are justified by the correct physical output they provide. So we gain the expression for exciton dissociation

$$\begin{aligned} G_{i,j}^{t+\Delta t} &= \frac{ex_{i,j}^{t+\Delta t}}{\tau_1}, \qquad j \neq \frac{B}{2}, \frac{B}{2}+1 \\ G_{i,j}^{t+\Delta t} &= \frac{ex_{i,j}^{t+\Delta t}}{\tau_2}, \qquad j = \frac{B}{2}, \frac{B}{2}+1 \end{aligned}$$

The interface is situated between the two rows of grid-points characterized by $(i, \frac{B}{2})$ and $(i, \frac{B}{2}+1)$. Excitons dissociate in both of these rows. An exciton dissociating at $(i, \frac{B}{2})$ leaves an electron and a hole at position $(i, \frac{B}{2})$. The same goes for the row $(i, \frac{B}{2}+1)$.

Here, τ_1 is chosen much larger than τ_{ex} and τ_2 is still comfortably smaller than τ_{ex}. This choice of parameters gives the excitons enough time to diffuse to the interface before recombining, yet some of them do recombine. Upon reaching the interface, all excitons dissociate immediately into an electron-hole pair.

Electron-hole recombination rate $R_{i,j}^{t+\Delta t}$

The electron hole recombination rate is assumed to follow Langevin-recombination [7]

$$R(x,y,t) = \gamma\, n(x,y,t)\, p(x,y,t)\,, \tag{4.40}$$

with $\gamma = \frac{q\mu}{\varepsilon_0\varepsilon_r}$ and $\mu = \min[\mu_n, \mu_p]$. The formula describes a recombination process that is determined by the electron and hole concentrations at position (x, y) at time t. It is also directly proportional to the mobility of the slower charge carrier. This means, the more charge carriers are concentrated at one point and the higher their mobility, the more likely they are to recombine. It should be noted here that the direct dependence on the mobility and thus the diffusion constant means that the Langevin expression models diffusion-controlled recombination.

The discretized version of (4.40) reads

$$R_{i,j}^{t+\Delta t} = \gamma\, n_{i,j}^{t+\Delta t}\, p_{i,j}^{t+\Delta t}\,,$$

with $\gamma = \frac{q\mu_{i,j}}{\varepsilon_0\varepsilon_r}$ and $\mu_{i,j} = \min[\mu_{n,i,j}, \mu_{p,i,j}]$.

4.5 Contacts

The semiconductor-contact interface poses a potential barrier for charge carriers. Its height is determined by the difference between the contact workfunction and the electron/hole transport level in the semiconductor given by the LUMO/HOMO levels. This potential barrier is influenced by the acting electric field in the device. If the field component perpendicular to the contact rises towards the contact it bends down the injection barrier enabling a tunneling current, controlled by the barrier width. If the electric field bends the barrier strongly, its width will be small and the tunneling current noticeable. If the electric field decreases towards the contact the barrier is not reduced and no tunneling current can occur. In fact the potential rises even more.

The calculation will be demonstrated for holes. The electron case is analogous. We start from the mathematical description of a Schottky barrier at the interface [23, 24, 25, 26].

$$U(x, y) = \Phi - \frac{q^2}{16\pi\varepsilon_0\varepsilon_r(x, y = 0)y} - qE_\perp(x, y = 0)y\,, \tag{4.41}$$

where U is the effective barrier height, Φ the nominal injection barrier given by the difference between the workfunction of the contact and the HOMO transport level, and $E_\perp$ the elelectric field component perpendicular to the contact. We take the values of ε_r and $E_\perp$ at the contact ($y = 0$). The injection barrier according to equation (4.41) is plotted in Fig. 4.2 as a function of the distance from the contact y. The three differenct cases for $E_\perp$ are shown.

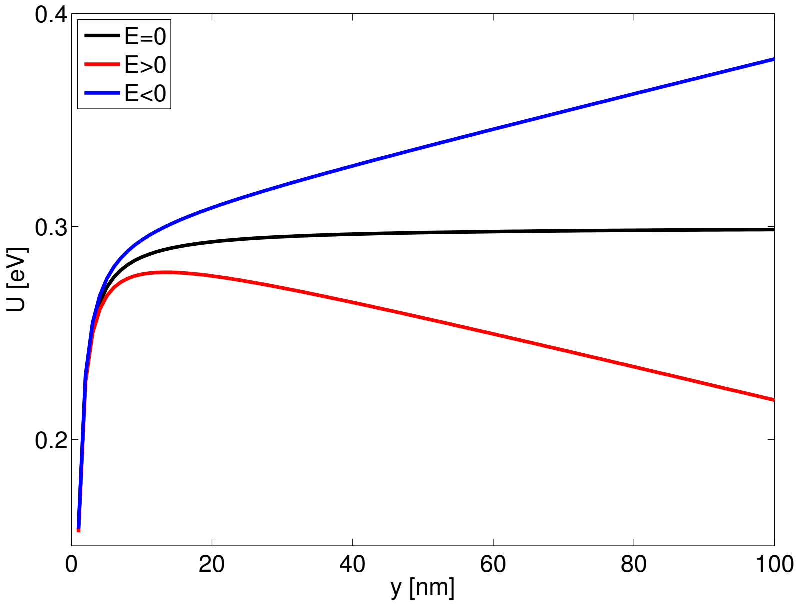

Figure 4.2: Schottky barrier at the contact-semiconductor interface where the contact is located at $y = 0$ and the semiconductor is situated at $y > 0$. The barrier shapes for $E_\perp = 0$, $E_\perp > 0$ and $E_\perp < 0$ are shown.

For $E_\perp > 0$ the barrier is bent down by the field. In this case it has a distinct maximum height. It can be found analytically by taking the derivative of (4.41) with respect to y and setting it equal to zero. By this method we find that the barrier has its maximum value at

$$y_{max} = \left(\frac{q}{E_\perp(x, y = 0) 16\pi\varepsilon_0\varepsilon_r(x, y = 0)} \right)^{\frac{1}{2}} ,$$

and consequently

$$U_{max}(x) = \Phi - \sqrt{\frac{q^3 E_\perp(x, y = 0)}{4\pi\varepsilon_0\varepsilon_r(x, y = 0)}} .$$

We have to distinguish between two different cases:

- $E_\perp < 0$: If the electric field is negative, the barrier is not reduced by the electric field. No thermionic injection or tunneling can occur.
- $E_\perp > 0$: A positive electric field bends down the injection barrier and thermionic emission into the semiconductor and tunneling occur, their current densities being determined by the barrier height and width.

The current density due to thermionic emission in y-direction is given by [27, 25]

$$J_{th}(x) = AT^2 \exp\left(-\frac{U_{max}(x)}{k_B T} \right) , \tag{4.42}$$

with the Richardson constant A and the temperature T. The Boltzmann constant is denoted by k_B. Thermionic emission is, as the name suggests a process primarily regulated by the temperature. The tunneling current on the other hand is explicitly temperature independent. It strongly correlates with the width of the potential barrier. The expression for the tunneling current density in the WKB approximation is given by [23], [25]

$$J_{tu}(x) = J_t \left[\frac{E_\perp(x, y = 0)}{E_t t(h(x))}\right]^2 \exp\left[-\frac{E_t v(h(x))}{E_\perp(x, y = 0)}\right] , \tag{4.43}$$

with the constant factors

$$J_t = \frac{q\Phi^2}{9(\pi a_0)^2 \hbar R} , \qquad E_t = \frac{4\Phi^{\frac{3}{2}}}{3qa_0\sqrt{R}} ,$$

where a_0 denotes the Bohr radius and R the Rydberg constant. The functions $h(x)$, $v(h(x))$, $t(h(x))$ are given by

$$\begin{aligned} h(x) &= \Phi^{-1} q \sqrt{\frac{qE_\perp(x, y = 0)}{4\pi\varepsilon_0\varepsilon_r(x, y = 0)}} , \\ v(h(x)) &= [1 + h(x)]^{\frac{1}{2}} \left\{ \mathcal{E}\left(\sqrt{\frac{1 - h(x)}{1 + h(x)}}\right) - h(x)\, \mathcal{K}\left(\sqrt{\frac{1 - h(x)}{1 + h(x)}}\right) \right\} , \\ t(h(x)) &= [1 + h(x)]^{-\frac{1}{2}} \left\{ (1 + h(x))\, \mathcal{E}\left(\sqrt{\frac{1 - h(x)}{1 + h(x)}}\right) - h(x)\, \mathcal{K}\left(\sqrt{\frac{1 - h(x)}{1 + h(x)}}\right) \right\} . \end{aligned}$$

Here $\mathcal{E}(\mathcal{X})$ and $\mathcal{K}(\mathcal{X})$ are the complete elliptic differential integrals of argument $\mathcal{X}$ of first and second kind [27, 25].

The two components J_{th} and J_{tu} constitute the current density going from the contact into the semiconductor. Flowing out of the device we have to consider the back drift current density J_{bd} [27] and the interface recombination current density J_{ir} [27, 25]. They constitute the backflowing current density J_{bf}

$$J_{bf}(x) = J_{bd}(x) + J_{ir}(x) .$$

The back drift current density is given by [27]

$$J_{bd} = \begin{cases} \mu_p(x, y)p(x)E_y(x) & E_\perp(x) < 0 \\ 0 & E_\perp(x) > 0 . \end{cases}$$

The interface recombination current density has the form [25]

$$J_{ir} = \frac{AT^2}{n_0} p(x) ,$$

with the density of occupiable states n_0, which is chosen according to [25], the hole density in the semiconductor $p(x)$ and the hole mobility μ_p. The above stated equations have to be discretized. The relative dielectric permittivity ε_r is taken at positions $(i, j = 1)$ for the top contact and $(i, j = B)$ for the bottom contact. The electric field component in y-direction for the top contact is calculated as a mean value over two rows

$$E_{\perp,top,i} = \frac{\psi_{i,2} - \psi_{i,0}}{y_2 - y_0} \, ,$$

where the electrostatic potential is denoted by ψ. The field at the bottom contact is calculated by

$$E_{\perp,bottom,i} = \frac{\psi_{i,B+1} - \psi_{i,B-1}}{y_{B+1} - y_{B-1}} \, ,$$

The nominal injection barrier Φ entering equation (4.41) for the top contact is given by

$$\Phi = |\Theta_{p,i,1} - \Phi_1| \, ,$$

where $\Theta_{p,i,1}$ is the HOMO transport level at spatial position $(i, j = 1)$ and Φ_1 denotes the workfunction of the top contact. The bottom contact is treated analogously.

The current densities J_{th}, J_{tu}, J_{bd}, J_{ir} are evaluated at the top contact for holes and at the bottom contact for electrons. Electrons are only injected from the bottom contact. Therefore, equation (4.32) has to be altered for $j = B$ to include the current densities described above. The terms containing the electron density at the bottom contact, namely $n_{i,B+1}^{t+\Delta t}$, are substituted. The altered version of equation (4.32) reads

$$
\begin{aligned}
n_{i,B}^{t+\Delta t} = \Bigg[& \left(-R_{i,B}^{t+\Delta t} + G_{i,B}^{t+\Delta t} + \frac{n_{i,B}^{t}}{\Delta t} \right) \frac{a_{i-1}+a_i}{2} \frac{b_{B-1}+b_B}{2} \\
& + n_{i+1,B}^{t+\Delta t} D_{n,i+\frac{1}{2},B} B \left(\frac{\Psi_{n,i+1,B}^{t+\Delta t} - \Psi_{n,i,B}^{t+\Delta t}}{U_T} \right) \frac{b_{B-1}+b_B}{2a_i} \\
& + \frac{J_{th}+J_{tu}}{q} \frac{a_{i-1}+a_i}{2} \\
& + n_{i,B-1}^{t+\Delta t} D_{n,i,B-\frac{1}{2}} B \left(\frac{\Psi_{n,i,B-1}^{t+\Delta t} - \Psi_{n,i,B}^{t+\Delta t}}{U_T} \right) \frac{a_{i-1}+a_i}{2b_{B-1}} \\
& + n_{i-1,B}^{t+\Delta t} D_{n,i-\frac{1}{2},B} B \left(\frac{\Psi_{n,i-1,B}^{t+\Delta t} - \Psi_{n,i,B}^{t+\Delta t}}{U_T} \right) \frac{b_{B-1}+b_B}{2a_{i-1}} \Bigg] \\
\times \Bigg[& D_{n,i,B-\frac{1}{2}} B \left(\frac{\Psi_{n,i,B}^{t+\Delta t} - \Psi_{n,i,B-1}^{t+\Delta t}}{U_T} \right) \frac{a_{i-1}+a_i}{2b_{B-1}} \\
& + D_{n,i-\frac{1}{2},B} B \left(\frac{\Psi_{n,i,B}^{t+\Delta t} - \Psi_{n,i-1,B}^{t+\Delta t}}{U_T} \right) \frac{b_{B-1}+b_B}{2a_{i-1}} \\
& + D_{n,i+\frac{1}{2},B} B \left(\frac{\Psi_{n,i,B}^{t+\Delta t} - \Psi_{n,i+1,B}^{t+\Delta t}}{U_T} \right) \frac{b_{B-1}+b_B}{2a_i} \\
& + D_{n,i,B+\frac{1}{2}} \frac{1}{U_T} \frac{\Psi_{n,i,B+1}^{t+\Delta t} - \Psi_{n,i,B}^{t+\Delta t}}{b_B} \frac{a_{i-1}+a_i}{2} \\
& + \frac{A T^2}{n_0 q} \frac{a_{i-1}+a_i}{2} \\
& + \frac{1}{\Delta t} \frac{a_{i-1}+a_i}{2} \frac{b_{B-1}+b_B}{2} \Bigg]^{-1} . \qquad (4.44)
\end{aligned}
$$

For the negative electric field in the back drift current term we used $E_y = \frac{\Psi_{n,i,B+1}^{t+\Delta t} - \Psi_{n,i,B}^{t+\Delta t}}{b_B}$. Holes are only injected by the top contact, hence the hole equation (4.33) is adapted analogously for $j = 1$. For a more detailed description of the contact modelling the reader is referred to [27].

4.6 Boundary conditions

The simulated device cross section is depicted in Fig. 4.1. The top contact with coordinates $(i, 0)$ is coloured red, the bottom contact, defined by the indices $(i, B+1)$, is marked yellow. The ghost points, coloured grey, mark the left and right boundary of the simulated area. They have coordinates $(0, j)$ for the left column and $(A+1, j)$ for the right one.

There are two possibilities of considering the boundaries in x-direction in the simulation. The first one is to treat the simulated area as the whole device. In this case the potential at the ghost points is set equal to the potential at the neighbouring layer of the active area:

$$\psi_{0,j} = \psi_{1,j}\,, \quad \psi_{A+1,j} = \psi_{A,j}\,; \qquad \forall j \in [0, B+1].$$

Additionally the current flow across these boundaries must be zero as charge carriers can only enter and leave the device through the contacts. This can be ensured by choosing the diffusion constants in these points in the following way:

$$\begin{aligned} D_{n,0,j} &= -D_{n,1,j}\,, & D_{n,A+1,j} &= -D_{n,A,j}\,, \\ D_{p,0,j} &= -D_{p,1,j}\,, & D_{p,A+1,j} &= -D_{p,A,j}\,, \\ D_{ex,0,j} &= -D_{ex,1,j}\,, & D_{ex,A+1,j} &= -D_{ex,A,j}\,. \end{aligned}$$

A typical solar cell has an extenstion of about 100 nm in the y-direction but a few centimeters or even more in the x-direction. Considering this size ratio it seems reasonable to simulate a cell with dimensions (100×100) nm and employ periodic boundary conditions in x-direction. This is allowed as we can assume the solar cell to be fairly homogenous in the x-direction. The periodic boundary conditions are included in the simulation by setting

$$C_{0,j} = C_{A,j}\,, \quad C_{A+1,j} = C_{1,j}\,; \qquad \forall j \in [0, B+1]\,.$$

Here, C represents the electrostatic potential ψ, the HOMO level Θ_p, the LUMO level Θ_n, and the electron, hole, and exciton densities n, p, ex.

We additionally must consider the boundary conditions in y-direction. For the Poisson equation at the top contact we use

$$\psi_{i,0} = 0\,, \qquad \forall i \in [0, A+1]\,.$$

The condition at the bottom contact is given by

$$\psi_{i,B+1} = U_{ext} - V_{bi}\,, \qquad \forall i \in [0, A+1]\,,$$

where the externally applied voltage is denoted by U_{ext}. The built-in voltage is called V_{bi}. It is defined as the difference in workfunctions of both contacts:

$$V_{bi} = \Phi_{anode} - \Phi_{cathode}$$

The exciton density at the top and bottom contact must be set to zero, because of recombination processes (exciton quenching). We therefore define

$$ex_{i,0} = ex_{i,B+1} = 0\,, \qquad \forall i \in [0, A+1]\,.$$

For the continuity equations the boundary conditions for ohmic contacts are given by fixing the charge carrier densities at both contacts. We choose the following densities for top contact (=anode)

$$n_{i,0} = 10^{10} m^{-3}\,, \quad p_{i,0} = 10^{22} m^{-3}\,; \qquad \forall i \in [0, A+1]$$

and for the bottom contact (=cathode)

$$n_{i,B+1} = 10^{22} m^{-3}\,, \quad p_{i,B+1} = 10^{10} m^{-3}\,; \qquad \forall i \in [0, A+1]\,.$$

For the realistic contact modelling described in Section 4.5 the electron density at the top contact and the hole density at the bottom contact are set to

$$n_{i,0} = p_{i,B+1} = 10^{10} m^{-3}\,, \qquad \forall i \in [0, A+1]\,.$$

The electron density next to the bottom contact $n_{i,B}$ and the hole density next to the top contact $p_{i,1}$ are determined by equation (4.44) for electrons and an analogous equation for holes by fixing the current densities J_{th}, J_{tu} and J_{bf} at the interface between semiconductor and contact.

4.7 Iteration algorithm and initial conditions

Figure 4.3 shows the flowchart of the algorithm for finding a self-consistent solution of the coupled system of drift-diffusion and Poisson equations.

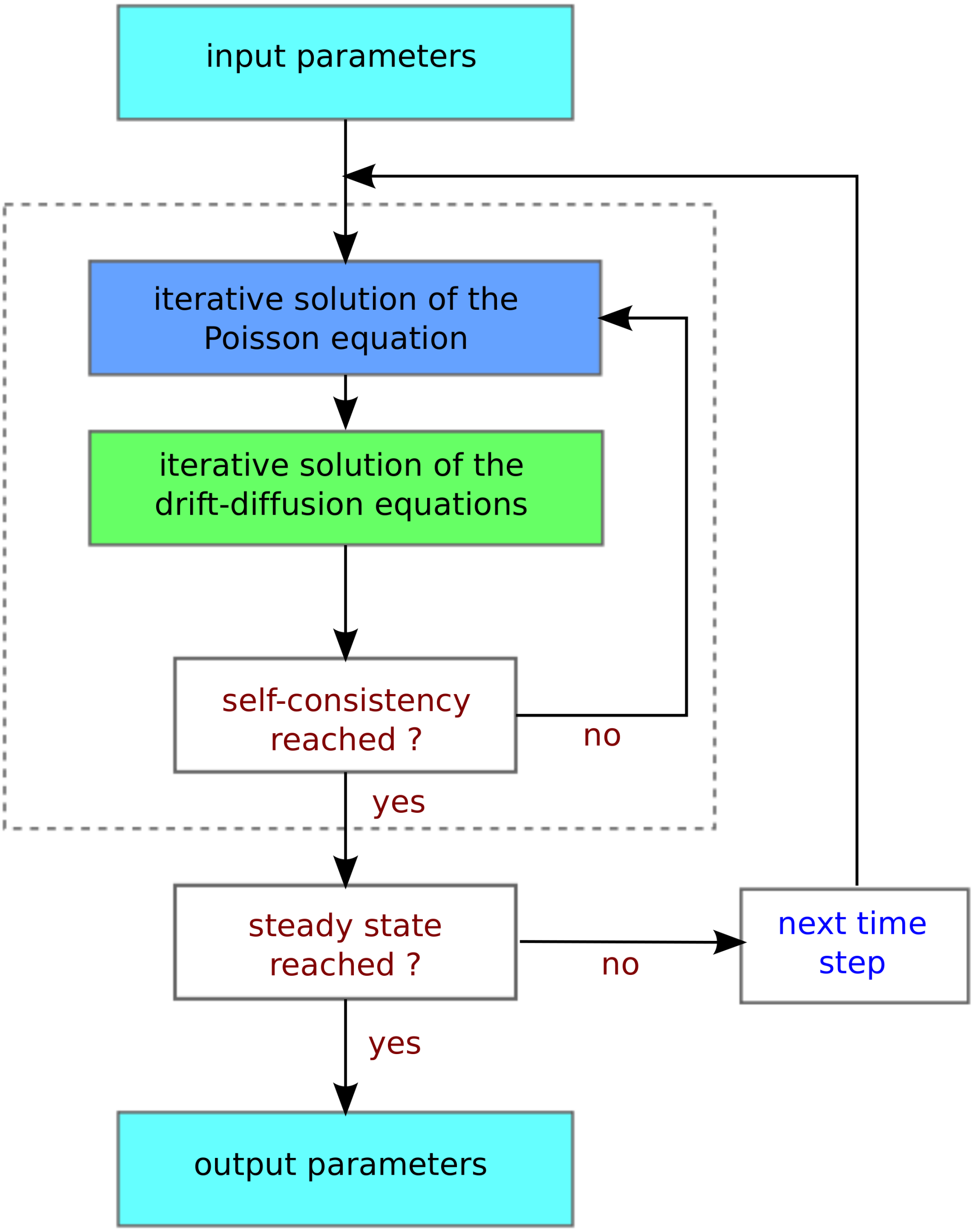

Figure 4.3: Flowchart of the simulation algorithm. The self consistent solution of the Poisson- and drift-diffusion equations performed at each time step is marked by the dashed line.

At the top, several input parameters must be handed over to the program. The necessary data includes the external applied voltage V_{ext} the HOMO and LUMO levels, the relative dielectric constants and the absorption coefficients of the donor and acceptor and the workfunctions of the contacts. Also required are the electron, hole and exciton mobilities, the incoming light spectrum and the ambient temperature. All these quantities are the input parameters of the program.

Before the simulation can be started initial conditions for the charge carrier densities and the potential have to be specified. We begin the simulation with no charge carriers or excitons present in the active layer. The electrostatic potential is zero all throughout the active layer. The workfunctions at the contacts are set at a fixed value. Summing up the initial conditions gives

$$n_{i,j}^{t=0} = p_{i,j}^{t=0} = ex_{i,j}^{t=0} = \psi_{i,j}^{t=0} = 0 \qquad \forall\, i \in [1, A],\, j \in [1, B]\,.$$

Before the iteration process is started the exciton distribution in the device is calculated. Excitons are generated without loss by light falling on the solar cell. The process is described in more detail in section 4.4. As the exciton generation rate is not influenced by the potential or the charge carrier densities we can calculate it up front and store the position dependent generation rate in a matrix. Then the iteration begins.

First a solution of the Poisson equation is found by the Poisson solver described in section 4.2. The potential is evaluated row-wise from left to right starting at position $(i = 1, j = 1)$. The so calculated potential distribution is plugged into the discretized drift-diffusion equations (4.32) and (4.33) for electrons and holes. The respective concentrations are calculated iteratively. The iteration process needs a starting configuration as an input parameter. We begin with vanishing charge carriers in the active area $n_{start,i,j} = p_{start,i,j} = 0$. Then the new charge carrier densities are calculated according to the current electric potential, row-wise from left to right starting at the top left grid point. This procedure is repeated over and over again always using the values of the previous runthrough as input. In our case the iterations for the potential and the electron and hole densities are performed alternately, because these quantities influence each other. This process is performed until self consistency is reached, yielding $\psi_{i,j}^t$, $n_{i,j}^t$, $p_{i,j}^t$. If this is the case the whole iteration is redone for the next time step, $t + \Delta t$. We exit the iteration if the change in the charge carrier densities and the potential from one time step to the next is smaller than a given threshold value. If this condition is fulfilled we assume to have reached the steady state.

In the following we can calculate interesting output data as the current density distribution or the total current running through the device. To obtain a whole I-V characteristic the whole simulation has to be done for a number of different applied voltages.

5 Simulation results

5.1 Model system

The following results were obtained by using the two-dimensional drift-diffusion equations described in Chapter 4. The simulation is based on the device layout shown in Fig. 5.1. All interfaces are planar. Thus a one-dimensional simulation is adequate. For this thesis a program for two-dimensional simulations was written. This enables the user to simulate different interface morphologies. The simulations done in the following all show planar interfaces. We therefore did not write a second code performing only one-dimensional simulations but used the 2D code reducing the number of grid points in x-direction to three including the ghost points. The grid-spacing in x-direction is equal. In y-direction it is not regular. Around the interfaces between the contacts and the adjoining semiconductor and the heterojunction the grid points in y-direction are set more closely than in the rest of the device. This allows us to plot the simulation results in 1D graphs, drawing the simulation results along the cross section shown as a red line in Fig. 5.1.

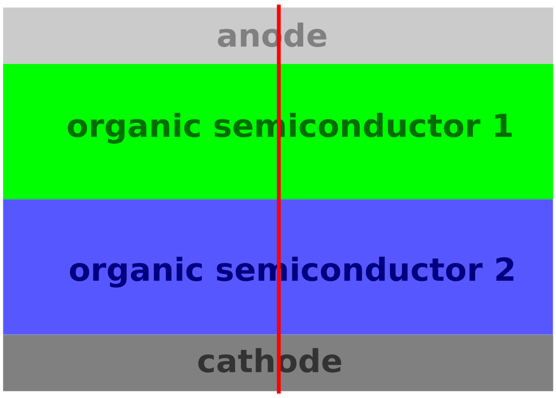

Figure 5.1: Schematic drawing of the device layout used for the 1D drift-diffusion simulations. All interfaces are planar.

At this point we want to introduce the reference system used in this work. All following simulations studying the influence of parameter variations will be compared to this reference case. The system parameters were chosen to represent a realistic system:

- Organic semiconductor 1: HOMO $= 5.4\,\mathrm{eV}$; LUMO $= 3.6\,\mathrm{eV}$

- Organic semiconductor 2: HOMO = 5.6 eV; LUMO = 4.1 eV
- Mobilities: $\mu_n = \mu_p = 10^{-8}\,\mathrm{m^2V^{-1}s^{-1}}$ for the entire device [14]
- Exciton diffusion constant: $D_{ex} = 2.25 \cdot 10^{-7}\,\mathrm{m^2s^{-1}}$
- Dielectric constants: $\varepsilon_{r,org1} = 3.5$ [39], $\varepsilon_{r,org2} = 4.4$ [40]
- Temperature: T= 300 K $\widehat{=}$ room temperature
- Potential at the real contacts: $\Phi_1 = 5.2\,\mathrm{V}$; $\Phi_2 = 4.3\,\mathrm{V} \rightarrow V_{bi} = 0.9\,\mathrm{V}$

The built-in voltage is defined as the difference in workfunctions $\Phi_{1/2}$ of the two contacts. It is denoted by V_{bi}. The electron and hole mobilities are denoted by μ_n and μ_p. The potential drop from the LUMO level of the acceptor to the cathode is the same as the potential drop from the HOMO level of the donor to the anode. Thus, electrons and holes encounter the same injection barrier from the contact into the semiconductor.

The simulation temperature of 300 K is of course not the average operating temperature of a solar cell, yet nearly all experiments are performed at this reference temperature. To enable comparisons with actual experiments, we choose the same ambient temperature for our simulations.

The contact modelling used in the reference system is described in Section 4.5. We also use it in most of the following simulations. In Section 5.2, simulation results obtained with this realistic contact modelling are compared with simulations using ohmic contact models.

The reference simulation already includes a reflective back contact as described in Chapter 4 and the use of wavelength-dependent absorption coefficients for both semiconductors, see Section 5.3. The absorption spectra of pentacene and C60 [28], see Fig. 5.8, were used for the donor and acceptor.

For the parameter studies treated in the following sections, only one of the simulation parameters is changed in each case. The used values are given at the beginning of the section. All not explicitly stated parameters have the same value as in the reference case.

The 1D plot of this reference simulation is depicted in Fig. 5.2. All simulation results are plotted at the maximum power point to enable comparisons between different simulations.

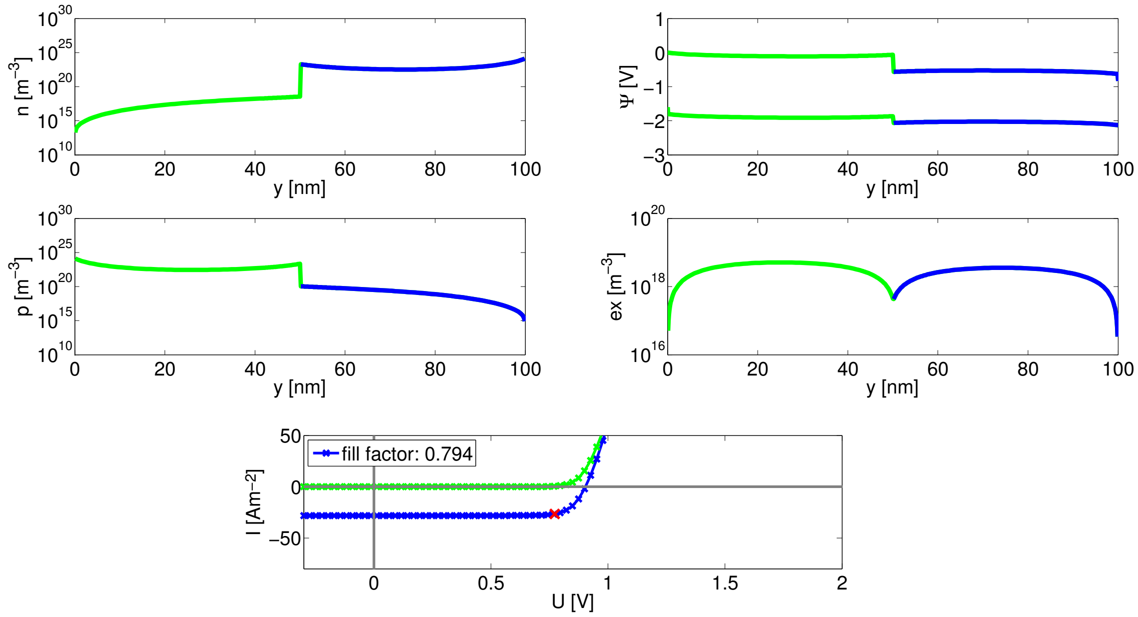

Figure 5.2: Simulation results for the reference system. Light first penetrates the top layer organic semiconductor (depicted by the areas coloured in green). The heterojunction to the second semiconductor (shown in blue) is clearly visible in all four subplots. The quantities drawn are the electron density n (top left), the hole density p (bottom left), the electrostatic potential Ψ (top right) and the exciton density ex (bottom right) and the current-voltage characteristic (bottom center). The I-V curve for the dark current is drawn in green, the illuminated current in blue. The simulated quantities shown in the top four panels are plotted for the illuminated case at the maximum power point. It is indicated as a red cross in the current-voltage characteristic.

After these preliminary considerations let us take a closer look at the simulation results shown in Fig. 5.2. The curves are coloured half in green and half in blue. This colour scheme is supposed to represent the two different organic semiconductors contained in the device, as illustrated in Fig. 5.1. Here the green area represents the electron donor, which is the hole conductor and the blue area the electron acceptor, which is the electron conductor.

In the top right panel of Fig. 5.2 we find the electrostatic potential Ψ separately for electrons and holes. The top curve gives the potential acting on electrons, the lower one on holes. At the heterojunction marked by the change in colour from green to blue, we find a potential jump in both curves, created by the offsets in the HOMO and LUMO levels of both semiconductors. In this case the offsets are not equal for HOMO and LUMO leading to differently sized potential jumps for electrons and holes.

Below the potential plot we find the panel depicting the exciton density ex. We see that it decreases quite significantly at the donor-acceptor interface. This is what one would expect. As already explained in Chapter 2 excitons are generated all through the device according to Lambert-Beer's law of absorption, yet they can only dissociate at a donor-acceptor interface. Thus, we see the clear decrease in the exciton density at the interface. Looking closely we also find that the exciton density slowly decreases from the top contact to the bottom contact. This is caused by the exponential character of light absorption. As this simulation already includes a reflective back electrode the effect is not very pronounced. A simulation showing this effect more clearly is depicted in Fig. 5.9 of Section 5.3.

The electron and hole densities n and p are plotted in the two panels on the left of Fig. 5.2. In both graphs a distinct jump in concentrations is found at the heterojunction. Electrons are found in much higher concentrations in the acceptor (blue area) and holes in the donor (green). In accord with the differently sized potential jump for electrons and holes the jump in the density is also larger for electrons than for holes. The reason for this correlation is that excitons dissociate into free electron-hole pairs at the interface. These free charge carriers are then literally sucked into either device half by the strong electric field acting at the interface. This field is generated by the potential jump at the interface. Thus, in this reference case the field acting on electrons is a bit stronger than the one acting on holes making the charge separation for electrons a little faster than for holes. This aspect will be discussed in more detail in Section 5.4.

A second interesting feature of the electron and hole density distributions is the behaviour towards the contacts. It can be clearly seen that the electron density rises distinctly towards the cathode (bottom contact) and the hole density towards the anode (top contact). This is caused by the realistic contact modelling used for the simulations as described in Section 4.5. The electrodes actively inject charge carriers into the semiconductor by thermionic emission and tunneling, thus increasing the charge carrier density in their vicinity. So the cathode raises the electron concentration and the anode the hole concentration. This form of contact modelling will be compared with ohmic contact modelling in Section 5.2.

Lastly we come to the current-voltage characteristics depicted in the bottom most panel of Fig. 5.2. We find two different curves, one in green and one in blue. Here these two colours do not represent the two device halves. The blue curve gives the I-V characteristic of the illuminated device, whereas the green curve shows the dark current. To better understand the simulation results it is useful to look at the transport level alignment of the system for different external voltages. Schematic illustrations plus a short description for distinct points on the I-V characteristic are given in the following.

At negative applied voltages the level alignment looks like in Fig. 5.3.

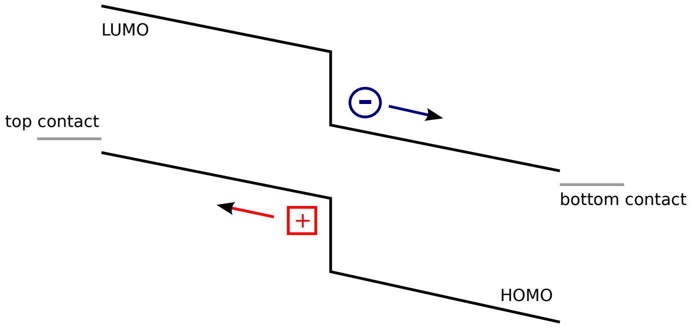

Figure 5.3: Energy level alignment in the device for negative applied voltages. The contact workfunctions are coloured grey, the HOMO and LUMO levels black. The workfunction of the top contact (on the left) is shifted above the workfunction of the bottom contact (right).

Current is flowing from the bottom contact to the top contact, meaning holes travel from bottom to top and electrons in the opposite direction.

At zero applied voltage we have the short circuit condition meaning the contacts are both at the same potential as shown in Fig. 5.4.

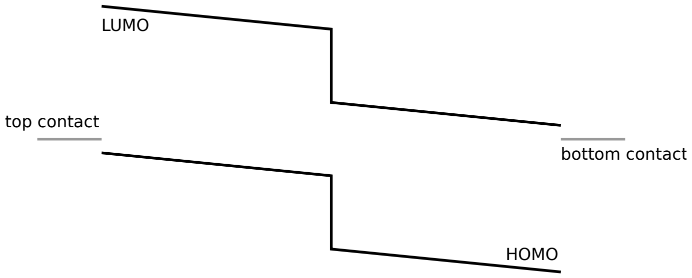

Figure 5.4: Energy level alignment in the device for zero applied voltages, called short circuit condition. The workfunctions of the contacts align at the same energy. The HOMO and LUMO levels are still tilted.

The current is still flowing from the bottom contact to the top contact.

Further increasing the externally applied voltage leads to the flat band condition, because the transport levels for electrons and holes are flat across the device as shown in Fig. 5.5.

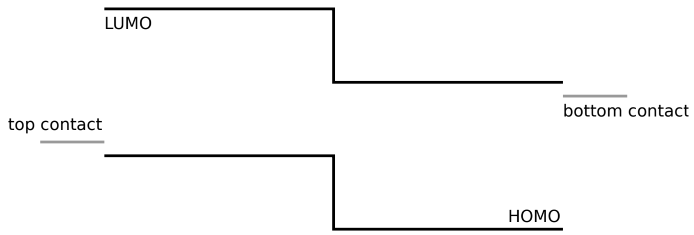

Figure 5.5: Energy level alignment in the device for flat band conditions. The applied external voltage exactly compensates the built-in voltage, so the HOMO and LUMO levels are completely flat in either half of the device. Charge carriers can only move diffusively, there is no drift force driving the charge carriers from the interface towards the contacts. The strong electric field at the interface is still present. It separates newly generated electrons and holes into the two semiconductors.

Under these conditions the charge carriers do not drift anymore from the interface towards the contacts. The strong electric field at the interface is still present. It separates newly generated electrons and holes into the two semiconductors. The only possible form of motion from the interface towards the contacts is diffusion. Electrons still mostly diffuse from the interface to the bottom contact and holes in the opposite direction from the interface to the top contact. Charge carriers will move away from densely populated areas. As free electrons and holes are generated solely at the heterojunction, they diffuse away from it towards their respective contacts. This charge carrier extraction due to diffusion only takes place in organic solar cells, see Section 2.2.

If the applied voltage is increased even further the potential landscape tilts in the other direction as plotted in Fig. 5.6.

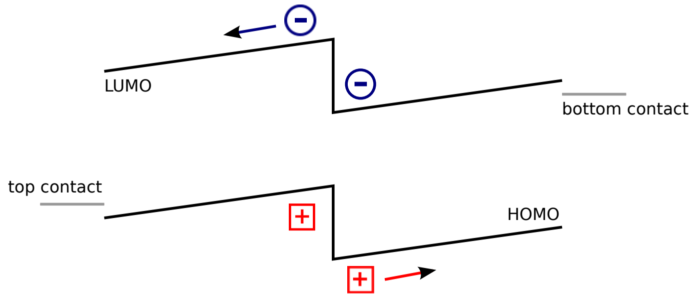

Figure 5.6: Energy level alignment in the device for applied voltages greater than the open circuit voltage. The transport levels are tilted in the other direction. Charge carriers drift towards the wrong contact. If the tilt is large enough they can overcome the potential barrier at the interface.

The open circuit voltage is approximately given by the formula [41, 42]

$$V_{oc} = V_{bi} + \min\{|\Delta\text{HOMO}|, |\Delta\text{LUMO}|\}$$

It is very important to note that for organic semiconductors the open circuit voltage is larger than the built-in voltage. If the external exactly compensates the built-in voltage, charge carriers still diffuse from the interface towards the current contacts, thus still resulting in negative current. The external voltage has to be increased even further to suppress this diffusion current. This case is depicted in Fig. 5.6. Caused by the tilt in the transport levels charge carrier drift towards the 'wrong' contacts sets in. For one, driven by photogenerated charge carriers drifting from the interface in the wrong direction. Secondly charge carriers are injected from the contacts into the semiconductors which additionally drift towards the opposite contact and thus also contribute to the unwanted positive current. In this process electrons are injected by the cathode and holes by the anode.

Here, the differences between organic and inorganic solar cells are very relevant and will be stated in the following.

- **Inorganic solar cells**
  In inorganic solar cells $\mathbf{V_{oc} = V_{bi}}$. This is the case for the following two reasons. Firstly, in inorganic semiconductors **diffusion plays a negligible part in the charge carrier extraction towards the contacts** as already explained in Chapter 2. Thus, we can only rely on drift forces driving the charge carriers out of the device. Now, if $V_{ext} = V_{bi}$, as shown in Fig. 5.5, which is the flat band condition, charge carriers are not subjected to any driving drift force and thus do not travel towards the contacts. So we find that in inorganic semiconductors there is no current flow in the flat band situation, thus the open circuit voltage equals the built-in voltage.

  Secondly, if there is any diffusion going on in the device it is neglibly small in inorganic semiconductors. Apart from that, electrons and holes both diffuse into the same direction, namely in the direction from the top contact to the bottom contact. Their two contributions to the current flow would cancel out as explained in more detail in Chapter 2.

- **Organic solar cells**
  Here $\mathbf{V_{oc} \geqslant V_{bi}}$. The open circuit voltage in this case is larger than the built-in voltage. In the flat band condition $V_{ext} = V_{bi}$ charge carriers are also not subjected to any drift force but they still diffuse from the interface, where they are generated towards the 'right' contact. This diffusion current is quite strong in organic semiconductors, because free charge carriers are only generated at the heterojunction and accumulate there. Thus, the gradient in the concentration as well as the electrostatic repulsion lead to charge carriers moving away from the interface towards their contact, because they can not overcome the potential barrier at the interface.

  The fact that charge carriers in organic solar cells can only be generated at the donor-acceptor interface has another significant impact. They tend to **accumulate at the heterojunction**, especially around the flat band condition. This accumulation of positive charges on one side of the interface and negative charges on the opposite creates a jump in potential that is superimposed to the potential drop already situated at the junction. However, this new potential drop is oriented in the opposite direction, thus **reducing the original potential drop** at the interface. The more charge carriers accumulate, the lower the energetic barrier gets until at a specific value, defined by the ambient temperature, charge carriers are able to thermally overcome the barrier. This effect plays a crucial role in the behaviour of organic solar cells, see Sections 5.6 and 5.8.

Coming now back to Fig. 5.2, we can easily describe the two characteristics. The dark current (green) is solely created by charge carrier injection from the contacts into the device. This only sets in at an applied voltage of $V_{oc} \approx 0.9\,\mathrm{V}$. At this point the energy level alignment already looks like in Fig. 5.6. Electrons are injected by the cathode and travel towards the anode and vice versa for holes. The external voltage is large enough to enable them to overcome the potential barrier at the interface. This results in a positive current. The blue curve of Fig. 5.2 shows the characteristic of an illuminated solar cell. The current stays at a certain negative value over a long voltage range before it rises more or less sharply towards zero and positive values. The current remains at the same value because only a certain number of charge carriers are generated per time unit, according to the incoming light intensity. All charge carriers are extracted to the contacts by the built-in voltage. If the external voltage is negative it even increases the electric field extracting the charge carriers. If V_{ext} is positive it reduces the built-in field, but the electric field is still strong enough to extract nearly all charge carriers. Therefore, the current remains at one value for such a long time. The abrupt rise shortly before V_{oc} is caused by charge carriers diffusing and drifting towards the 'wrong' contact, eventually making the current positive. In the illuminated case there are two contributions. For one, charge carriers are injected by the contacts and travel towards the respective opposite contact. This is the contribution of the dark current. Secondly, the free charge carriers created at the interface also drift towards the 'wrong' contact, thus increasing the unwanted positive current even more. As the external voltage is increased this unwanted positive current quickly compensates the fastly decreasing negative current until it gets too strong and the overall I-V characteristic reaches positive current values. With this explanation in mind it is clear that the open circuit voltage V_{oc} of the illuminated characteristic is strongly bound to the onset voltage V_{onset} of the dark current. Once the dark current sets in the photocurrent quickly gets overcompensated.

5.2 Contacts

In our program ohmic contacts are modeled considering two features:

- They have the same workfunction as the respective HOMO/LUMO level of the adjoining semiconductor, here meaning the HOMO-level for the hole or top contact and the LUMO-level for the electron or bottom contact.

- Their charge carrier densities are held at a fixed value. We choose the hole concentration at the top contact to be the same as the electron concentration at the bottom contact. They both have the value $p_{top} = n_{bottom} = 10^{22}\,\mathrm{m}^{-3}$.

The simulation results for ohmic contacts are shown in Fig. 5.7, the ones for real contacts in Fig. 5.2 of Section 5.1.

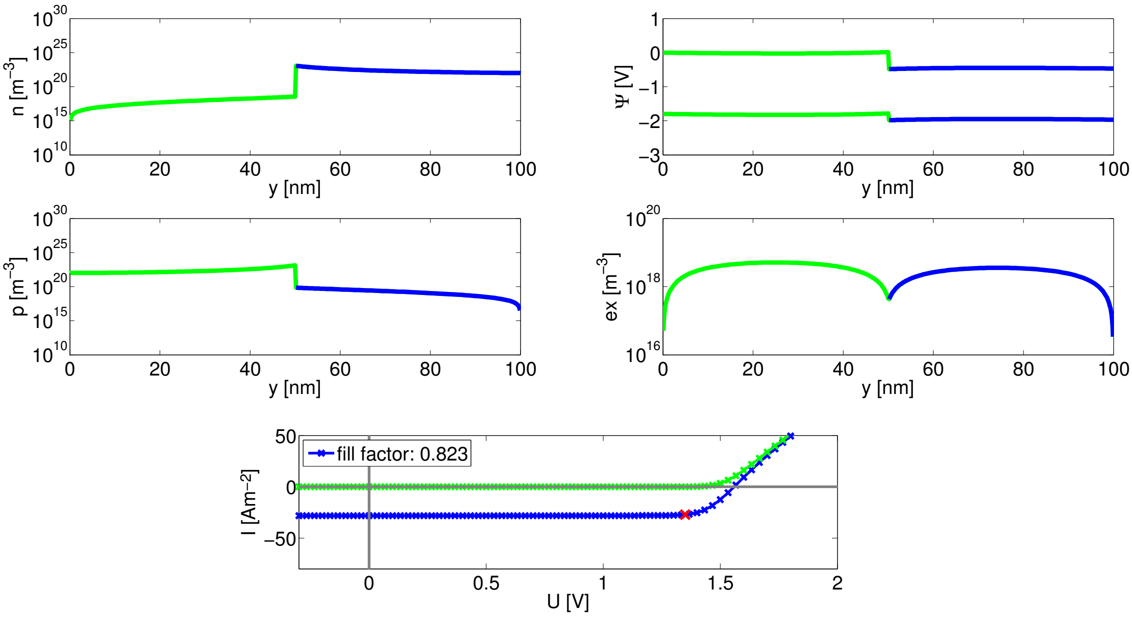

Figure 5.7: Simulation results for the model system described in Section **??** combined with ohmic contacts. The electron and hole densities n, p (left side) as well as the electrostatic potential Ψ (top right), the exciton density ex (in the middle on the right side) and the current-voltage characteristic (bottom) are shown.

For ohmic contacts the open circuit voltage is larger than the built-in voltage. The reason for this behaviour could be charges still diffusing to 'their' contact. Furthermore the I-V curve bends more sharply and abruptly in the case of real contacts. That also increases the fill factor in the case of ohmic contacts a little bit.

Next we consider the electron distribution corresponding to the point of maximum power shown in the upper left panels of Fig. 5.2 and 5.7. The maximum electron density for ohmic contacts occurs right at the organic-organic interface reaching a value of $n_{max} \approx 1.4 \cdot 10^{24} m^{-3}$. Roughly the same value holds for holes. The charge carrier densities at the interface are of the same magnitude for realistic contacts. This is immediately plausible, because the contact modelling does not influence the interface. One noticeable difference is the charge carrier density in proximity to the contacts. In the case of realistic contacts it bends up towards the contact, that is the electron density rises towards the bottom contact and the hole density towards the top contact. This does not happen when ohmic contacts are used. The difference is about three orders of magnitude adjacent to the contact, so it can be called a significant impact. This is due to the active injection of charge carriers into the semiconductor at reals contacts.

The potential distribution has fairly the same shape in both cases except that there obviously is a difference in the built-in voltage, determined by the workfunctions of the contacts. These parameters are fixed at the start of the simulation.

The exciton distribution is also the same in both cases which is very reasonable, because the exciton generation and dissociation does not happen at and is not influenced by the contacts.

All following simulations are done with the more realistic contact modelling.

5.3 Reflection and absorption

5.3.1 Reflection condition at the bottom contact

We now want to look at the impact of a reflective bottom contact on the performance of the solar cell. In the simulation, it is assumed that the light travels on a straight path from the top electrode to the bottom electrode where it gets reflected at an angle of 0° and goes back the same way. Along its path through the device, light is absorbed by the semiconductor according to the Lambert-Beer law of absorption (4.39). In this case α is taken from an absorption measurement [28]. We used the absorption coefficients of pentacene and C60 as a function of wavelength for our simulations. The according spectra are plotted in Fig. 5.8.

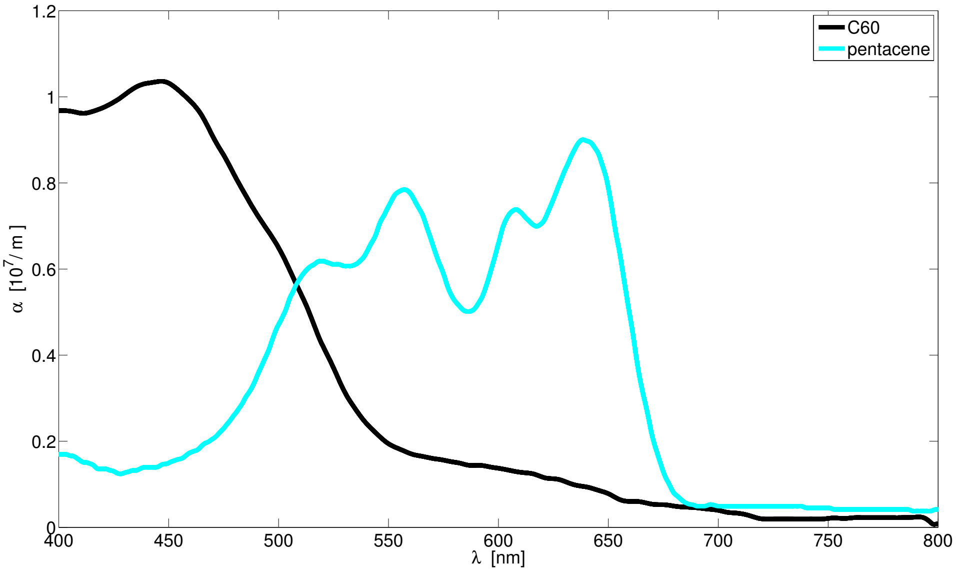

Figure 5.8: Absorption coefficients of pentacene and C60 in dependence of wavelength [28].

We used the absorption coefficient of pentacene for the topmost semiconductor layer and the one of C60 for the second semiconductor layer. Light diffusion and refraction are not taken into account.

Figure 5.9 shows the simulation without reflection at the bottom contact. The plot of the reference case, including a reflecting back electrode can be found in Fig. 5.2 of Section 5.1.

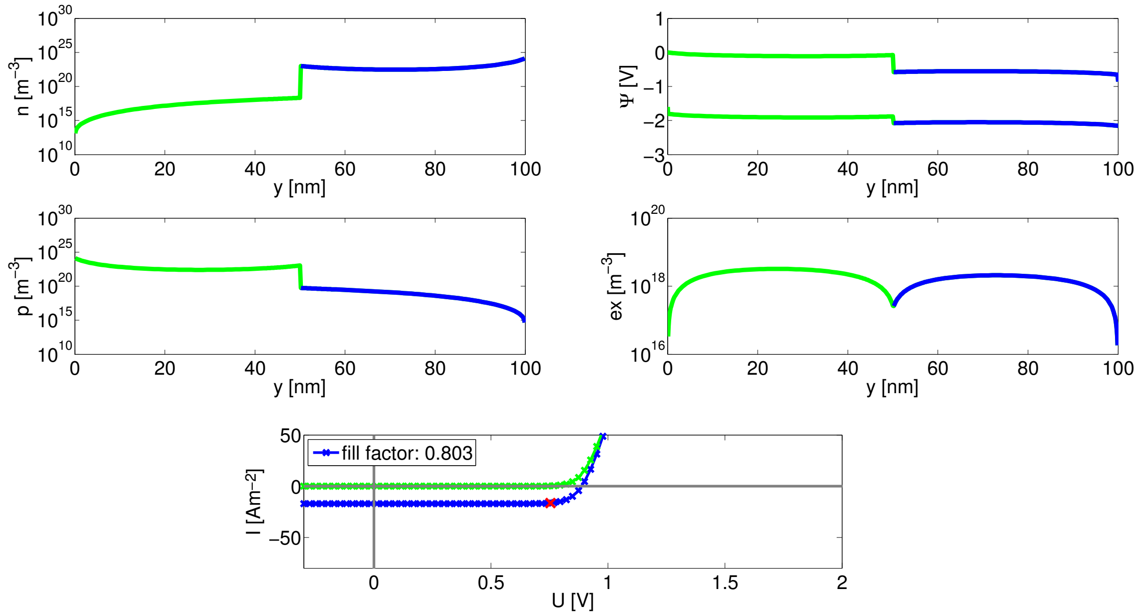

Figure 5.9: Simulation results for the model system without light being reflected at the bottom contact. Light travels on a straigt path from the top electrode to the bottom electrode.

We see a significant increase in the short circuit current from $I_{sc} \approx -17\,\mathrm{Am}^{-2}$ to $I_{sc} \approx -28\,\mathrm{Am}^{-2}$. This is very reasonable because the light passes the device twice and generates many more excitons which in turn dissociate at the interface, leading to higher current values. Looking closely one can also notice the change in the exciton distribution. Without reflection at the bottom contact more excitons are generated in the top half of the device than in the bottom half. This is very plausible as less light intensity reaches the second half. But if the light is reflected back again it first passes the second polymer thereby generating excitons. So on its way back the light has still more intensity in the bottom half than in the top half of the device, there producing more excitons as the absorption coefficients of both materials are approximately the same. Thus, combining both influences the exciton density is approximately equal in both device halves, yet it is generally a little elevated compared to the simulation without light reflection.

5.3.2 Influence of the absorption coefficient on the simulation results

The program was improved by going from absorption coefficients chosen for each material to implementing measured absorption coefficients including their wavelength dependence. These coefficients were calculated from absorption measurements, [28], and are plotted in Fig. 5.8. The absorption spectra of pentacene and C60 were used to represent the two organic semiconductors. Pentacene is a hole conductor (represented by the green area in Fig. 5.1) and C60 an electron conductor (blue area in Fig. 5.1). The reference simulation described in Section 5.1 includes the given spectra plus a reflective back electrode.

Before implementing actual absorption spectra in the program test simulations with fixed values for the absorption coefficients of the two semiconductors α_{org1} and α_{org2} were performed. A simulation done with the specific values $\alpha_{org1} = 1 \cdot 10^7\,\mathrm{m}^{-1}$ for the top semiconductor layer and $\alpha_{org2} = 5 \cdot 10^6\,\mathrm{m}^{-1}$ for the bottom semiconductor layer is shown in Fig. 5.10. The simulation includes light reflection at the back electrode.

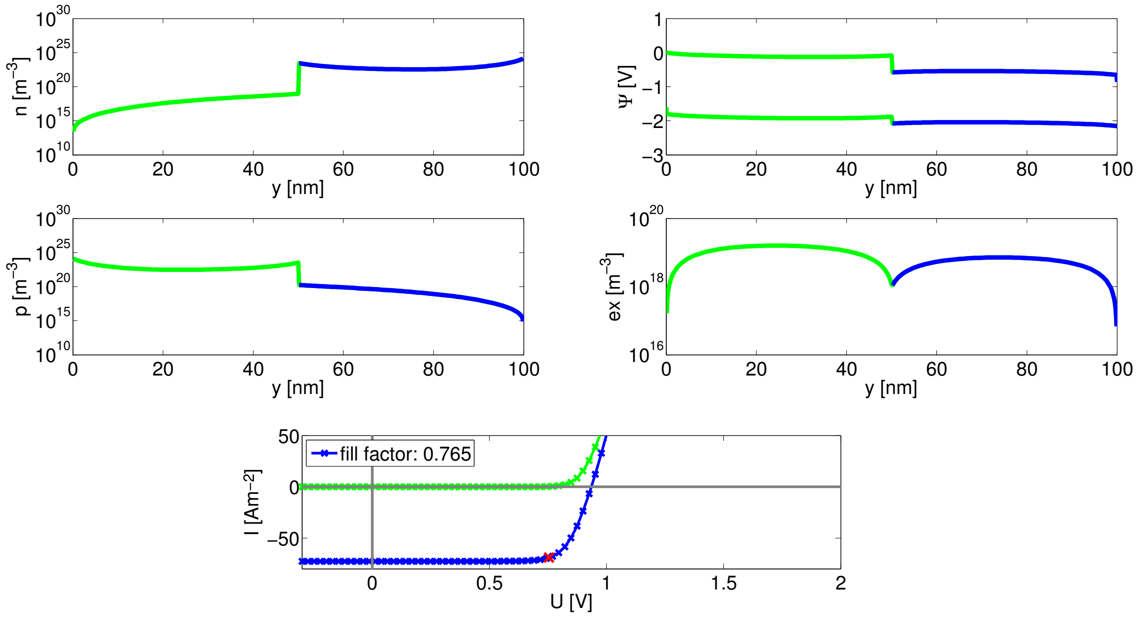

Figure 5.10: Simulation results for the model system with the absorption coefficients chosen as $\alpha_{org1} = 1 \cdot 10^7\,\mathrm{m}^{-1}$, $\alpha_{org2} = 5 \cdot 10^6\,\mathrm{m}^{-1}$. Light reflection at the back contact is included.

We notice at once that with these α values the short circuit current is very high compared to the reference case (figure 5.2). The open circuit voltage is unchanged as one would strongly expect, the contact modelling being the same in both simulations.

The exciton distribution, however, shows a difference. Firstly, it is generally higher throughout the device in the case of fixed absorption coefficients. We have chosen both α values higher than in the α spectra. Secondly we see a higher concentration of excitons in the top semiconductor (represented in green in Fig. 5.1), which can be expected, knowing the used absorption coefficients. They occur in Lambert-Beer's law (4.39) with a minus sign in an exponential factor $e^{-\alpha \cdot d}$. Consequently, the larger α the more light is absorbed. In our case this means that the first semiconductor layer (green) which has a higher α-value absorbs more light than the second semiconductor and therefore, more excitons are generated in the top device half.

In the case of equal absorption coefficients for both materials, see Fig. 5.11, we see a marginally higher exciton concentration in the bottom layer of the device than in the top layer.

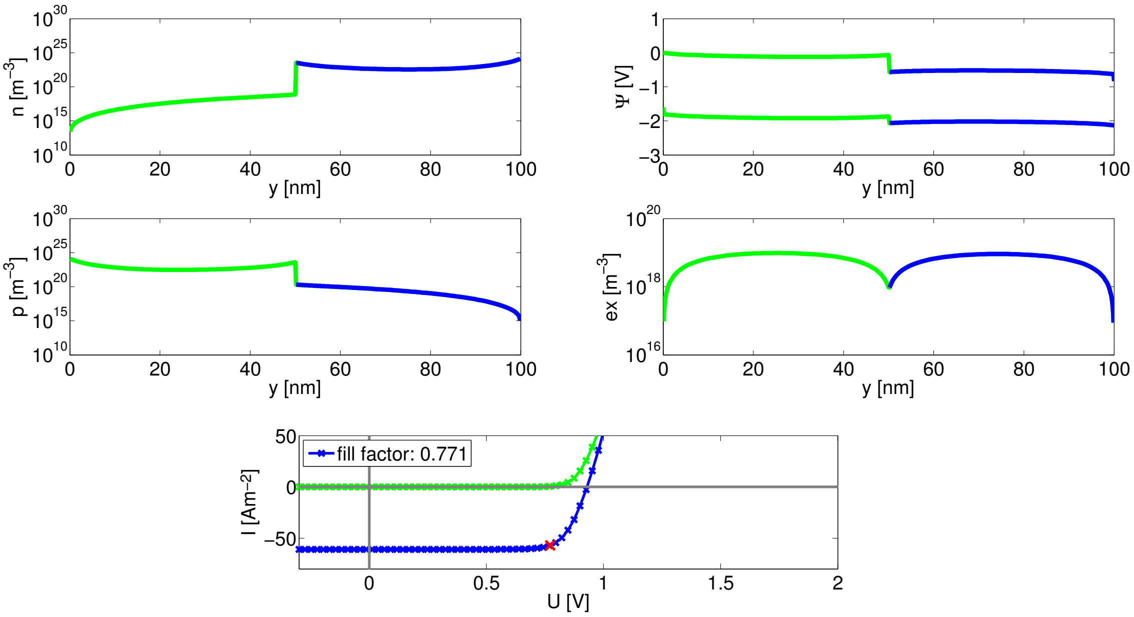

Figure 5.11: Simulation results for the model system with equal absorption coefficients for both semiconductors: $\alpha_{org1} = \alpha_{org2} = 5 \cdot 10^6\,\mathrm{m}^{-1}$. Light reflection at the back contact is included.

Light enters the solar cell through the top contact and gets absorbed steadily on its way through the device. When it reaches the second semiconductor its intensity has already decreased due to absorption, therefore less excitons are generated in the second semiconductor than in the first. The difference in exciton density can be reduced by introducing a reflective back contact as was done in the previous section, or by choosing a lower α value for the first semiconductor than for the second. In the case of equal absorption coefficients for both semiconductors and reflection at the backside of the solar cell the exciton concentration is approximately the same in both device halves, as can be seen in Fig. 5.11. So apparently, reflection off the back contact has a profound impact on the exciton generation. A lot of intensity reaches the back contact and is now used again for absorption and not neglected in the simulation. The short circuit current is a little lower than in the case of $\alpha_{org1} = 1 \cdot 10^7\,\mathrm{m}^{-1}$, $\alpha_{org2} = 5 \cdot 10^6\,\mathrm{m}^{-1}$, see Fig. 5.10, because the overall absorption is reduced as the first absorption coefficient $\alpha_{org1} = 5 \cdot 10^6\,\mathrm{m}^{-1}$ used for the simulation shown in figure 5.11 is smaller than for 5.10.

We did another test by swapping the absorption coefficients from Fig. 5.10 and simulating again, now with the configuration $\alpha_{org1} = 5 \cdot 10^6\,\mathrm{m}^{-1}$ and $\alpha_{org2} = 1 \cdot 10^7\,\mathrm{m}^{-1}$. The simulation results are shown in Fig. 5.12.

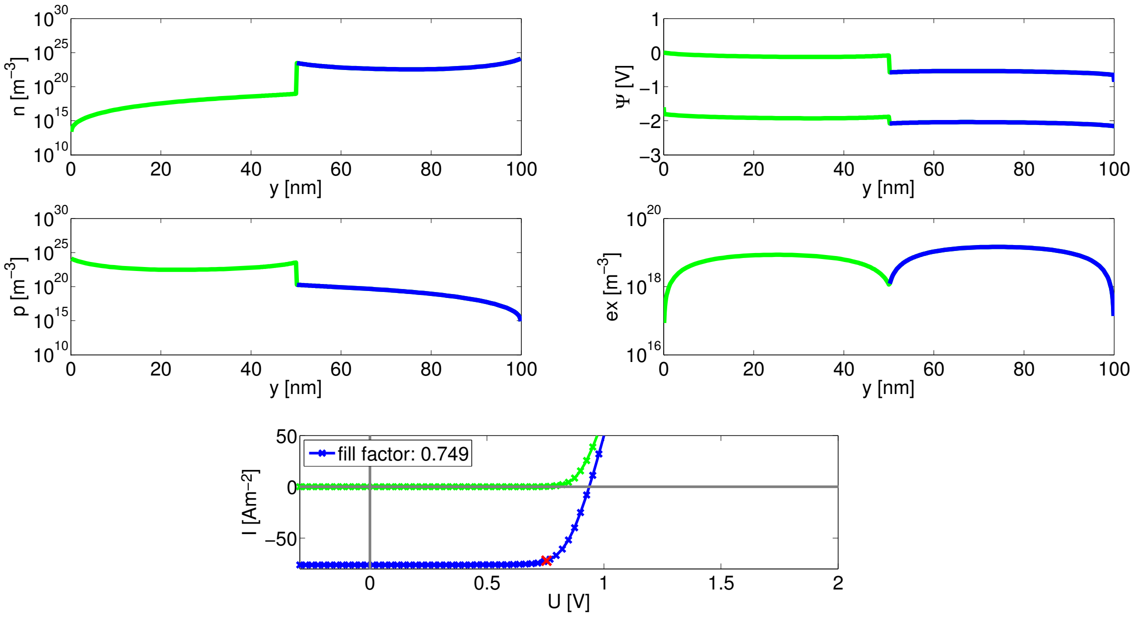

Figure 5.12: Simulation results for the model system with the absorption coefficients chosen as $\alpha_{org1} = 5 \cdot 10^6\,\mathrm{m}^{-1}, \alpha_{org2} = 1 \cdot 10^7\,\mathrm{m}^{-1}$. Light reflection at the back contact is included.

In the I-V curve we see only a slight difference in the short circuit current compared to Fig. 5.10 and this tiny shift can be explained by the different exciton distributions. The open circuit voltage remains once again unchanged. Now we come to the exciton density. We see that the swap in absorption coefficients makes the exciton density in the second semiconductor even higher than in the first.

All following simulations are performed using the absorption spectra in Fig. 5.8.

5.4 Charge separation at the organic-organic interface after exciton dissociation

In the simulations, exciton dissociation is implemented in such a way that all excitons, which reach the organic-organic interface by diffusion, dissociate instantaneously into an electron-hole pair. The exciton is thus separated into two independent and no longer electrically neutral charge carriers. As already described in Chapter 4, an exciton dissociating in the row above the interface, characterized by the coordinates $(i, \frac{B}{2})$, leaves a hole and an electron at the same position $(i, \frac{B}{2})$. The same goes for the row beneath the interface, denoted by coordinates $(i, \frac{B}{2}+1)$. They newly generated free electrons and holes react to the strong electric field present at the interface and are literally sucked into their respective transport layers, that is the top layer (green) for holes and the bottom layer (blue) for electrons. The according simulation results are shown in Fig. 5.2 of Section 5.1.

A test simulation was done to show the efficiency, with which the electron-hole pairs are separated by the electric field into the two semiconductors. When an exciton reaches the interface we mean it reaches the row above the interface, denoted by coordinates $(i, \frac{B}{2})$, or the row below, denoted by coordinates $(i, \frac{B}{2}+1)$. The interface is situated between those two rows. So if an interface reaches "the interface" in this test simulation a hole is instantaneously generated in the last row of the hole conductor, characterized by the coordinates $(i, \frac{B}{2})$, and an electron in the top row of the electron conductor, characterized by the coordinates $(i, \frac{B}{2}+1)$. The results are shown in Fig. 5.13.

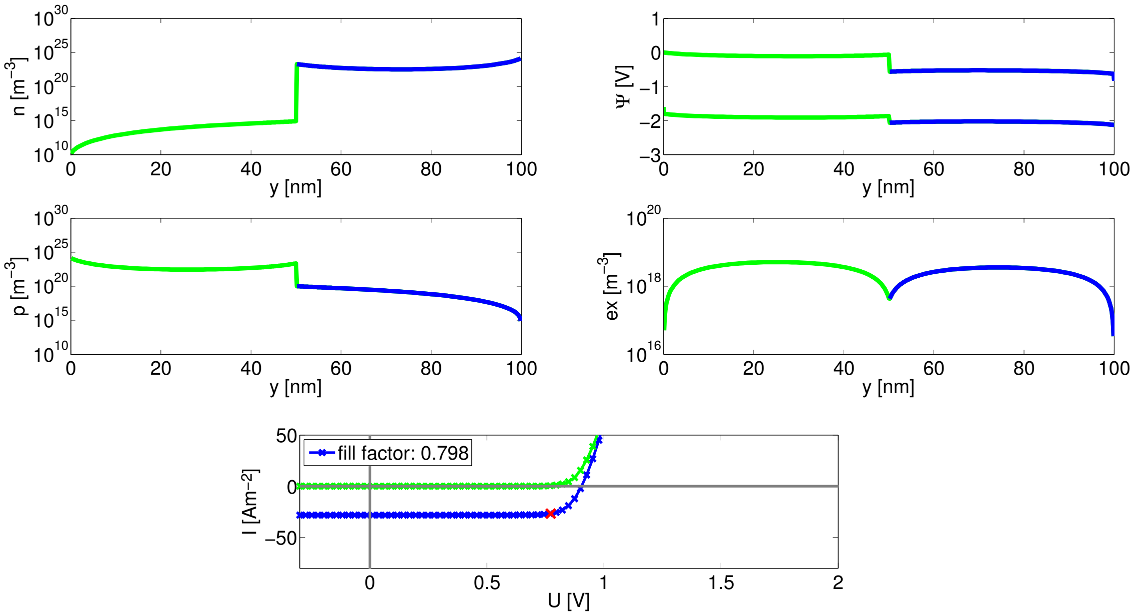

Figure 5.13: Simulation results for the model system with fixed charge separation at the interface. If an exciton dissociates at the interface a hole is instantaneously generated in the last row of the top layer and an electron in the top row of the bottom layer.

We find a difference in the electron and hole densities between the two figures 5.2 and 5.13. It is caused by electrons and holes generated in the wrong layer and recombining there before they are moved into the 'right' semiconductor. The electric field indeed separates the charges very effectively as can be seen by comparing the I-V curves of figures 5.2 and 5.13, which are almost identical.

We notice that the electron density in the hole conductor (green) in the test case, see Fig. 5.13 top left panel, is lower than in the reference case, see Fig. 5.2. However, there is no influence on the I-V curve. This is reasonable as the electron/hole densities in the respective other conductor are very low anyway. So if there are a little less or more 'wrong' charge carriers in each semiconductor it does not influence the I-V characteristic noticeably. This shows that the charge separation by the electric field following each exciton dissociation is very effective. Far less charge carriers are lost due to recombination at the interface as would be necessary to influence the I-V characteristic.

For the following simulations, we only use the model of charge separation by the electric field. It is physically more intuitive than the strict separation. And as the exact nature of the exciton dissociation and charge separation at the interface are not yet understood in detail, our way of modeling is a reasonable first choice.

5.5 Mobility

All simulations were done with the system parameters according to the model system described in Section 5.1. Only the charge carrier mobilities in both organic semiconductors were varied and are stated for every simulation. The reference simulation is shown in Fig. 5.2.

1) The first change in mobility was taken in a way we hoped would improve the performance of the solar cell. The values chosen were:

Organic semiconductor 1 (top half): $\mu_n = 10^{-8}\,\mathrm{m^2V^{-1}s^{-1}}$; $\mu_p = 10^{-6}\,\mathrm{m^2V^{-1}s^{-1}}$.
Organic semiconductor 2 (bottom half): $\mu_n = 10^{-6}\,\mathrm{m^2V^{-1}s^{-1}}$; $\mu_p = 10^{-8}\,\mathrm{m^2V^{-1}s^{-1}}$.

The charge carriers have higher mobilities in the device halves adjoining their collective contact, meaning holes move faster in the top half of the device and electrons in the bottom half. The according simulation results are shown in Fig. 5.14.

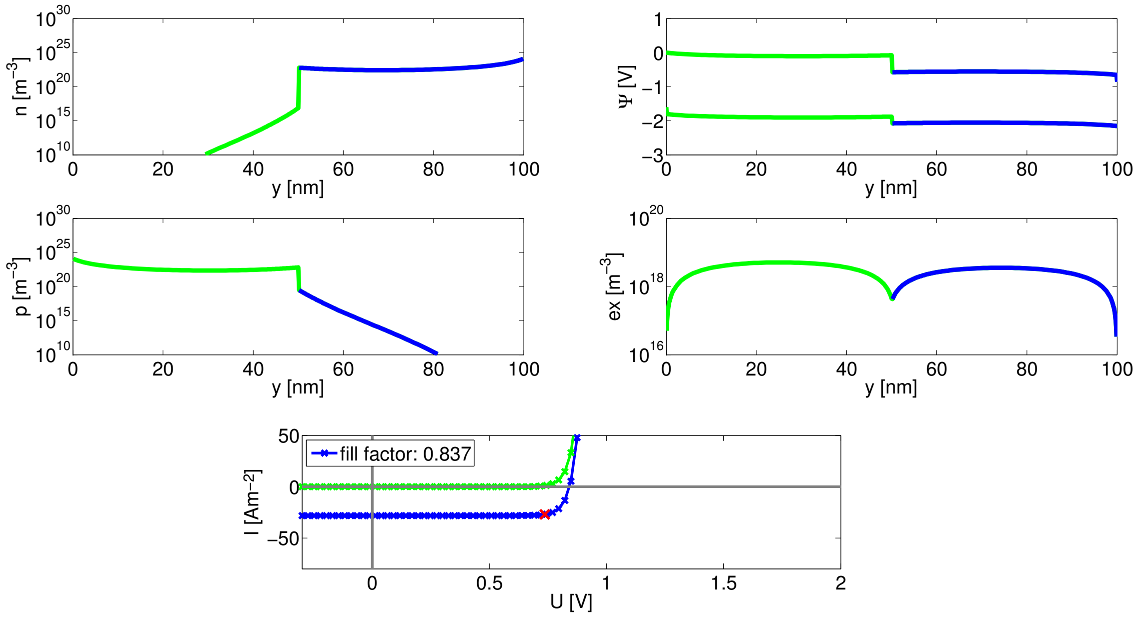

Figure 5.14: Simulation results for the model system with different electron and hole mobilities in the two semiconductors:
top half: $\mu_n = 10^{-8}\,\mathrm{m^2V^{-1}s^{-1}}$; $\mu_p = 10^{-6}\,\mathrm{m^2V^{-1}s^{-1}}$,
bottom half: $\mu_n = 10^{-6}\,\mathrm{m^2V^{-1}s^{-1}}$; $\mu_p = 10^{-8}\,\mathrm{m^2V^{-1}s^{-1}}$.

We only see a slight influence on the shape of the I-V curve. The slope near the open circuit voltage is a bit steeper in case 1) than in the reference case. This is caused by the increase in the mobility on one half of the device per charge carrier.

We expect no influence on the short circuit current, which indeed is the case as is clearly observable in Fig. 5.2 and 5.14. Indeed, how fast the charge carriers move has no influence on how many excitons are generated or on how efficiently they dissociate at the interface. Therefore, the short circuit current is not influenced significantly by the charge carrier mobility.

Now we have a look at the electron and hole distributions in the device, depicted in the panels of the left of Fig. 5.14. We see that the charge carrier density on the respective opposite half of the device is dramatically lower in case 1) than in the reference case. This is caused by low mobility in these regions for one type of charge carrier. Most of them recombine before they can travel far. In the reference simulation we detect a slight accumulation of charges at the interface. This does not happen in case 1) because electrons and holes diffuse away faster from the interface driven by the gradient in charge carrier density.

We do not see an impact on the potential landscape and the exciton distribution. The potential distribution should be slightly influenced by the charge accumulation at the interface. The gathering of positive and negative charges at either side of the organic-organic interface creates an electric field which superimposes the electric field created by the potential drop at the interface. So the potential difference at the interface should be reduced a little bit. This can indeed be seen if the charge

accumulation is more pronounced as will be shown later in Fig. 5.27 and 5.30 of Sections 5.10 and 5.11. Here the effect is too small to see it on the chosen scale of the plot.
2) In the next case we increase the mobilities still further by one order of magnitude in the favoured halves:

Organic semiconductor 1 (top half): $\mu_n = 10^{-8}\,\mathrm{m^2V^{-1}s^{-1}}$; $\mu_p = 10^{-5}\,\mathrm{m^2V^{-1}s^{-1}}$.
Organic semiconductor 2 (bottom half): $\mu_n = 10^{-5}\,\mathrm{m^2V^{-1}s^{-1}}$; $\mu_p = 10^{-8}\,\mathrm{m^2V^{-1}s^{-1}}$.

The simulation results are shown in Fig. 5.15.

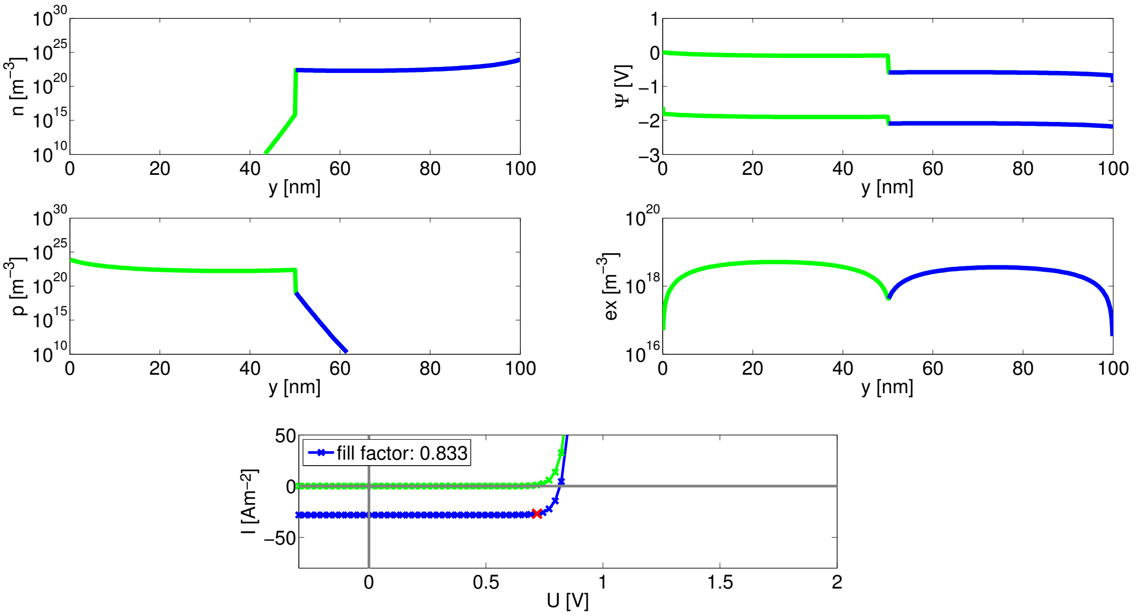

Figure 5.15: Simulation results for the model system with different electron and hole mobilities in the two semiconductors:
top half: $\mu_n = 10^{-8}\,\mathrm{m^2V^{-1}s^{-1}}$; $\mu_p = 10^{-5}\,\mathrm{m^2V^{-1}s^{-1}}$,
bottom half: $\mu_n = 10^{-5}\,\mathrm{m^2V^{-1}s^{-1}}$; $\mu_p = 10^{-8}\,\mathrm{m^2V^{-1}s^{-1}}$.

We expect the same trends as in case 1) but more distinctive. This is indeed observed for the I-V curves as well as the electron and hole densities.
3) To also study the opposite case we did a simulation with "reversed" mobilities, i.e. the following choice of parameter was used:

Organic semiconductor 1 (top half): $\mu_n = 10^{-6}\,\mathrm{m^2V^{-1}s^{-1}}$; $\mu_p = 10^{-8}\,\mathrm{m^2V^{-1}s^{-1}}$.
Organic semiconductor 2 (bottom half): $\mu_n = 10^{-8}\,\mathrm{m^2V^{-1}s^{-1}}$; $\mu_p = 10^{-6}\,\mathrm{m^2V^{-1}s^{-1}}$.

These mobility settings mean that electrons move faster in the device half adjoining the hole collecting top contact than in the other half of the device. The same holds for holes only vice versa. This simulation is expected to show the opposite effects of case 1). The simulation results are shown in Fig. 5.16.

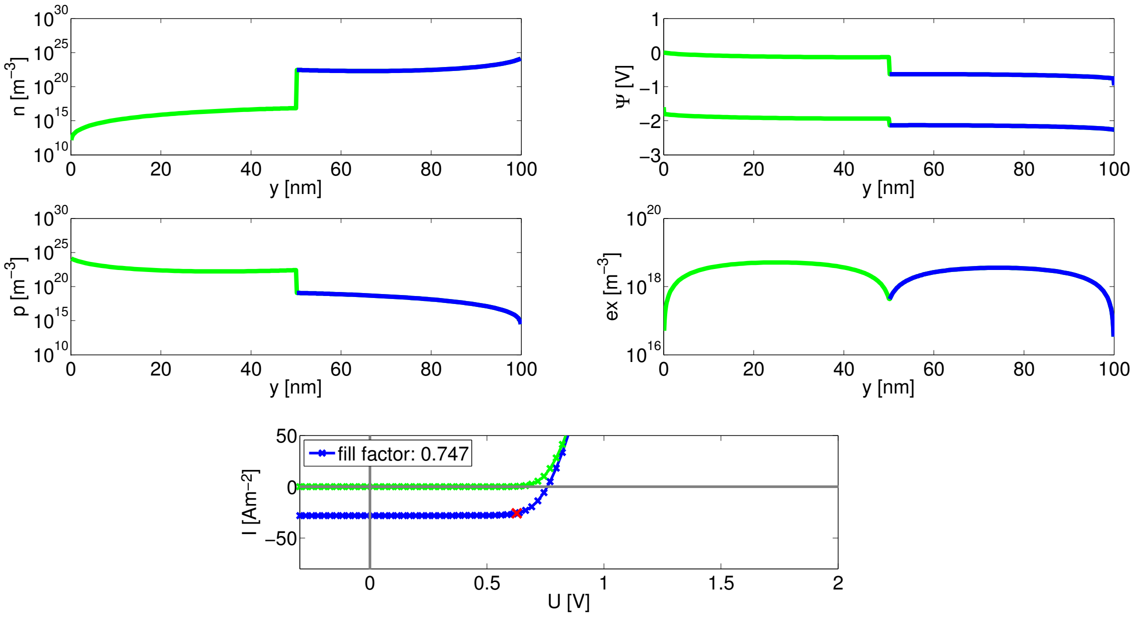

Figure 5.16: Simulation results for the model system with different electron and hole mobilities in the two semiconductors:
top half: $\mu_n = 10^{-6}\,\mathrm{m^2V^{-1}s^{-1}}$; $\mu_p = 10^{-8}\,\mathrm{m^2V^{-1}s^{-1}}$,
bottom half: $\mu_n = 10^{-8}\,\mathrm{m^2V^{-1}s^{-1}}$; $\mu_p = 10^{-6}\,\mathrm{m^2V^{-1}s^{-1}}$.

As expected, we indeed see a drop in fill factor from case 1) to case 3). We also expect higher charge carrier densities on the ”wrong” halves of the device, which can really be observed in Fig. 5.16.

5.6 Temperature dependence of the model system

In the reference case, shown in Fig. 5.2, we see only a slight accumulation of charges at the organic-organic interface, as already described in more detail in Section 5.1. It takes the charge carriers a certain time, defined by temperature, mobility and the gradient in the charge carrier density, to diffuse and drift away from the interface, where they are generated.

We now look at a simulation done for the same system parameters, but at an ambient temperature of T = 400 K, plotted in Fig. 5.17.

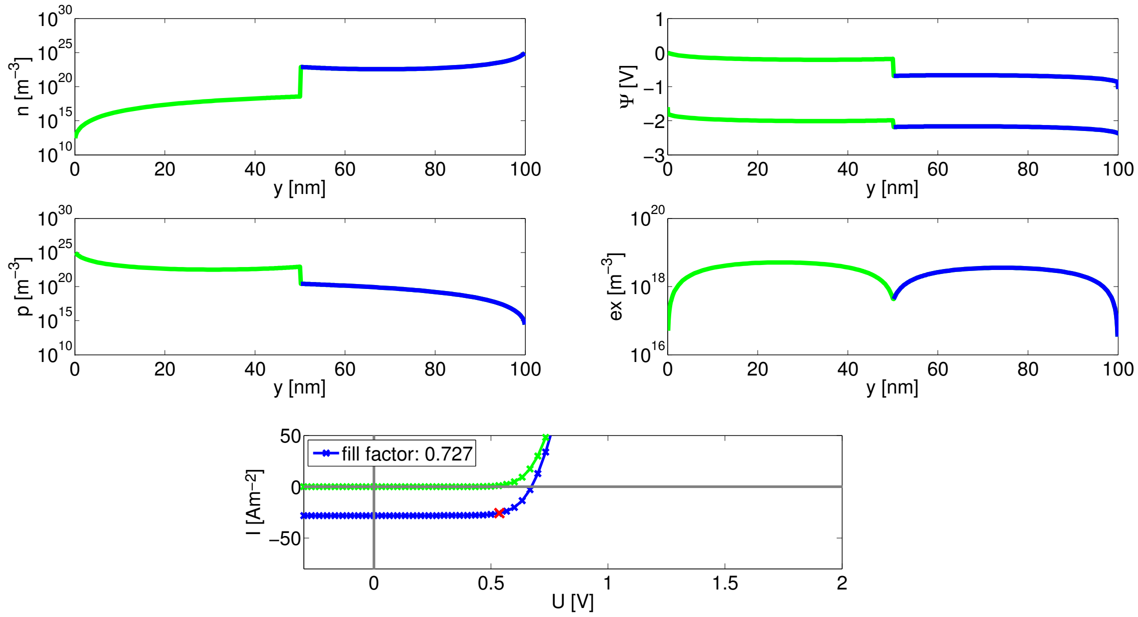

Figure 5.17: Simulation results for the model system described in Section 5.1 simulated at an ambient temperature of T = 400 K. Depicted are the electron and hole densities n and p (left column), the electrostatic potential Ψ (top right), the exciton density ex (middle right) and the current-voltage characteristic (bottom) for the illuminated (blue) and dark (green) case.

At first inspection of the I-V curve, we see a noticeable decrease in the open circuit voltage as well as in the onset of the dark current. They are both correlated, as one would expect. The change in V_{oc} is caused by the fact that the charge carrier motion is of course temperature dependent, see equations (4.32) and (4.33). The charge carriers have a higher thermal energy allowing them to overcome energy barriers as the one posed by the organic-organic interface more easily. Their large thermal energy allows electrons and holes to cross the interface at a lower applied external voltage than at lower ambient temperatures.

A second effect plays a role. The jump in the potential at the interface is reduced by charges accumulating at either side of the interface. At higher temperatures, fewer carriers have needed to accumulate to lower the barrier sufficiently to allow charge carriers to cross it. Therefore, the dark current sets in earlier. We can see that at T = 400 K the electron and hole densities bend up less at the interface than in the simulation for T = 300 K, see Fig. 5.2.

The short circuit current is not influenced by the temperature. The fill factor decreases from $FF = 0.79$ for T = 300 K to $FF = 0.75$ for T = 400 K.

We now look at the case of an ambient temperature of T = 200 K. The according simulation results are shown in Fig. 5.18.

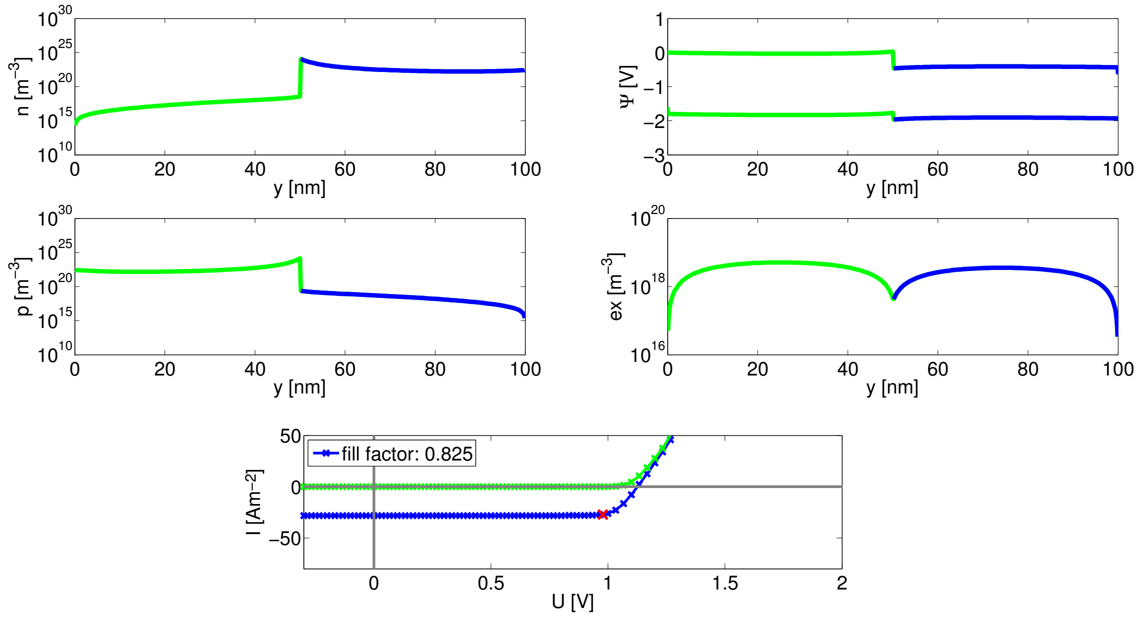

Figure 5.18: Results for the model system described above simulated at an ambient temperature of T = 200 K.

This simulation shows, as already suggested by the results of the simulation for T = 400 K, a significantly increased open circuit voltage of $V_{oc} \approx 1.14\,\mathrm{V}$, again corresponding with the onset of the dark current. The short circuit current I_{sc} is not affected. We see a clear increase in the fill factor from $FF = 0.79$ for T = 300 K to $FF = 0.83$ for T = 200 K.

Now considering the electron and hole densities we find that both types of charge carriers strongly accumulate at the interface, thereby diminishing the energy barrier located there. The potential barrier reaches the low point of $\Delta\Psi = 0.2\,\mathrm{V}$ for holes. The dark current of course sets in as soon as one type of charge carrier is able to overcome its potential barrier at the interface and drift towards the opposite contact.

These observations correspond very well to the simulation done at a temperature of T = 400 K. Indeed they show the exact opposite effect, as one would expect, thereby further corroborating the explanation put forward.

5.7 Real system ITO/PEN/C60/Al

We now move on to have a look at the simulation results of the more realistic system ITO/PEN/C60/Al. The energy levels are given in Tab. **??**, [32]:

Table 5.1: Energy levels of the system ITO/PEN/C60/Al

top contact	indium-tin-oxide (ITO)	$\Phi = 4.8\,\mathrm{eV}$
electron donor	pentacene (PEN)	HOMO=4.9eV, LUMO=3.0eV
electron acceptor	(C60)	HOMO=5.8eV, LUMO=4.1eV
bottom contact	aluminum (Al)	$\Phi = 4.2\,\mathrm{eV}$

However, one always has to take into account that the actual energy levels in a device can be quite different from the levels in a single material. When bringing two different materials in contact with each other, various effects can happen at interface, such as formation of an interface dipole layer, which can shift the transport levels considerably [35, 36, 37]. This explains the variety of values given in the literature. We therefore are not bound to one specific value but can vary them a little bit.

The simulation of this system posed considerable convergence problems. The difficulties result from the large offsets in the HOMO and LUMO levels. We resolved the situation by updating the electron and hole concentrations per simulation step, n^k, p^k more slowly. The applied technique is called mixing:

$$\begin{aligned} n^k_{new} &= \sigma n^{k-1} + (1-\sigma) n^k_{old}\,, \\ p^k_{new} &= \sigma p^{k-1} + (1-\sigma) p^k_{old}\,. \end{aligned}$$

We achieved good convergence with the choice $\sigma = 0.8$, although the simulations naturally took longer times to finish.

For this system, we again consider a planar junction between the two organic semiconductors, each of which is 50 nm thick (as in the model system). Non-ohmic contacts, reflection at the aluminum contact and real absorption spectra of pentacene and C60 are included in the simulation. The mobilities were chosen to be equal for electrons and holes in the entire device: $\mu_n = \mu_p = 10^{-8}\,\mathrm{m^2V^{-1}s^{-1}}$.

The results of the reference simulation performed at an ambient temperature of $\mathrm{T} = 300\,\mathrm{K}$ are depicted in Fig. 5.19.

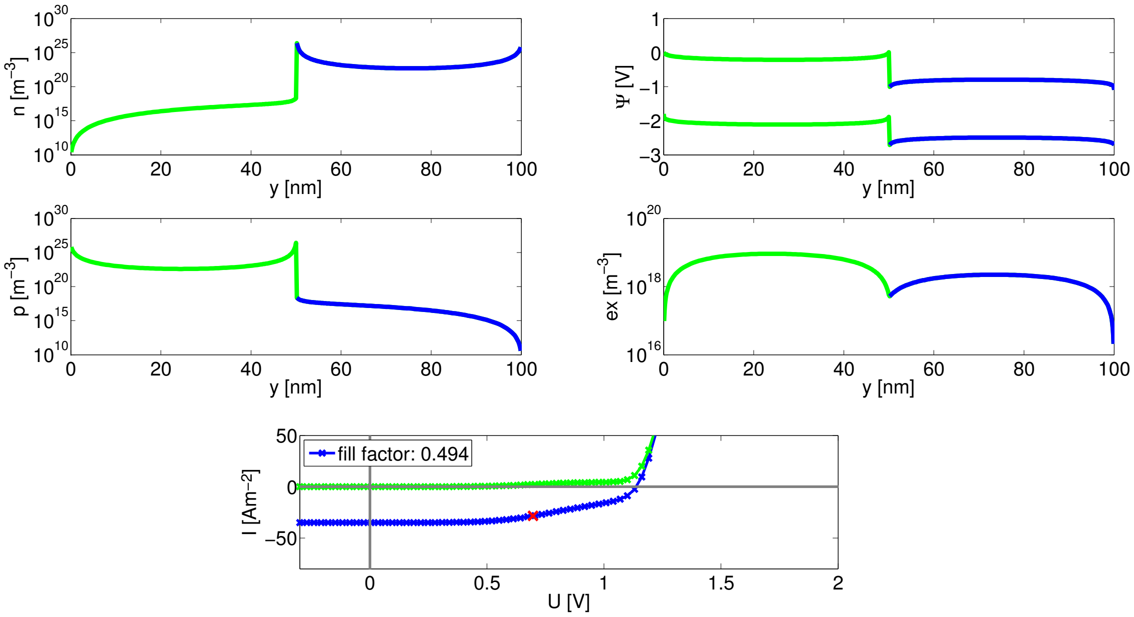

Figure 5.19: Simulation results for the system ITO/PEN/C60/Al calculated at a temperature of T = 300 K.

We find an unexpected looking I-V curve. The current is zero at a voltage of $V_{oc} \approx 1.14\,\mathrm{V}$, but there is already a distinct kink at about $V_{ext} \approx 0.6\,\mathrm{V}$, which corresponds to the built-in voltage, which is given by the difference of the workfunctions of the contacts $V_{bi} = \Phi_1 - \Phi_2 = (4.8 - 4.2)\,\mathrm{V} = 0.6\,\mathrm{V}$.

In our simulations we saw a difference between the I-V curves of layouts with different energy level alignments:

1. $\mathbf{V_{bi}} > \min\{|\mathbf{\Delta}\mathrm{HOMO}|, |\mathbf{\Delta}\mathrm{LUMO}|\}$
2. $\mathbf{V_{bi}} < \min\{|\mathbf{\Delta}\mathrm{HOMO}|, |\mathbf{\Delta}\mathrm{LUMO}|\}$

1) In the first case the I-V curves look as discussed earlier in the reference case of the model system, see Fig. 5.2 of Section 5.1. The current stays at the value of the short circuit current for a long time until a steep ascent begins shortly before V_{oc}. No s-shapes or kinks are observed.

2) In the second case of energy level alignments we always observe a kink in the illuminated current as well as in the dark current at $V_{ext} = V_{bi}$. A typical simulation result is shown in Fig. 5.19. This simulation will be used as a reference case for all further simulations of the system ITO/PEN/C60/Al.

The above mentioned kink is was always found as long as the condition **2)** holds. Simulations with various level offsets have been performed. The HOMO and LUMO levels of the semiconductors as well as the workfunctions have been modified always resulting in the same qualitative shape of the I-V curve. So it seems reasonable to propose that the kink in the characteristic is not restricted to one special device layout or due to a certain coincidence. It seems to be a common feature of devices with energy landscapes according to the condition **2)**. *Kumar et al.* also observed such a kink in the I-V characteristic of organic solar cells [34]. They attribute this behaviour to strong interface dipoles. We will consider this explanation also in Sections 5.9 to 5.11 and show that both the a potential drop at the interface can be introduced into the system by directly shifting the HOMO/LUMO levels of the donor and acceptor, or by inserting a dipole layer at the interface.

Here we attempt to give an **explanation** for this unexpected shape of the current-voltage characterstic. For this purpose we consider again the transport band alignment at different external voltages of in Fig. 5.3 to 5.6 of Section 5.1.

If $V_{bi} < \min\{|\Delta\mathrm{HOMO}|, |\Delta\mathrm{LUMO}|\}$, then a certain number of charge carriers can already cross the potential barrier at $V_{ext} = V_{bi}$. The probability of such an event is very small. If $V_{ext} = V_{bi} + \min\{|\Delta\mathrm{HOMO}|, |\Delta\mathrm{LUMO}|\}$, all charge carriers of one type injected by the contact can cross the interface, because the potential energy they have at their starting point, the contact, equals the potential energy of the jump at the interface, see Fig. 5.6. Charge carriers injected by the contacts, reaching the opposite electrode compose the dark current. Between V_{bi} and V_{oc}, the illuminated current also rises with a nearly constant slope before rather abruptly changing the slope at V_{oc}. The continuous increase in current between $V_{ext} = V_{bi}$ and $V_{ext} = V_{oc}$ implies that more and more charge carriers travel in the unwanted direction through the device. The probability of crossing the energy barrier at the interface gets larger with higher applied voltage. The increase in the illuminated current from $V_{ext} = V_{bi}$ onwards is more pronounced than the rise in the dark current. This is the case because the illuminated current is composed of the photocurrent plus the dark current, so we have to take into account both kinds. The dark current has already been mentioned above. The photocurrent is generated by charge carriers created at the interface, which move towards the contacts. In this discussed case they drift towards the 'wrong' contact, electrons to the anode and holes to the cathode, meaning that also the photocurrent slowly reverses its direction. These two contributions together, photo + dark current, explain why the illuminated current rises more distinctly than the dark current.

Coming back to the reference simulation, we take a look at the electron and hole densities depicted in the two panels on the left of Fig. 5.19. Electrons and holes accumulate very strongly on either side of the organic-organic interface. The maximum electron density is $n_{max} \approx 10^{27}\,\mathrm{m}^{-1}$ and the maximum hole density is $p_{max} \approx 10^{27}\,\mathrm{m}^{-1}$. They both occur at the interface. The charge carrier densities are also bent upwards at the contact regions, because of the non-ohmic contact simulation. The extreme charge gathering at the interface even bends up the potential in that region, on top of reducing the potential jump.

The potential jump, to be found in the top right panel of Fig. 5.19, in the electron transport level is larger than in the hole transport level. The height is determined by the HOMO and LUMO levels in the two semiconductors. In this case $|\Delta\mathrm{LUMO}| > |\Delta\mathrm{HOMO}|$.

5.8 Temperature dependence of the system ITO/PEN/C60/Al

Now we come to the temperature dependence of the system ITO/PEN/C60/Al. The results of the reference case for all following simulations of this system is depicted in Fig. 5.19 of Section 5.7.

We first look at the changes caused by a higher temperature of T = 400 K. The according simulation curves are depicted in Fig. 5.20.

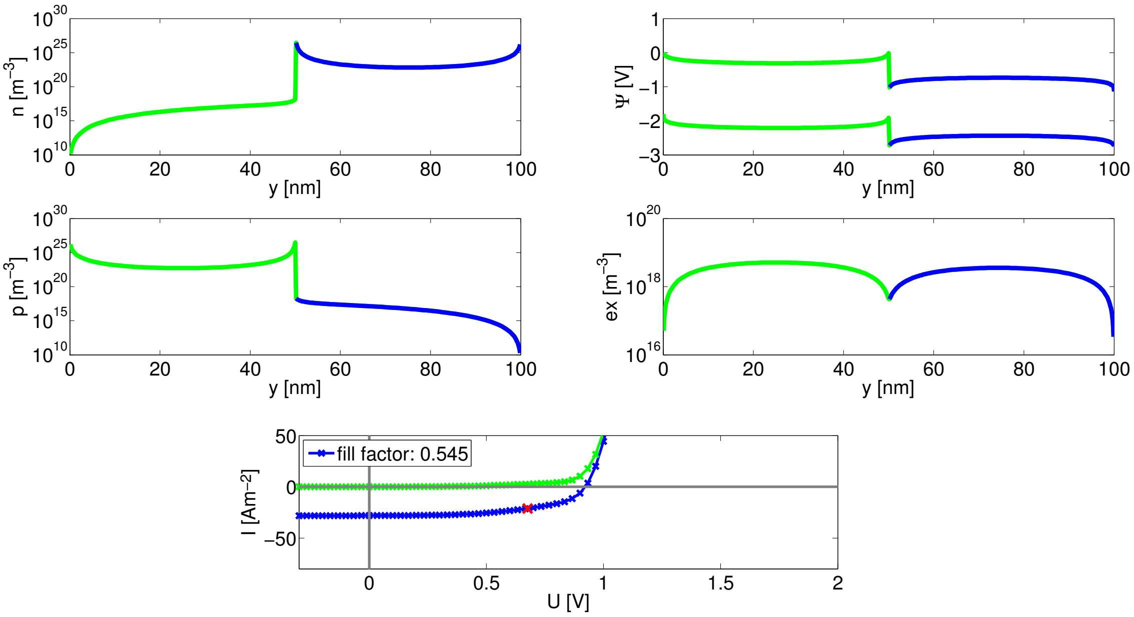

Figure 5.20: Simulation results for the system ITO/PEN/C60/Al calculated at a temperature of T = 400 K.

We notice that the open circuit voltage has dropped to $V_{oc} \approx 0.9\,\mathrm{V}$. The change in slope, or kink, at $V_{ext} = V_{bi} = 0.6\,\mathrm{V}$ is still visible, but not as distinctively as at lower temperature. The dark current also still rises a little bit at $V_{ext} = V_{bi} = 0.6\,\mathrm{V}$.

The lowering in the open circuit voltage is not surprising and can be explained by the fact that the charge carriers can cross higher energy barriers due to their raised thermal energy, see equations (4.32) and (4.33). This effect was also seen in the model system, as was the described change in the potential distribution (see Section 5.6). The explanation is again given by the increase in thermal energy.

We now have a look at the simulation results for an ambient temperature of T = 200 K, shown in Fig. 5.21.

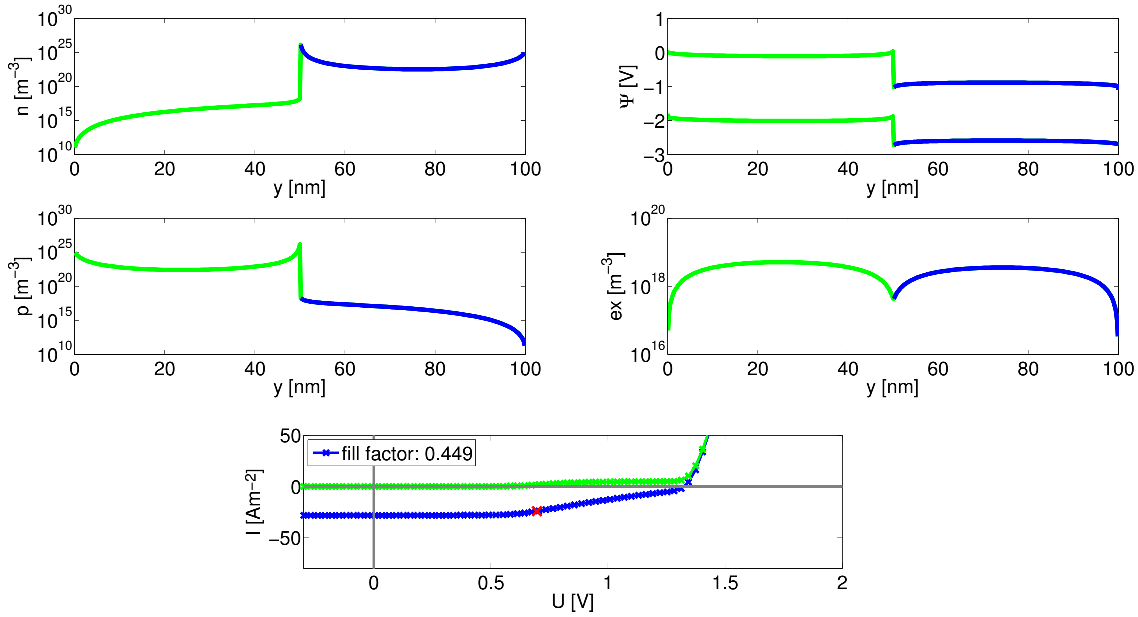

Figure 5.21: Simulation results for the system ITO/PEN/C60/Al calculated at a temperature of T = 200 K.

The open circuit voltage has increased compared to the results for T = 300 K. It is now $V_{oc} \approx 1.33\,\mathrm{V}$. The kink is still there and even more distinctive. The changes in slope are more abrupt than in the other two cases. The dark current shows the expected rise at $V_{ext} = V_{bi}$ and the sharp bend at $V_{ext} \approx 1.33\,\mathrm{V}$.

The potential distribution also has the expected shape. The height of the barrier in the HOMO level at V_{oc} is reduced to $\Delta\Psi \approx 0.3\,\mathrm{V}$. The explanation is analogous as for T = 400 K, except that the charge carriers have of course lower thermal energy. Therefore, more charge carriers need to accumulate at the interface to reduce it to even lower levels as for T = 400 K to enable the charge carriers to cross it.

5.9 Influence of a shift in the vacuum energy level on the solar cell performance

By inserting a dipole layer at the organic-organic interface, as schematically shown in Fig. 5.22, a shift ΔE_{vac} of the vacuum energy level is induced [33].

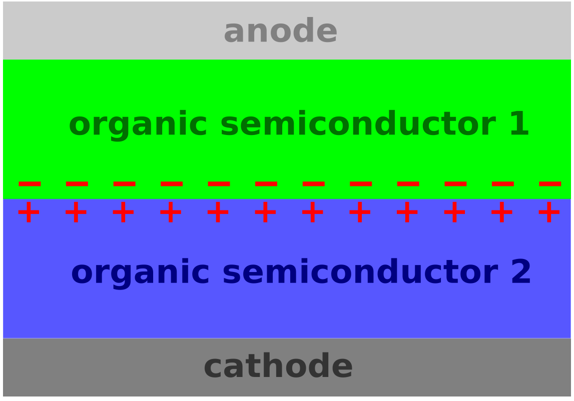

Figure 5.22: Schematic illustration of a planar heterojunction solar cell with a dipole layer situated at the organic-organic interface.

Whether the vacuum energy level is raised or lowered is determined by the orientation of the dipole layer. Figure 5.23 shows an illustration of an energy landscape representative of the ones simulated in this work. The vacuum energy level E_{vac} is taken as a reference point. All other energies are measured with respect to E_{vac}. The positive energy axis is directed downwards. Lines drawn lower than E_{vac} in the following graphics represent positive energies.

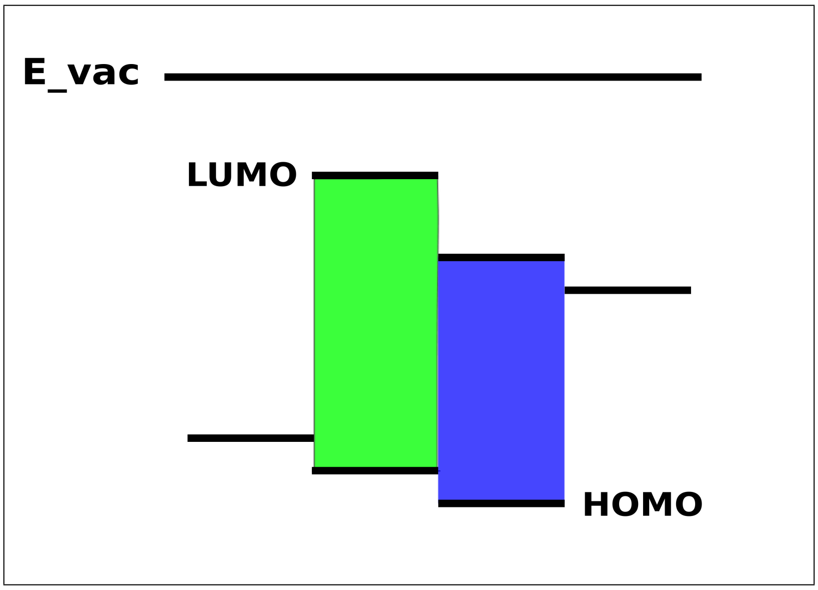

Figure 5.23: Schematic illustration of an energy level alignment representative for the device layouts simulated in this work. The vacuum energy level is included.

The region highlighted green represents the top semiconductor, the one coloured blue corresponds to the bottom semiconductor. The black bars on the upper and lower end of the coloured rectangles depict the respective HOMO and LUMO transport levels of the semiconductors. To the left and right of the coloured rectangles another two black lines can be found. They represent the workfunctions of the top contact (left) and the bottom contact (right). Additionally the vacuum energy level is drawn.

If the negative charges are situated at the upper side of the interface (left in the schematic drawings), the vacuum energy level is lowered by a defined amount in the device half below the interface, meaning in the second semiconductor (blue) and in the bottom contact. The HOMO and LUMO levels of the semiconductor (blue) are lowered by the same amount as the workfunction of the bottom contact material (black). A representative drawing of this situation can be found in Fig. 5.24.

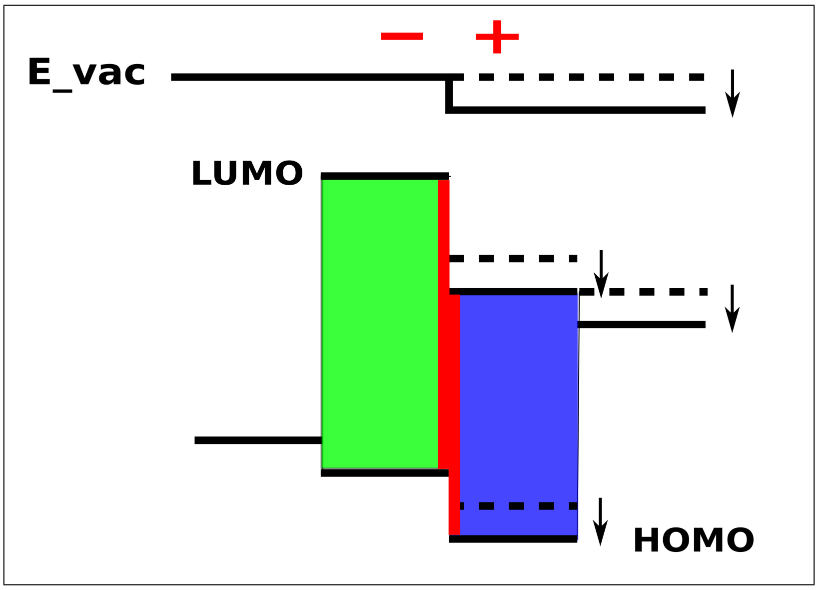

Figure 5.24: Shift in the vacuum energy level induced by a dipole layer situated at the planar heterojunction of the solar cell. The HOMO, LUMO levels of the bottom semiconductor (blue) as well as the workfunction of the bottom contact are shifted accordingly.

The charge density needed to induce a certain defined shift in the vacuum energy level can be estimated. For this purpose we regard the interface dipole layer as a parallel plate capacitor. From the known formula for the capacitance C of a parallel plate capacitor

$$C = \frac{\varepsilon_0 \varepsilon_r A}{d}$$

and the relation between the capacitance and the applied voltage U

$$Q = CU$$

the required charge carrier density at the interface ρ_{fix} per unit volume can be calculated. In the above formulas Q is the total charge that can be placed on a capacitor with capacitance C by applying a voltage U, ε_0 is the vacuum permeability and ε_r the relative permeabiltiy of the medium. The distance between the two parallel plates is named d. The surface area of each plate is denoted by A. As two materials with different permeabilties meet at the interface we use the mean value of both $\overline{\varepsilon_r} = \frac{\varepsilon_{r1}+\varepsilon_{r2}}{2}$. The total charge on the capacitor $Q = \rho_{fix} q \Delta y A$ is the product of the charge carrier density ρ_{fix} times the elementary charge q times the linespacing in y-direction Δy at the interface times the surface area A of the capacitor plates. The distance d between the plates is also described by the line spacing Δy at the interface. As a result we obtain for the fixed charge carrier density at the interface

$$\begin{aligned} \rho_{fix} q \Delta y A &= \pm \frac{\Delta E_{vac} \varepsilon_0 \overline{\varepsilon_r} A}{\Delta y} \\ \rho_{fix} &= \pm \frac{\Delta E_{vac} \varepsilon_0 \overline{\varepsilon_r}}{q (\Delta y)^2} \,, \end{aligned} \tag{5.1}$$

where $U = \Delta E_{vac}$ is the shift in the vacuum energy level to be reached.

If the orientation of the dipole layer is reversed, meaning the positive charges gather at the upper side of the interface the vacuum energy level of the top device half would be shifted downwards. As only the energy level alignment and not the absolute values play a role in the simulation, we are allowed to keep the energy levels of the top device half fixed and shift all energy levels of the bottom device half accordingly upwards. It is very important to make a connection between this Section and Section 5.7. In Section 5.7 two fundamentally different cases of energy level alignment have been introduced and discussed. As just mentioned here, an interface dipole layer changes the system by shifting the transport and contact levels with respect to each other. This means that the cases **1)** and **2)** of Section 5.7 can be established for a given system by introducing an appropriately oriented interface dipole layer with a defined dipole moment. This enables us to actively tune a given system's I-V characteristic to a dramatic extent.

To conclude these introductory remarks we show two simulations, both done with the model system parameters of Section 5.1. The first one was done with a fixed dipole layer at the interface hard written into the code. The negative charges were situated at the upper side of the interface, the positive charges at the lower side. To induce a shift of $\Delta E_{vac} = 0.2\,\mathrm{eV}$ both charge carrier densities were given the equal value of $n_{fix} = -p_{fix} = 1.0914 \cdot 10^{27}\mathrm{m}^{-3}$. The values for n_{fix} and p_{fix} were calculated from equation (5.1), using $\varepsilon_{r1} = \varepsilon_{r,PEN} = 3.5$ [39] and $\varepsilon_{r2} = \varepsilon_{r,C60} = 4.4$ [40] as material parameters. The simulation results are shown in Fig. 5.25.

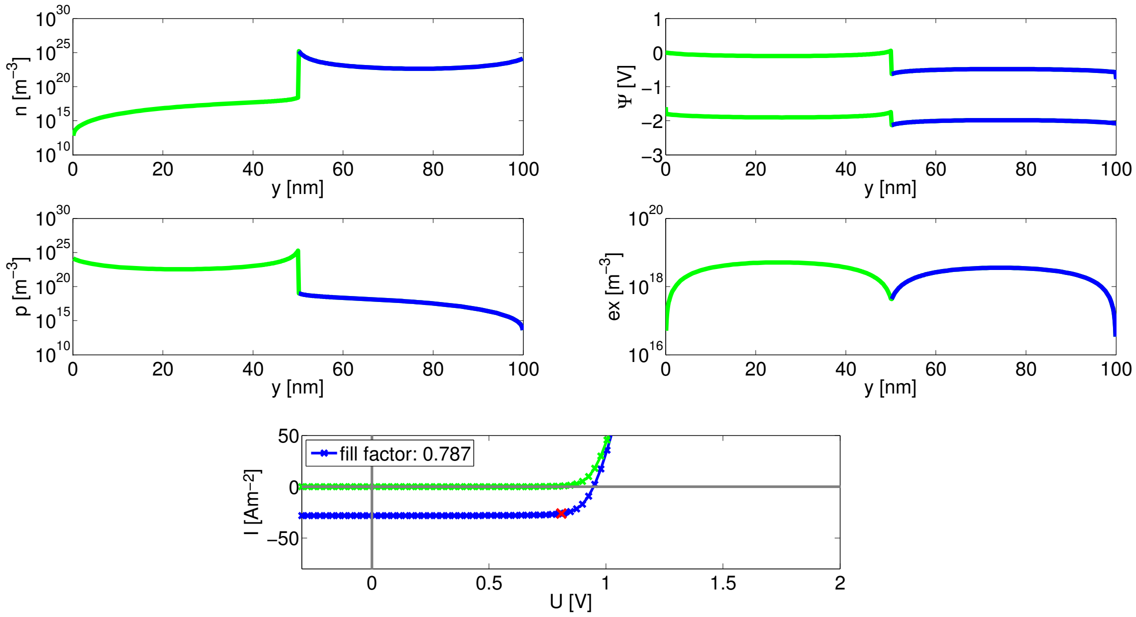

Figure 5.25: Simulation of the model system with no shift in the vacuum energy level, but with a fixed dipole layer at the organic-organic interface written into the code. The negative charges are situated at the upper side of the interface, the positive charges at the lower side. Both charge densities have the equal value of $n_{fix} = -p_{fix} = 1.0914 \cdot 10^{27}\mathrm{m}^{-2}$.

As discussed above, the presence of ρ_{fix} is equivalent to a shift in the vacuum energy level ΔE_{vac}. Thus, shifting the HOMO, the LUMO and the contact levels according to ΔE_{vac} should yield the same result as inserting a dipole layer. Consequently, the second simulation performed has no fixed charges at the interface, but all energy levels of the second half of the device were shifted by $\Delta E_{vac} = +0.2\,\mathrm{eV}$. The simulation results are shown in Fig. 5.26.

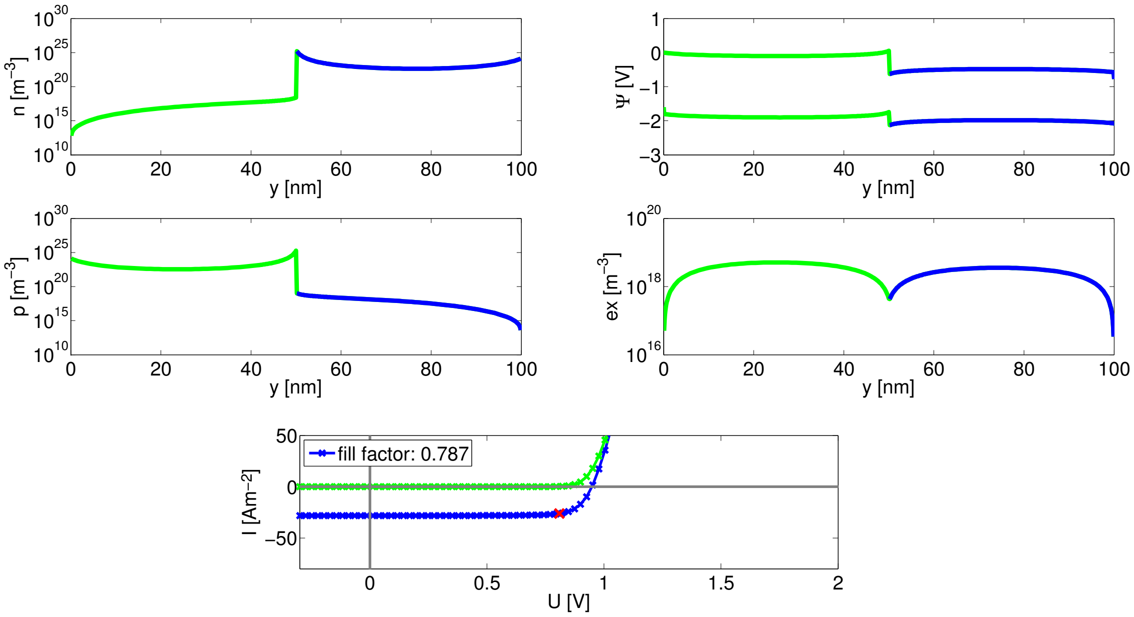

Figure 5.26: Simulation of the model system with a shift in the vacuum energy level of $\Delta E_{vac} = +0.2\,\text{eV}$. No additional dipole layer was inserted.

As we see, the simulation results of 5.25 and 5.26 are idential. The two described methods of simulation are equivalent. As the direct shift of the transport and contact energy levels can be realised and handled more easily in the program we employ this method in all further simulations. In the following calculations only the energy levels of the bottom device half are shifted, the ones of the top device half stay at their fixed values. The stated shifts ΔE_{vac} always describe the shift of the vacuum energy level of the bottom device half relative to its original position.

5.10 Impact of interface dipole layers on the model system

First we want to study the effects of an interface dipole layer on the model system described in Section 5.1. We again use Fig. 5.2 as the reference case. This reference simulation includes no shift in the energy levels.

For the first test case the vacuum energy level in the second half of the device was shifted by $\Delta E_{vac} = +0.2\,\text{V}$, i.e. the transport levels were adjusted in the blue marked region plus the bottom contact (see Fig. 5.24). Figure 5.27 shows the according simulation results.

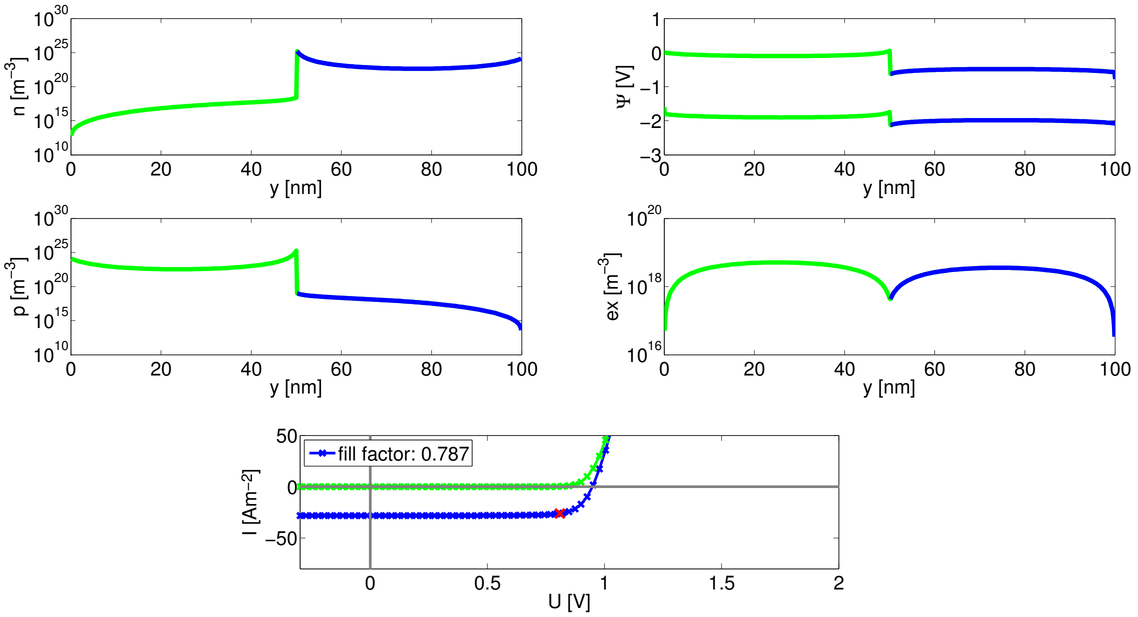

Figure 5.27: Simulation results for the model system described above with a shift in the vacuum energy level of $\Delta E_{vac} = +0.2\,\mathrm{V}$.

Looking at the top right graph, where the potential is plotted, it can be seen that the gap in the HOMO and LUMO levels ($\Delta\mathrm{HOMO}, \Delta\mathrm{LUMO}$) has increased and the minimal bandgap has decreased, as has the built-in voltage, because the workfunction of the bottom contact has been shifted as well.

Next we have a look at the electron and hole densities. In the maximum power point, which is used for both figures, the electron and hole densities reach much higher values in the case of $\Delta E_{vac} = +0.2\,\mathrm{V}$ than in the reference case. Additionally, the charge accumulation at the interface is much more distinct in the shifted case than in the reference case. This holds for the electron density as well as the hole density. The very prominent gathering of charges is a result of the large jumps in the HOMO and LUMO levels at the interface. As the external voltage is raised up to the maximum power point the transport levels reach the flat band condition or are even tilted a little bit upwards. This induces the electrons to travel towards the top contact and the holes towards the bottom contact. They are driven partially by drift and partially by diffusion. On their way to the opposite contact the charge carriers have to cross the organic-organic interface and the jump in potential situated there. This jump is increased by the shift of $\Delta E_{vac} = +0.2\,\mathrm{V}$ making it harder for the charge carriers to cross it. A smaller percentage of charge carriers crosses the interface at a given voltage.

The electrons are drawn towards the interface from the bottom side and the holes from the top side by the external voltage. But as they are stuck on their side more and more electrons/holes gather at the interface. This accumulation itself is a dipole layer at the interface, which creates an electric field. The field superimposes the strong local electric field already situated at the interface and weakens it. The charge carriers accumulate in such numbers that their own electric field lowers the potential barrier sufficiently for them to cross the interface.

The massively increased density at the interface of course also heightens the diffusion away from it, but as is clearly visible in Fig. 5.27 this effect does not level out the charge carrier density.

We now move on to the I-V characteristic of the solar cell. It has the expected shape, the rise of the light current accords with the rise in the dark current. The open circuit voltage is $V_{oc} \approx 0.955\,\mathrm{V}$, which is slightly increased compared to the reference case (Fig. 5.2).

The marginal rise in V_{oc} is contrary to what one would expect. The shift in the contact workfunction by $+0.2\,\mathrm{V}$ decreases the built-in voltage from $V_{bi} = 0.9\,\mathrm{V}$ to $V_{bi} = 0.7\,\mathrm{V}$. So one would expect the open circuit voltage to drop as well by about the same amount. This is obviously not the case. The first reason for the observed result could be the before mentioned rise in ΔHOMO, ΔLUMO. Charge carriers need a larger external voltage to cross the interface. However, the shift in V_{oc} is only small, because the already discussed charge accumulation around the flat band condition lowers ΔHOMO, ΔLUMO again. Therefore, an only slightly increased external voltage is needed to make charge carriers cross the barrier.

The short circuit current is not influenced by the shift in the vacuum energy level. This is the case, because the exciton dissociation rate in our program is not dependent on the electric field. This is not a physically correct assumption and should be tackled in a next step to improve the program. At this stage, however, it is not yet possible to look at the influence of an additional electric field, caused by an interface dipole layer, on the exciton dissociation and charge generation at the heterojunction. Consequently, the same short circuit current has to be expected in all following simulation studies of a shifted vacuum energy level.

The exciton distribution plotted in the bottom right corner is also not influenced as light absorption in the device is not affected by the dipole layer.

In the next simulation we shift the vacuum energy level by $\Delta E_{vac} = -0.1\,\mathrm{V}$. The results are shown in Fig. 5.28.

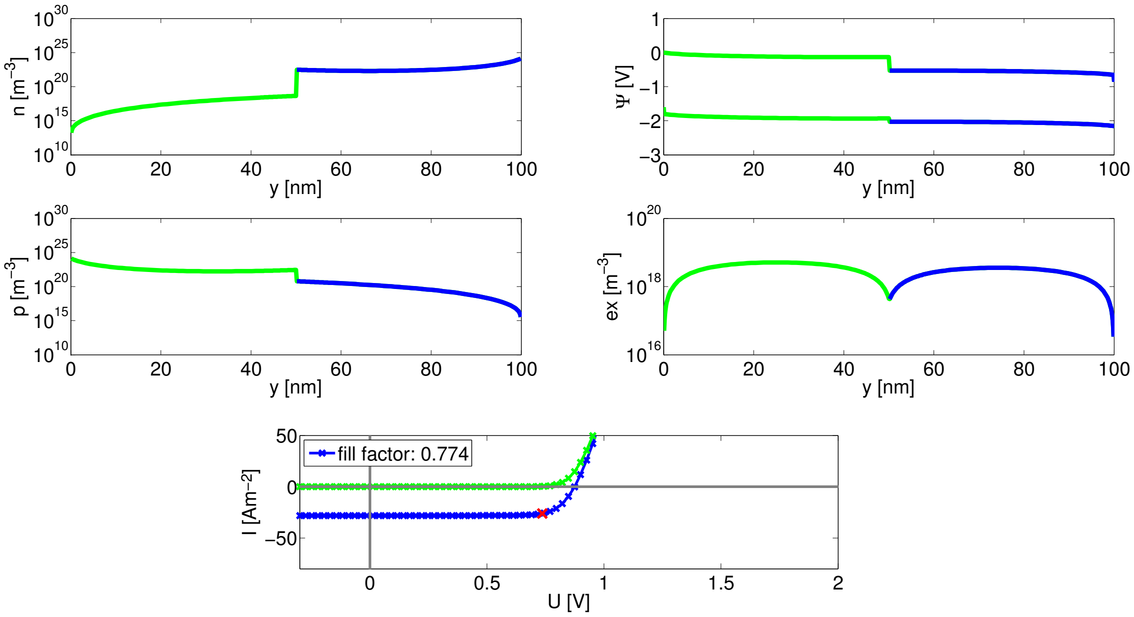

Figure 5.28: Simulation results for the model system described above with a shift in the vacuum energy level of $\Delta E_{vac} = -0.1\,\mathrm{V}$.

We expect the exact opposite tendencies as in the case $\Delta E_{vac} = +0.2\,\mathrm{V}$ (Fig. 5.27), only less prominent. Indeed we see a lowering of $\Delta\mathrm{HOMO}$, $\Delta\mathrm{LUMO}$ and there is an increase in the minimal bandgap and the built-in voltage. Actually the jump in the hole transport level is practically nonexistent. It is reduced to $\Delta\mathrm{HOMO} = 0.1\,\mathrm{V}$ and is still lowered a little bit further by the slight charge accumulation at the interface, which is noticeable in the electron and hole distributions.

In accordance with the afore mentioned explanation, the charge accumulation is much less pronounced than in both the other cases $\Delta E_{vac} = +0.2\,\mathrm{V}$ and $\Delta E_{vac} = 0.0\,\mathrm{V}$. The maximum charge carrier density at the heterojunction is orders of magnitude lower for $\Delta E_{vac} = -0.1\,\mathrm{V}$ than in the other two simulations. The charge carrier density at the contacts always stays practically at the same value. It is primarily determined by the contact modelling, which in all cases includes the more realistic contact simulation described in Section 5.2.

The drop in the hole density at the interface is much smaller than the drop in the electron density. This is caused by the smaller jump in the HOMO level than in the LUMO level at the interface: $\Delta\mathrm{HOMO} = 0.1\,\mathrm{V}$, $\Delta\mathrm{LUMO} = 0.4\,\mathrm{V}$. Holes can easily cross the interface in both directions.

We move on to inspecting the I-V characteristic. As already mentioned before, the short circuit current remains unchanged. The open circuit voltage drops by a small amount. This is the expected opposite tendency to the case $\Delta E_{vac} = +0.2\,\mathrm{V}$. The explanation is analogous. The fill factor is a little lower than for $\Delta E_{vac} = 0.0\,\mathrm{V}$.

As a last simulation for the model system we have a look at the exaggerated case of $\Delta E_{vac} = -0.3\,\mathrm{V}$. This relatively large shift in the vacuum energy level exceeds the original jump in the HOMO level at the interface, which is $\Delta\mathrm{HOMO} = +0.2\,\mathrm{V}$

and reduces it to $\Delta\text{HOMO} = -0.1\,\text{V}$. The holes now encounter a potential barrier on their way to the hole collecting top contact. The potential jump for electrons is not reversed, it is just diminished from $\Delta\text{LUMO} = 0.5\,\text{V}$ to $\Delta\text{LUMO} = 0.2\,\text{V}$. Electrons can still travel to their contact without hindrance. The simulation results are shown in Fig. 5.29.

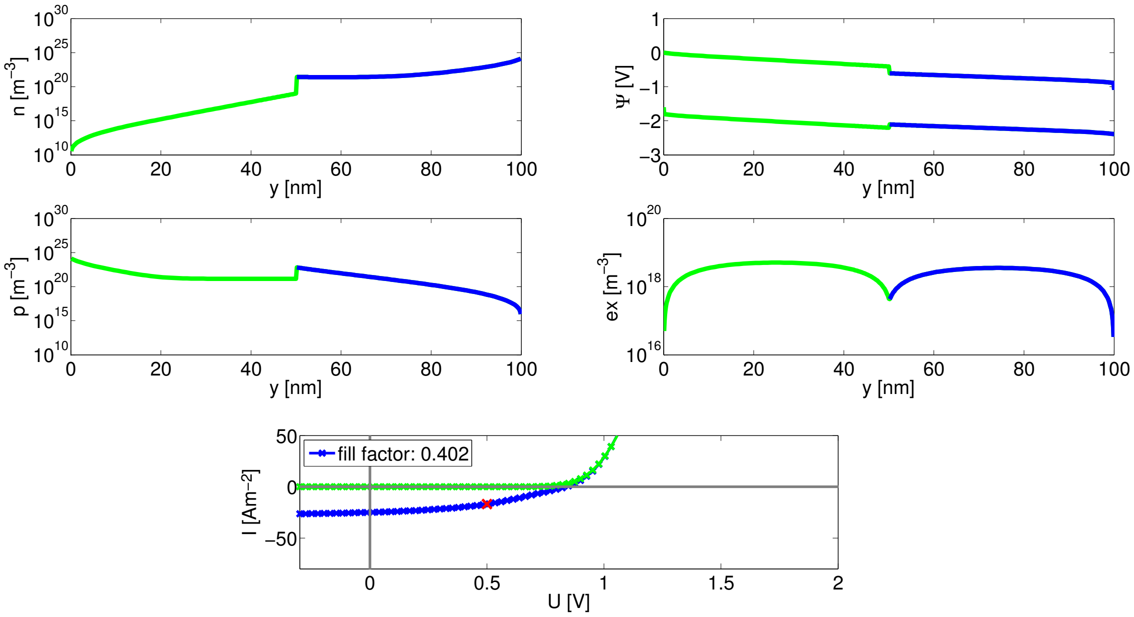

Figure 5.29: Simulation results for the model system described above with a shift in the vacuum energy level of $\Delta E_{vac} = -0.3\,\text{V}$.

One can see the reversed potential jump in the hole transport level in the top right graph. The barrier is only small, nevertheless it has a dramatic effect on the I-V curve.

We also see the influence on the hole concentration. At the contacts it reaches the same value as in the simulation $\Delta E_{vac} = 0.0\,\text{V}$. The density decreases from the top contact to the interface, where it abruptly rises. It stays at a higher level in the electron conductor (blue) than in the hole conductor (green).

Holes are generated next to the interface and need to cross it to reach the top contact. They can not easily overcome the potential barrier. Hence, they accumulate at the lower side of the interface.

We now come back to the I-V curves. The dark curve looks normal enough, leaving aside the quite flat slope at V_{oc}. The light current on the other hand looks very poor. The fill factor of $FF = 0.40$ is exceptionally low. The current starts to rise even at the low value of $V_{ext} \approx 0.2\,\text{V}$ and grows steadily until it reaches zero and positive values. The reason for this behaviour is the potential barrier for holes traveling from the bottom to the top contact, whereas there is no barrier for holes moving in the opposite direction.

5.11 Impact of interface dipole layers on the system ITO/PEN/C60/Al

We will now study the impact of a shift in the vacuum energy level on the behaviour of the system ITO/PEN/C60/Al. The reference simulation for this system is shown in Fig. 5.19 of Section 5.7. In this reference case no shift in the vacuum energy level is included.

The first test simulation was done with a shift in the vacuum energy level of $\Delta E_{vac} = +0.5\,\mathrm{V}$. The according results are depicted in Fig. 5.30.

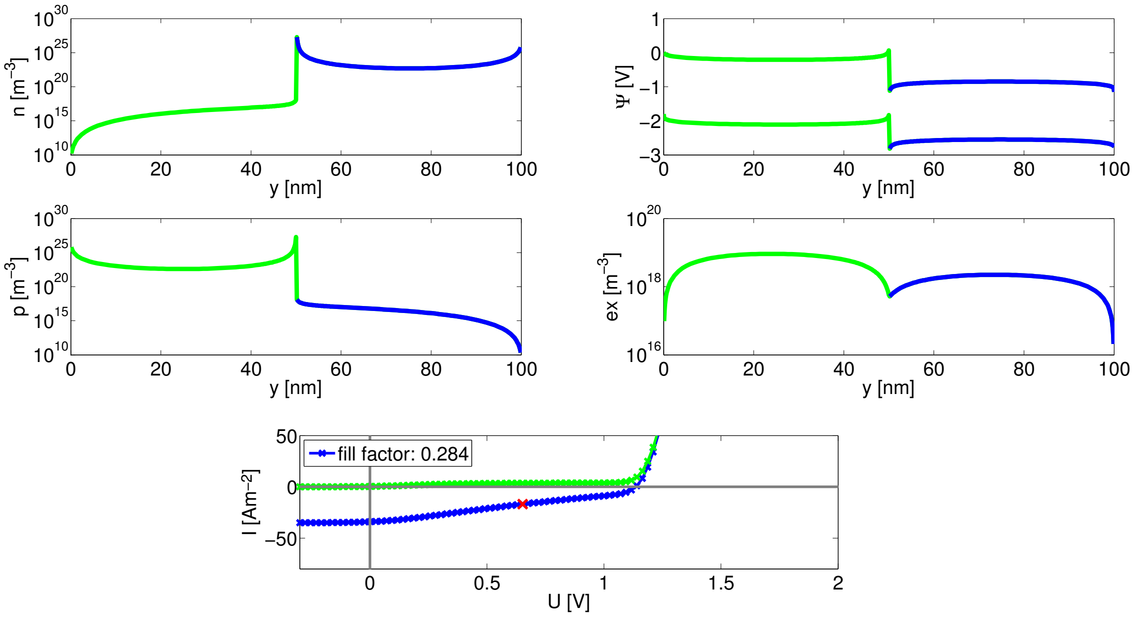

Figure 5.30: Simulation results for the system ITO/PEN/C60/Al with a shift in the vacuum energy level of $\Delta E_{vac} = +0.5\,\mathrm{V}$.

At first sight the features of this simulation are merely more pronounced than those of the reference simulation, Fig. 5.19. The potential distribution as well as the electron and hole densities show a larger drop at the interface at the maximum power point, which is plotted.

The I-V characteristic also looks similar in both cases. Yet here, the slope changes earlier, even as soon as $V_{ext} \approx 0.15\,\mathrm{V}$, which is roughly the built-in voltage in the shifted case $V_{bi} = 0.1\,\mathrm{V}$.

The open circuit voltage has not shifted noticeably, but the current around V_{oc} is much weaker in this case than in the reference case. The dark current again behaves according to the light current and also rises slightly at $V_{ext} \approx 0.15\,\mathrm{V}$.

Summing up we find that the built-in voltage has decreased by 0.5 V and the gaps in the HOMO and LUMO levels have increased by the same amount, the potential at the interface has also changed accordingly in the maximum power point.

Charge carriers accumulate at the interface until their electric field has lowered the potential barrier sufficiently for them to cross it. The critical height of the barrier, at which charge carriers can overcome it is determined by the externally applied electric field, giving the charge carriers a certain starting potential energy and the ambient temperature responsible for the thermal energy. The barrier must not be higher than the sum of both these energies.

The parameter most affected by the slope of the current voltage characteristic is the fill factor. It is reduced to the meagre level of $FF = 0.28$.

The next case study was done with an energy shift of the same amount but in the opposite direction. The vacuum energy level was shifted by $\Delta E_{vac} = -0.5\,\mathrm{V}$. In Fig. 5.31 the simulation results are shown.

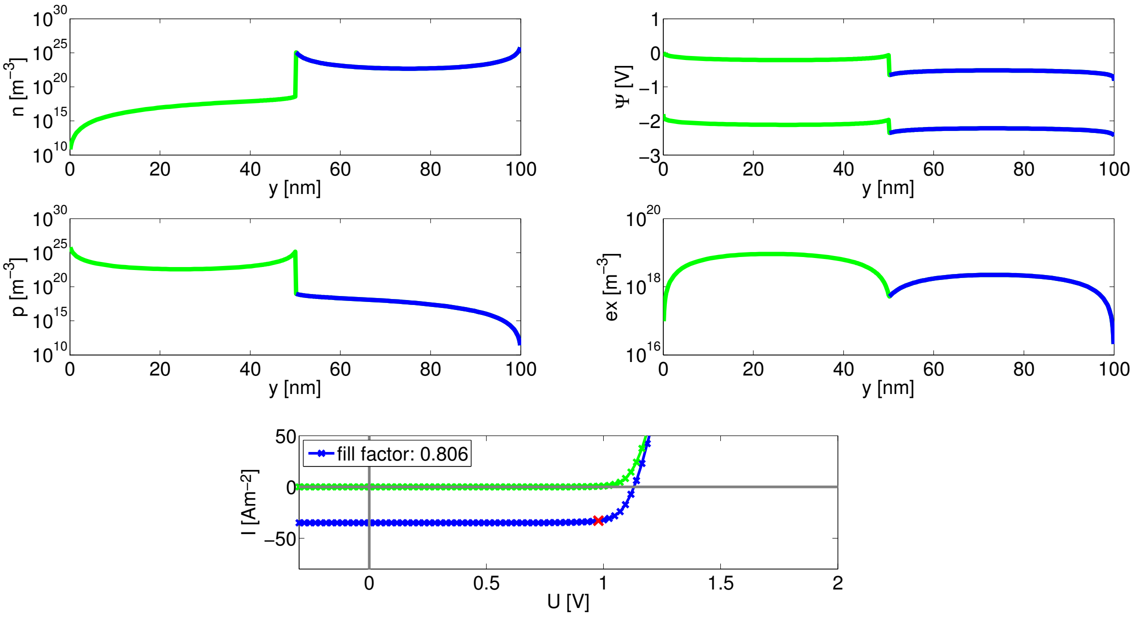

Figure 5.31: Simulation results for the system ITO/PEN/C60/Al with a shift in the vacuum energy level of $\Delta E_{vac} = -0.5\,\mathrm{V}$.

We immediately notice the different shape of the I-V curve. No kink whatsoever can be detected. The current stays at the same value until it rises near the open circuit voltage. This is the typical shape of an I-V curve, which we know from the model system simulation.

Looking at the shifted energy levels and their alignment

- ITO: $\Phi = 4.8\,\mathrm{eV}$,
- PEN: $\mathrm{HOMO} = 4.9\,\mathrm{eV}, \mathrm{LUMO} = 3.0\,\mathrm{eV}$,
- C60: $\mathrm{HOMO} = 5.3\,\mathrm{eV}, \mathrm{LUMO} = 3.6\,\mathrm{eV}$,
- Al: $\Phi = 3.7\,\mathrm{eV}$,

we see that we indeed simulated a similar layout. Because of the energy shift, the condition $V_{bi} > \min\{|\Delta\text{HOMO}|, |\Delta\text{LUMO}|\}$ of Section 5.7 is fulfilled. As already stated in that section no kinks appear in the I-V curve under these circumstances.

By increasing the external voltage we compensate the jump in the HOMO/LUMO levels before we even reach V_{bi}. Therefore, the charge carriers have no chance of crossing the interface long before V_{oc}. In Fig. 5.31 we clearly see that they only can overcome the barrier when the external voltage equals or is bigger than the built-in voltage, $V_{ext} \geqslant V_{bi} = 1.1\,\text{V}$. This corresponds well with the behaviour of the dark current.

We now have a look at the electron and hole densities. They are less increased at the heterojunction. This is a very reasonable tendency. The jumps in the potential are already reduced by 0.5 V, so less charge carriers need to gather to further reduce them to manageable levels.

The last simulation was done with a shift in the vacuum energy level of $\Delta E_{vac} = -1.0\,\text{V}$. The simulation results are shown in Fig. 5.32.

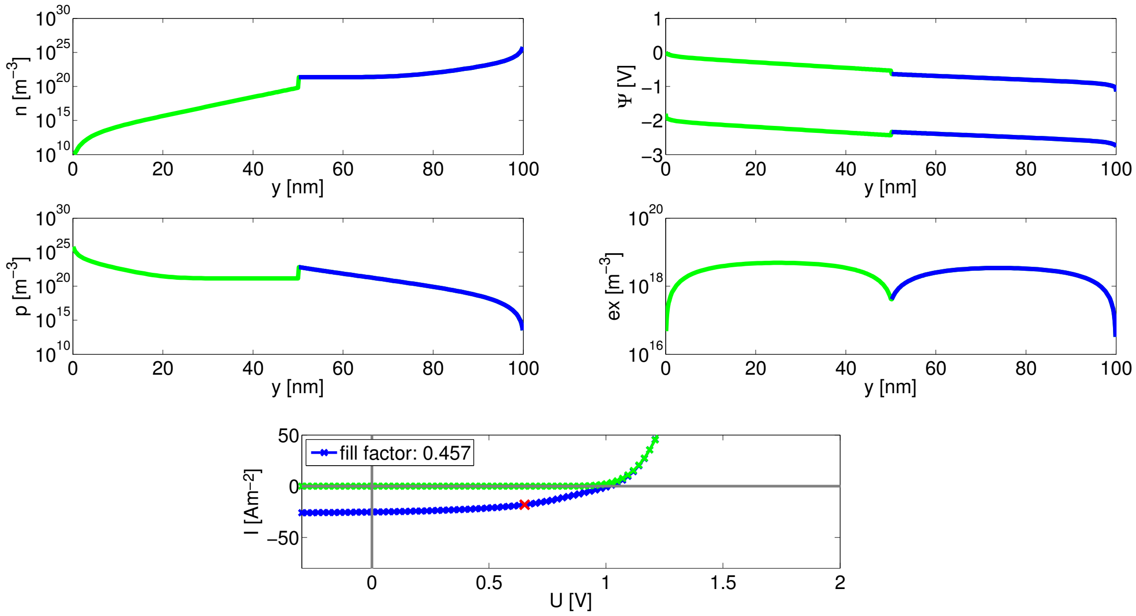

Figure 5.32: Simulation results for the system ITO/PEN/C60/Al with a shift in the vacuum energy level of $\Delta E_{vac} = -1.0\,\text{V}$.

The shift in E_{vac} is chosen so that it overcompensates the jump in the HOMO level, which changes from $\Delta\text{HOMO} = 0.9\,\text{eV}$ to $\Delta\text{HOMO} = -0.1\,\text{eV}$. The gap between the LUMO levels is just reduced from $\Delta\text{LUMO} = 1.1\,\text{eV}$ to $\Delta\text{LUMO} = 0.1\,\text{eV}$, it does not change sign.

The built-in voltage is increased from $V_{bi} = 0.6\,\text{V}$ to $V_{bi} = 1.6\,\text{V}$, yet the open circuit voltage lies far beneath that value, as can be seen clearly in Fig. 5.32. The fill factor is not very high.

The open circuit voltage reaches a value of $V_{oc} \approx 1.0\,\text{V}$, which stands in stark contrast to the built-in voltage of $V_{bi} = 1.6\,\mathrm{V}$. The explanation for this behaviour is the same as for the analog simulation of the model system, see Fig. 5.29.

The holes encounter an energy barrier on their way from the semiconductor interface to the top contact, but not on the way to the bottom contact, which is intended as the electron collecting contact. Thus, a larger number of holes travels in the wrong direction, decreasing the current in the wanted direction. Furthermore, on their way to the bottom contact holes have more possibilities to recombine with electrons than in the top half of the device. Through such recombination events the wanted current is weakened even further, because less electrons reach the aluminum contact.

These speculations can be verified by looking at the charge carrier densities. The hole density in the second half (blue) is much too high. It even exceeds the concentration in the first half (green), except at the contacts, where it is predetermined by the contact modelling. The electron density in the bottom half (blue) on the other hand is much too low. It is the consequence of the increased recombination in this device region.

6 Conclusion

The aim of this thesis is the simulation of the behaviour of organic solar cells with an interface dipole layer. We specifically study planar heterojunction solar cells consisting of two different organic semiconductors. For this purpose we perform two-dimensional drift-diffusion simulations based on the self-consistent solution of the drift-diffusion-current and the continuity equations for electrons, holes and excitons in combination with the Poisson equation. They are solved on a two-dimensional mesh with variable grid spacing. The input parameters include the HOMO and LUMO levels of the semiconductors, the workfunctions of the contacts as well as the charge carrier mobilities for both active layers. The AM 1.5 solar spectrum is used for the incoming light intensity. The exciton generation follows Lambert Beer's law of absorption. Exciton dissociation is assumed to be independent of the acting electric field. The charge carrier recombination is assumed to be of Langevin type. The contact modelling includes thermionic emission and tunnelling from the contact into the semiconductor. This way a number of scenarios were simulated for a model case with small band offsets and for the realistic system ITO/PEN/C60/Al. The influence of a fixed dipole layer situated at the planar heterojunction on the current-voltage characteristics is studied. Various combinations of level alignments and dipole moments are tested. The non-ohmic contact modelling leads to more realistic open circuit voltages than ohmic contact modelling. Furthermore the reflective back contact increases the short circuit current by a significant amount and thus has to be taken into account. The main new insight of this thesis was that interface dipole layers greatly influence the current-voltage characteristic. Firstly they shift the transport levels and thus change their relative alignment. This can lead to a strong charge carrier accumulation at the interface, which in turn greatly enhances the diffusion of electrons and holes. Secondly we found s-shaped current-voltage characteristics if the built-in voltage is lower than the minimum of the HOMO/LUMO level offsets. This condition can be regulated by introducing an appropriately strong interface dipole layer. Thereby the HOMO, LUMO and contact levels can be shifted until the built-in voltage is larger than the HOMO/LUMO level offsets, which has been found to yield I-V characteristics without s-shapes and therefore good fill factors.

7 Acknowledgements

I would like to thank my supervisors Ao.Univ.-Prof. Dr.techn. Ferdinand Schürrer and Dipl.-Phys. Dr.rer.nat. Karin Zojer sincerely for their support, advice and encouragement throughout this thesis. I am especially grateful for their patience in answering my endless questions. This work has been done in cooperation with the "Christian Doppler Labor für Nanokomposit Solarzellen" at the Technical University of Graz who also gave financial support. For their help I want to thank the whole group and especially their head Dipl.-Ing. Dr. Univ.Doz. Gregor Trimmel. I also would like to thank Manfred Gruber very much for helping me whenever I got stuck writing new code and for the friendly atmosphere in our office. Without his aid this thesis would have taken far longer to complete. At this place I want to thank my family for their constant support and encouragement. Lastly I would like to thank all my colleagues and friends, who accompanied me during my studies and helped me so often.

Bibliography

[1] pn-junction in solar cell. Internet: http://mrsec.wisc.edu/Edetc/SlideShow/images/pn_junction/pn_junction_solar.jpg (accessed 1 June **2009**)

[2] Principles of an organic solar cell. Internet:
http://www.worldcommunitygrid.org/
images/cep1/faq_1.jpg (accessed 1 June **2009**)

[3] B. A. Gregg and M. C. Hanna: J. of Appl. Phys., Vol. 93, No. 6, **2003**

[4] Reference Solar Spectral Irradiance. Internet:
http://rredc.nrel.gov/solar/spectra/am1.5/ (accessed 1 June **2009**)

[5] Sonnstrahlung. Internet: http://de.wikipedia.org/wiki/Sonnenstrahlung (accessed 1 June **2009**)

[6] L. Kulikovsky: Experimentelle Untersuchung der Ladungträgerdynamik in photoreaktiven Polymeren, PhD thesis, Univ. Potsdam, **2003**

[7] E. A. Schiff: J. of Non-Cryst. Sol., 190, 1−8, **1995**

[8] A. Mozunder: J. Chem. Phys., 60, 4305−4310, **1974**

[9] C. Im: Optoelektronische Eigenschaften von π-konjugierten Polymeren. PhD thesis, Univ. Marburg / Lahn **2002**

[10] C. M. Swoden: Introduction to Semiconductor Device Modelling, World Scientific Publishing, Singapore **1986**

[11] G. A. Buxton, N. Clarke.: Mod. Sim. Mater. Sci., Eng., 13−26 **2007**

[12] J. Frenkel: Phys. Rev. 54, 647−648, **1938**

[13] J. E. Sutherlan: IEEE Trans. Elect. Dev, Vol. Ed. 24, No. 4, April **1977**

[14] M. Glatthaar *et al.*: Sol. Ener. Mater. and Sol. C., Vol. 91, 390−393, **2007**

[15] A. Iserles: A First Course in the Numerical Analysis of differential equations. Cambridge University Press, **1996**

[16] S.M. Sze: Semiconductor devices, physics and technology. Wiley & Sons, 2nd Ed., **2001**

[17] P.A. Markowich, C.A. Ringhofer and C. Schmeiser: Semiconductor Equations. Springer-Verlag, Wien **1990**

[18] M. Lundstrom: Fundamentals of Carrier Transport, 2nd Edition. Cambridge University Press, **2000**

[19] C. Cercignani: The Boltzmann Equation and Its Applications (Applied Mathematical Sciences, Vol. 67). Springer-Verlag, Berlin **1988**

[20] F. Poupaud: Etude Mathematique et Simulations Numeriques de Quelques Equations de Boltzmann. Thesis, Univ. Paris 6 **1988**

[21] S. Selberherr: Analysis and Simulation of Semiconductor Devices. Springer-Verlag, Wien-New York **1984**

[22] S.M. Sze: Physics of Semiconductor Devices. J. Wiley & Sons, New York **1981**

[23] C.Y. Chang and S.M. Sze: Solid-State Electronics, 13, 727 **1970**

[24] J.M. Shannon: Solid-State Electronics, 19, 537 **1976**

[25] P.S. Davids, I.H. Campell and D.L. Smith: J. Appl. Phys., 82, 6319 **1997**

[26] V.I. Arkhipov, U. Wolf and H. Bässler: Phys. Rev. B., 59, 7514 **1999**

[27] M. Gruber, F. Schürrer and K. Zojer: Org. Electron., 13, 1887 **2012**

[28] J. Huang, J. Yu, Z. Guan and Y. Jiang: Appl. Phys. Lett., 97, 143301 **2010**

[29] M. Gruber, B.A. Stickler, G. Trimmel, F. Schürrer, K. Zojer: Org. Electron., 11, 1999 **2010**

[30] T. Rath *et al.*: Adv. Energy. Mat., 1, 1046 **2011**

[31] M. Gruber: Investigation of morphology effects on the performance of organic solar cells and hybrid cells by two-dimensional drift-diffusion simulations. Diplomarbeit, TU Graz **2009**

[32] S. Yoo, B. Domercq and B. Kippelen: Appl. Phys. Lett., 85, 5427 **2004**

[33] A. Tada, Y. Geng, Q. Wei, K. Hashimoto and K. Tajima: Nature Mater., 10, 450 **2011**

[34] A. Kumar, S. Sista and Y. Yang: J. Appl. Phys., 105, 094512 **2009**

[35] G. Heimel, I. Salzmann, S. Duhm, J.P. Rabe and N. Koch: Adv. Funct. Mater., 19, 3874 **2009**

[36] S. Braun, W.R. Salaneck and M. Fahlman: Adv. Mater., 21, 1450 **2009**

[37] W. Osikowicz, M.P. de Jong and W.R. Salaneck: Adv. Mater., 19, 4213 **2007**

[38] R.R. Lunt, N.C. Giebink, A.A. Belak, J.B. Benzinger and S.R. Forrest: J. Appl. Phys., 105, 053711 **2009**

[39] C.H. Kim *et al.*: J. Appl. Phys., 109, 083710 **2011**

[40] H. Kataura, Y. Endo, Y. Achiba, K. Kikuchi, T. Hanyu and S. Yamaguchi: J. Phys. Chem. Solids, 58, 1913 **1997**

[41] B.A. Stickler, M. Gruber, G. Trimmel, F. Schürrer and K. Zojer: Org. Electron., 12, 1434 **2011**

[42] J. Meiss *et al.*: Phys. Rev. B., 83, 165305 **2011**

[43] G.A. Buxton and N. Clarke: Modelling Simul. Mater. Sci, Eng., 15, 13 **2007**

[44] W. Tress, A. Petrich, M. Hummert, M. Hein, K. Leo and M. Riede: Appl. Phys. Lett., 98, 063301 **2011**

[45] C. Uhrich *et al.*: J. Appl. Phys., 104, 043107 **2008**

[46] B.R. Saunders and M.L. Turner: Adv. Coll. Interf. Sci., 138, 1 **2008**

[47] W. Demtröder: Experimentalphysik 2. Springer-Verlag, Berlin-Heidelberg **2009**